Open-Access Microcavity - a New Platform for the Study of Interacting Exciton-Polaritons

Laurynas Giriunas

Department of Physics

University of Sheffield

A thesis submitted for the degree of

Doctor of Philosophy

2017 September

Acknowledgements

First and foremost, I would like to give my appreciations to my supervisor Dr. Dimitrii Krizhanovskii, who has never doubted my capabilities and who provided me with encouragement and patient guidance throughout the dissertation process, and Prof. Feng Li, who helped me a lot during his post-doc at the University of Sheffield. Also, I owe my gratitude to the other Low DImensional Devices and Structures (LDSD) group research students for their time, sincere help and enthusiasm. Without their input, the dissertation would not have been possible. I would also like to thank my dear girlfriend Monika. It was her optimism and companionship that supported me during the difficult moments and made me smile even in stressful situations. Finally, my deepest gratitude belongs to my family and especially my parents, who are always there for me. It is your support that made me who I am today and helped me to pursue my dreams. Thank you!

Publication List

Pending Publications

L. Giriunas, F. Li, D. Solnyshkov, G. Malpuech, M.S. Skolnick, and D. N. Krizhanovskii. "Condensation of free exciton-polaritons with tunable light-matter coupling strength". Aimed at *Appl. Phys. Lett.*

L. Giriunas, F. Li, M. Sich, M. S. Skolnick, and D. N. Krizhanovskii. "Polariton condensation and parametric scattering with a cold exciton reservoir in a tunable open microcavity". Aimed at *Appl. Phys. Lett.*

Journal Publications

S. Dufferwiel, Feng Li, A. A. P. Trichet, **L. Giriunas**, P. M. Walker, I. Farrer, D. A. Ritchie, J. M. Smith, M. S. Skolnick, and D. N. Krizhanovskii. "Tunable polaritonic molecules in an open microcavity system". *Appl. Phys. Lett.* 107, 201106 (2015).

S. Dufferwiel, Feng Li, E. Cancellieri, **L. Giriunas**, A.A.P. Trichet, D.M. Whittaker, P.M. Walker, F. Fras, E. Clarke, J.M. Smith, M.S. Skolnick, and D.N. Krizhanovskii. "Spin Textures of Exciton-Polaritons in a Tunable Microcavity with Large TE-TM Splitting". *Phys. Rev. Lett.* 115, 246401(2015).

S. Dufferwiel, F. Fras, A. Trichet, P. M. Walker, F. Li, **L. Giriunas**, M. N. Makhonin, L. R. Wilson, J. M. Smith, E. Clarke, M. S. Skolnick, and D. N. Krizhanovskii. "Strong exciton-photon coupling in open semiconductor microcavities". *Appl. Phys. Lett.* 104, 192107 (2014).

Conference Poster Presentations

L. Giriunas, F. Li, S. Dufferwiel, E. Cancellieri, A. Trichet, P. M. Walker, D. M. Whittaker, J. M. Smith, E. Clarke, I. Farrer, D.A. Ritchie, M. S. Skolnick, and D. N. Krizhanovskii. "Tunable Open Cavities: A Powerful and Versatile Tool for Exploring Light-Matter Interactions". Nanotech Dubai 2016, Dubai, UAE, December (2016).

L. Giriunas, S. Dufferwiel, F. Li, E. Cancellieri, A. Trichet, D. M. Whittaker, P. M. Walker, E. Clarke, I. Farrer, D. A. Ritchie, J. M. Smith, M. S. Skolnick, D. N. Krizhanovskii. "Manipulating Spin Textures of Polariton Condensates in a Tunable Hemispherical Microcavity". EP2DS-21/MSS-17, Sendai, Japan, July (2015).

Abstract

There are couple types of semiconductor microcavities. The most general structure type is fabricated using two distributed Bragg reflector (DBR) mirrors attached by a layer of semiconductor, whereas in open microcavity it is separated by a gap of air or vacum. In this device periodically repeating pairs of low and high refractive index semiconductor layes allows to reflect light very efficiently. Lately, interest increased in the use of open microcavities as they allow to investigate light and matter interactions in an alternative and more freely tunnable way. This system allows creating and studying of polaritons (which are quasi-particles created, when photons and excitons couple strongly) in case QWs (quantum wells) are introduced into the microcavity or even making a single photon source, in case a SAW (sound acoustic wave) device will be manufactured on the bottom mirror, which has QWs, successfully. Single photon source is very important in order to develop secure communication and quantum computers. A very welcoming use case of the open cavities is allowing to very effectively investigate vey small amounts of fluids in absorption spectroscopy, as well as development of ultralow-threshold lasers (low threshold appears, because photons spend more time in the cavity, which depends on Q-factor), because of recirculation in small volume mode, interaction for the same incident power increases as $I = P_{in}\frac{\lambda}{2\pi n}\frac{Q}{V}$, enhanced emitters, tunable microfilters and etc. ([1], [2], [3]). Polaritons also have long propagation distances, which allows to consider using them for optical circuits ([4]).

The project aim is to use this optical semiconductor microcavity system, which allows easy cavity tuning into resonance, to investigate

various effects in coupled mirrors, achieve polariton blockade and etc. Samples were made by University of Cambridge, University of Oxford and III-IV semiconductor center in Sheffield. In Chapter 2 experiments using planar DBR mirrors inside open cavity are present. For example, Rabi dependence on cavity length and optimum threshold dependence on detuning. Chapter 3 has data collected using top sample containing top concave mirror. Effective mass and coupled concave mirror coupling strength dependence on cavity length are good examples. Chapter 4 contains introduction of new setup design, which works in transmission and not reflectivity mode, and experiments carried on using it, like achievement of a very efficient polariton transfer from LG01 to LG00 mode. Chapter 5 will introduce to experiments which will be carried out in the future. This includes use of Surface Acoustic Waves (SAW), organic materials and etc.

Contents

Chapter 1

Background

1.1 III-V Semiconductors. Quantum Wells and Quantum Dots

A semiconductor is a material that has a higher conduction than insulators, but lower than conductors. $InGaAs/AlGaAs$ will be the most relevant materials throughout this thesis. Electric current conduction in a semiconductor depends on its temperature (with increasing temperature, conduction increases, the opposite of metals) and doping level (introduction of impurities to alter material properties). This is explained by its unique band structure, the energy gap between the conduction band (the lowest energy of empty orbitals, which are available for electrons) and the so-called valence band (it corresponds to the highest energy of electrons at a temperature of 0K). It defines the range in which electron states cannot occur Fig. 1.1.

If an electron has enough energy, usually after absorbing a photon with an energy higher than the band gap, it can jump from valence band to conduction band and - because of neutral semiconductor charge - valence band is left with a positively charged hole. Then the electron and the hole can attract one another, because of the Coulomb force, and form a system comparable to a hydrogen atom, called an exciton. An exciton has a binding energy of $E_b^n = \frac{R_E}{n^2}$, where R_E is Rydberg energy $R_E = \frac{\mu e^4}{2\hbar^2(4\pi\epsilon_0\epsilon)^2}$, with μ being the reduced mass, and

n - the principal quantum number. Binding energy is the measure of exciton stability. Excitons dissociate into free electrons and holes if the binding energy is smaller than the thermal energy. For example, the thermal energy at room temperature is around 25meV, and the exciton binding energy in GaAs is 5meV [5] and 60meV in ZnO [6], leading into unstable GaAs and stable ZnO excitons at room temperature.

ZnO binding energy has led to a good deal of research, as it promises polaritons at room temperature. Polaritons are quasi-particles appearing because of the strong coupling between excitons formed in quantum wells and confined photons in microcavities. ZnO excitons' stability at room temperature does not require a cooling down of the material and makes their use in technology easier, whereas GaAs has to be cooled to below liquid Nitrogen temperatures and use of liquid Hydrogen generally makes the technology too expensive and cumbersome.

Depending on a semiconductor's dielectric constant, excitons can be grouped into two types. The first type is Frenkel excitons, which have a small dielectric constant and strong interaction between particles. The second type is Wannier-Mott excitons, which have a large dielectric constant, but a smaller interaction between particles and a radius greater than the lattice spacing. Another important parameter is the exciton's Bohr Radius $a_B = \frac{\hbar}{\sqrt{2\mu R}}$, which allows the determination of the exciton density at which excitons ionise and stop existing, resulting in electron-hole plasma. This density, at which transition occurs, is called the Mott density. It describes the situation when the distance between excitons becomes very similar to the Bohr radius, and the interaction among excitons and holes starts being screened by other charged particles. Before the Mott density is reached, excitons and holes behave as gas of excitons and at even higher densities it becomes an electron-hole plasma. The larger the Mott density, the more particles can be injected into materials while still having polaritons. These quasi-particles, excitons, can be trapped in one dimension by placing higher-band gap materials around a thin layer of low-band gap material. This structure is called a Quantum Well (QW) (Fig. 1.2). Because of the confinement, it requires a greater force to separate the hole and the electron; thus, the binding

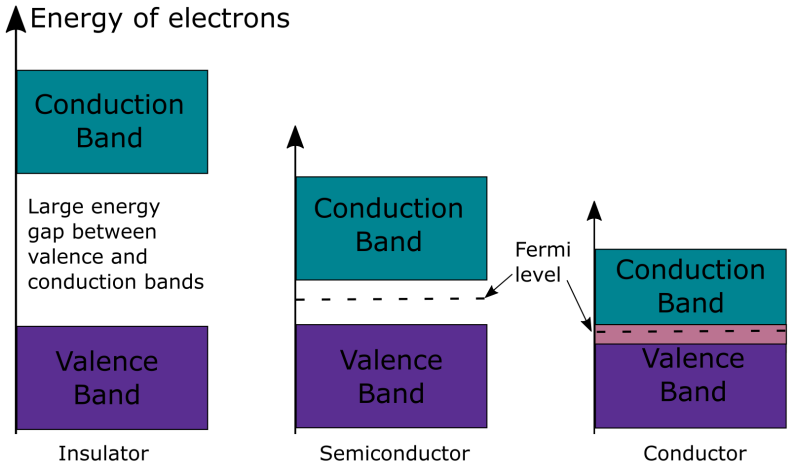

Figure 1.1: Insulator, semiconductor and conductor band structure. The valence band corresponds to the highest energy of electrons at 0K, and the conduction band is the lowest energy of empty orbitals available for electrons. Decreasing the band gap size increases the material's electron conduction.

energy becomes larger.

1.2 Microcavities

Since 1946, when Purcell suggested that spontaneous emission of the emitter could change depending on its environment, light and matter interaction has interested many scientists [7]. This idea was proven by [8] and [9]. Generally light and matter interact very weakly. In order to increase this interaction, therefore, the emitter was placed in the microcavity, to increase the number of times a photon passes through the emitter. In the usual materials, an exciton emitted photon escapes before being reabsorbed again.

Microcavities were developed to confine light inside of the material. Semiconductor microcavities are fabricated from two distributed Bragg reflector (DBR) mirrors, which are separated by a samiconductor layer representing a cavity layer. DBR mirrors are made by repeating two different semiconductor layers with different refractive indexes. Their thickness is $\lambda_{ab}/4n$ (λ_{ab}-wavelength of reflected light); such thickness is used because the appearance of 2π phase difference be-

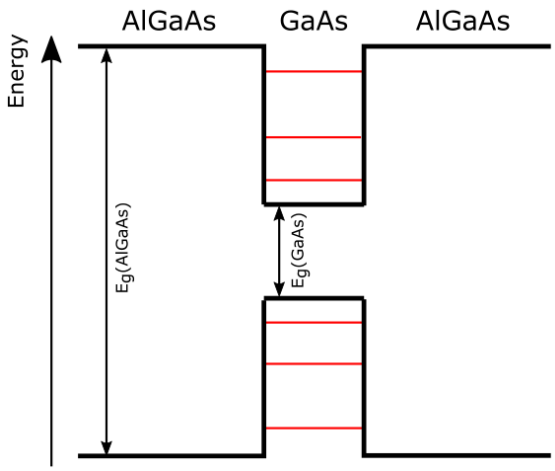

Figure 1.2: GaAs Quantum Well (QW) structure shown as band gap energy versus used material arrangement. A 20nm GaAs layer is surrounded by AlGaAs material with higher band gap. Particles are trapped inside QW as it requires higher energy for them to overcome the energy barrier and move to the AlGaAs conduction layer. Because of the confinement, GaAs energy structure changes as well and starts to have distinct energy levels as only certain wavelengths can be tapped inside QW.

tween DBR layers creates constructive interference. The wavelength of the wave that should be reflected inside of the microcavity and material's refractive index determines the thickness of layers. A partial relection of optical waves is caused by each layer boundary, and because of the generally large number of layers, DBR mirrors become very effective. They can reflect at least 99.99% of incoming light and even higher reflectivity is possible (metallic mirrors reflect up to 99%, because of their high absorption, and to achieve better 99.999% reflectivity, dielectric mirrors are used [5]). There are no perfect mirrors, and some photons always escape or are absorbed by the material. Increasing number of DBR layers can increase reflectivity.

The range of reflected wavelengths is called the stopband (Fig. 1.5), and its range definition is $(1 - R < 2(1 - R_{max}))$. The stopband width depends on the difference between the semiconductor's diffractive indices and the reflected wavelength for which it was designed (Eq. 1.1), but in most cases, it is around 100meV [10]. DBR reflectivity is given by Eq. 1.2. As seen from Fig. 1.6, the

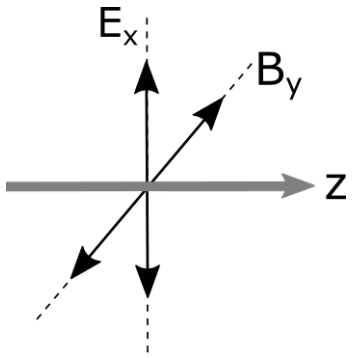

Figure 1.3: Figure showing electromagnetic radiation propagating in the direction of z axis as well as electric and magnetic fields oscillating perpendicularly (transverse).

electric field has a maximal magnitude between distributed Bragg reflector mirrors, but after it penetrates into the mirrors, the magnitude declines within the penetration depth (appearing because of the finite difference between refractive indices) of the DBR, given by Eq. 1.3. Penetration depth is found to be different for transverse magnetic (TM) and transverse electric (TE) polarisations of the light, electromagnetic radiation (Fig. 1.3). For TM polarisation, it increases with increasing angle, and for TE, the relationship is the opposite. This is the cause of polariton modes splitting, identified as TM and TE modes (Fig. 1.4). Splitting varies depending on the angle like $sin^2(\theta_{eff})$. It was shown that energy of TM mode is higher compared to TE [11]. With decreasing cavity length, the importance of penetration depth increases. This is the case, because penetration depth becomes larger than cavity length and because effective cavity length is a combination of cavity length and wave penetration in the DBR [11].

$$\Delta_{sb} = \frac{2\lambda_{sb}\Delta n}{\pi n_{eff}} \tag{1.1}$$

Δ_{sb} - the spectral width of the stopband, λ_{sb} - the central wavelength of the stopband, Δn - the difference between refractive indexes, n_{eff} - the effective refractive index.

$$R = \frac{(\frac{n_b}{n_a})^{2N} - \frac{n_f}{n_0}}{(\frac{n_b}{n_a})^{2N} + \frac{n_f}{n_0}} \tag{1.2}$$

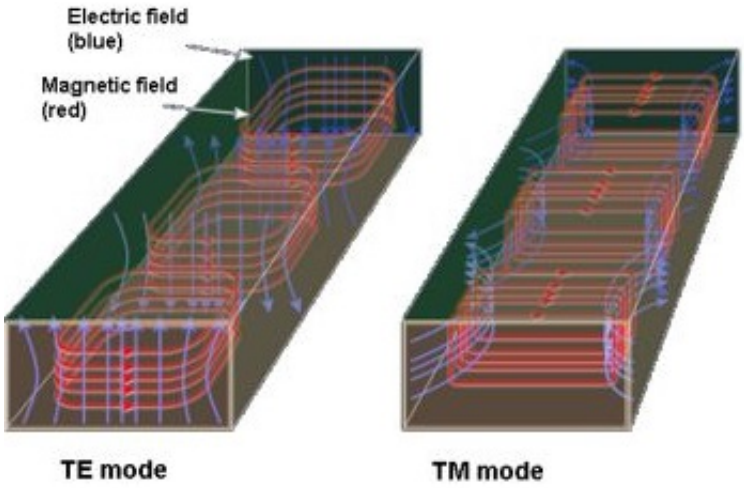

Figure 1.4: Figure taken from [12]. Geometrical representation of the TE and TM modes in terms of the electric and magnetic field vectors.

n_0 - refractive index of the starting material, n_f - refractive index of the final material, n_a and n_b - refractive indexes of alternating DBR materials ($n_a < n_b$), N - number of DBR layers.

$$L_{DBR} = \frac{\lambda}{2n_{eff}} \frac{n_H n_L}{n_H - n_L} \tag{1.3}$$

L_{DBR} - penetration depth of the DBR, λ - the wavelength of penetrating light, n_H and n_L - refractive indexes of DBR layers.

In free space, photon dispersion is found using $\omega = c|k|$ (the photon is massless), but in a microcavity, it becomes $\omega_{m,k} = \omega_{m,0}(1 + c^2|k|^2/n_{eff}^2\omega_{m,0}^2)^{1/2}$- parabolic as the photon becomes quantized in z direction. This change is because in DBR mirrors, only certain wavelengths can be trapped ($k = m\pi n_{eff}/L_{eff}$ corresponding to available wave vectors and energy $\hbar\omega_{m,k} = (\hbar c/n_{eff})(k_m^2 + |k|^2)^{1/2}$, which leads to quadratic dispersion). k wave vector is a vector representing the direction of the propagation of the light. Multiplied by Planck constant it corresponds to the photon momentum. It's physical meaning describes the "spatial frequency" of the light. Large k would mean that the wave has a large spatial frequency and it's phase evolves very fast. k_m is a wave vector in the microcavity direction, whereas $|k|$ represents a wave vector parallel to the microcavities plane.

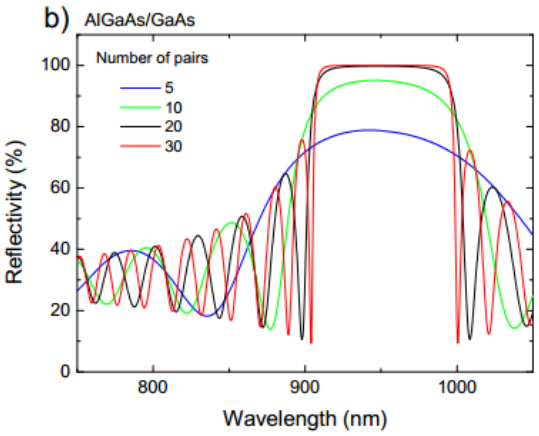

Figure 1.5: Simulated stopband reflectivity of AlGaAs/GaAs semiconductor DBR sample at different wavelengths, with a centre wavelength at 950nm. Simulation was performed for 5, 10, 20 and 30 pairs of DBR layers. It shows that reflectivity increases with a larger number of pairs as well as the stopband becoming more distinct [13].

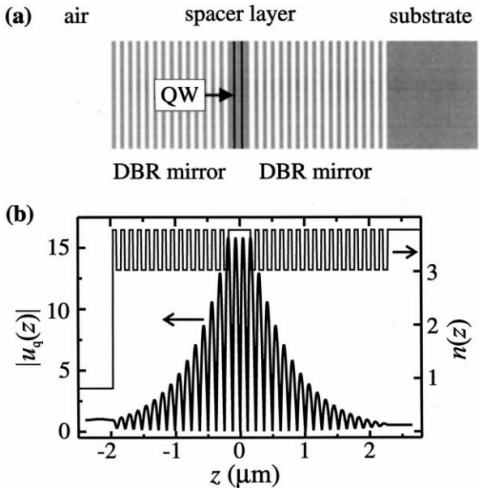

Figure 1.6: a) structure of DBR mirror. The first DBR mirror is grown on a structurally matching substrate. This is followed by a growth of semiconductor spacer layer with QWs positioned at electric field antinodes and finished with a growth of the second DBR mirror b) working principle of DBR mirror. The electric field is concentrated in the cavity, and its strength decreases within penetration length in DBR. Simulation was carried out using transfer matrix method [14].

When comparing an exciton and a photon dispersion, the former looks to be flat, but it is not the case, as exciton dispersion is also parabolic. This happens because of large exciton mass ($m_{ex} = 10^{4-5} m_{ph}$, where m_{ph} is photon mass), and so its curvature is 10^{4-5} smaller than the photon dispersion's curvature, which can be seen by combining two previous equations.

One of the main use cases for semiconductor microcavities is creation of polaritons - investigation of ligght and matter interactions. Light and matter interactions are amplified, because light bounces from mirrors, stays in the cavity longer and can interact more times [15]. Microcavities can be used to change the rate of the spontaneous emission. It could be increased or decreased, depending on the chosen experimental conditions. Such an out come has a name of "weak coupling". A way to successfully obtain it, emitters have to be located at the maximum strength of the electric field, otherwise called the cavity electric field antinode. The Purcell factor is the measurement of the spontaneous emission rate change (Eq. 1.22). In other words, the Purcell effect shows the ratio of emitter's emission rates with and without the microcavity. This factor increases with decreasing cavity size and increasing coupling strength. Microcavities are useful in this case, because the density of photon states can be increased by fabricating their volume to be very small.

$$F = \frac{3Q}{4\pi^2 V}(\frac{\lambda}{n})^3 \tag{1.4}$$

Where Q is quality factor, λ - emission wavelength, V - microcavity volume, n - material refractive index.

The best example of Purcell effect observation is quantum dots (QD), as they have a very small volume (smaller volume means smaller gaps between polaritons and higher nonlinear exciton interaction for comparable power excitation) and high strength of the oscillator. However, as a result of the cavity created around QD without possibility to change it, it's tunability cannot be controlled within big ranges [16]. Maximising quality factor can also lead into enhancement of the Purcell factor (it is harder to get it for visible light, because optical loss increases, so it is increased by increased mirror reflectivity). The quality factor is defined as

an inverse ratio of absorption peak full width at half maximum with absorption peak frequency or as the inverse ratio between the energy lost after every cycle of light and the energy stored in the cavity (Eq. 4). To get a high quality factor, microcavity losses should be reduced, because it depends on the cavity length and the reflectivity of the mirrors, as can be seen in Eq. 1.5. With an increasing number of DBR pairs the quality factor increases exponentially if the cavity has identical DBR layers on both sides.

$$Q = \frac{\omega_c}{\delta\omega_c} \tag{1.5}$$

Where ω_c is mode frequency, $\delta\omega_c$ - full-width-half-maximum (FWHM)

1.2.1 Finesse

Another property of microcavities is finesse. The finesse of an optical resonator (cavity) is defined as its free spectral range divided by the (full width at half-maximum) bandwidth of its resonances Eq. 1.6. It is independent of the resonator length and is fully determined by the resonator losses. This allows the determination of the reflectivity of the DBR mirrors, which in theory depends only on the number of repeating layers [17] and the difference between the refractive indexes of those repeating semiconductor materials. Finesse is related to the quality factor (Eq. 1.5) and is limited by a diffraction [18]. Finesse shows how much light is lost when it circles in the cavity. This is why the highest finesse is found when the cavity length is the smallest, as the light mode covers the smallest area on the mirror, because of light divergence [19].

$$Q = \frac{2\pi n_{eff} L_{eff}}{\lambda(1 - R_1 R_2)} = \frac{n_{eff} L_{eff} F}{\lambda} \tag{1.6}$$

Where n_{eff} is effective refractive index, L_{eff} - effective cavity length, λ - wavelength, R_1 and R_2 - DBR reflectivity.

$$F = \frac{\delta\omega_c}{\sigma\omega_c} = \frac{\pi\sqrt{R}}{1 - R} \tag{1.7}$$

At first it was thought that an atom, quantum dot or a molecule has an intrinsic property of spontaneous emission. This was disproved by putting the emitter into a cavity. A cavity changes the density of states into which an atom can emit, thus changing spontaneous emission properties by enhancing or suppressing them. A microcavity also causes the decay to be directional, because modes are enhanced towards the resonator [20]. Free space density is overcome by the maximal modes density at the quasi-mode resonant frequency, as noticed by Purcell [7].

1.2.2 Weak Coupling

The regime of weak coupling, also known as Purcell effect, is the regime in which an emitter is weakly coupled to the cavity mode, and the emitted light escapes the cavity before being reabsorbed by the emitter. Photons and excitons are coupled weakly, and the probability of the reabsorption is very small. From this follows that the condition for the weak coupling can be described as the decay rate of the cavity's electric field (κ, depending on the quality of the mirrors and their Q-factor) exceeding coupling strength of the emitter-cavity ($g = (\frac{\hbar^2 2\pi e^2 f}{4\pi\epsilon_0 m L_{eff}})^{\frac{1}{2}}$), which for a single quantum well depends on oscillator strength, f, particle mass, m, and effective length, L_{eff} [21]) and the atom's free space spontaneous emission rate (γ), $\kappa >> g, \gamma$ [13]. Proportionality of the described spontaneous emission to the photon density of states is shown by the Fermi's golden rule (Eq. 1.8).

$$W = \frac{2\pi}{\hbar^2}|M_{12}|^2 g(\omega) \tag{1.8}$$

Where $g(\omega)$ - the density of states, M_{12} - transition matrix element.

The emitter, which can be a quantum dot (semiconductor particle of several nanometres size) or a real atom, under circumstances that external field source is not present, free-space, using standard equation of photon states in free space and the average obtained from all possible orientations of the atomic dipole. The density of states for the microcavity polaritons are defined as the gradient of the dispersion relation for the k values or dE/dk otherwise. The used formulas for

the density of states and the transition matrix element are as follows:

$$g(\omega) = \frac{\omega^2 V_0}{\pi^2 c^3} \quad \text{and} \quad M_{12}^2 = \frac{\mu_{12}^2 \hbar\omega}{6\epsilon_0 V_0} \tag{1.9}$$

In which case the transition rate for spontaneous emission becomes:

$$W^{free} = \frac{1}{\tau_R} = \frac{\mu_{12}^2 \omega^3}{3\pi\epsilon_0 \hbar c^3} \tag{1.10}$$

The transition rate for spontaneous emission is influenced by the lifetime of a photon in the cavity. This rate is noticeably changed if compared to the cavity from the free space case. A few assumptions are made to find spontaneous emission in these conditions: first of all the atom is contained in a single-mode cavity and secondly, it has only two energy levels. In these conditions, there is only one possible way for the integral of density of states function over all possible frequencies to be equal to one, which is required:

$$g(\omega_0) = \frac{2}{\pi\delta\omega_c} \frac{\delta\omega_c^2}{4(\omega_0 - \omega_c)^2 + \delta\omega_c^2} \tag{1.11}$$

The matrix element will be, if ϵ is normalized dipole orientation factor:

$$M_{12}^2 = \xi^2 \frac{\mu_{12}^2 \hbar\omega}{2\epsilon_0 V_0} \tag{1.12}$$

The rate of spontaneous emission becomes Eq. 1.13, if everything is combined in Fermi's rule.

$$W^{cav} = \frac{2Q\mu_{12}^2}{\hbar\epsilon_0 V_0} \xi^2 \frac{\delta\omega_c^2}{4(\omega_0 - \omega_c)^2 + \delta\omega_c^2} \tag{1.13}$$

The ratio between the rate of spontaneous emission in the cavity and in free space gives the equation for the Purcell factor, which looks like:

$$F_p = \frac{W^{cav}}{W^{free}} = \frac{3Q(\frac{\lambda}{n})^3}{fzpi^2 V_0} \xi \frac{\delta\omega_c^2}{4(\omega_0 - \omega_c)^2 + \delta\omega_c^2} \tag{1.14}$$

If the dipoles are aligned in the direction of the field and the system is in resonance, then the previous equation is reduced to the Eq. 1.22. In case of $F_p > 1$, the rate of the spontaneous emission increases after an atom is placed in the microcavity and the lifetime of a photon has decreased in the cavity [22]. In the opposite case, the density of states has decreased, and spontaneous emission becomes slower. In the weak coupling regime, photons escape the cavity quicker than they are absorbed by the matter inside it. Observation of the Purcell factor requires a 0D photonic environment, high Q, low mode volume, an emitter placed at an antinode, a dipole oriented parallel to the vacuum electric field and $Q_{emitter} > Q_{cavity}$. It was already achieved using quantum dots placed in microresonators ([23]), micropillars ([24]) and photonic crystal microresonators ([25]).

1.2.3 Strong Coupling

The condition for the strong coupling is $g >> \kappa, \gamma$. It requires the emitter - cavity coupling strength to be much greater than the free space spontaneous emission rate and the decay rate of the electric field in the cavity [13]. So the emitted photon could be reabsorbed by the emitter and does not leave the microcavity before this effect, which is opposite how the weak coupling behaves. Because of the energy jumping between the emitter and the cavity, new eigenstates are created, as proven by [26]. In this case, hybridisation between the cavity mode and the cavity emitter appears, which is followed by the formation of new states, so-called polaritons. Strong coupling is recognized by the appearance of energy splitting between polariton states (splitting depends on the effective cavity length, the exciton oscillator strength and the number of quantum wells [27][28]), called Rabi splitting ($\delta E \propto 1/(L_{eff})^{\frac{1}{2}}$). (In other words, Rabi splitting determines the period of energy oscillation between the exciton and photon mode). There is a second condition - the peak width should be smaller than the energy splitting; any other way, it cannot be visible. The emitter has two energy levels, the ground state and the excited state, which leads to the mentioned splitting. One of the photon levels, in the case of one photon being in the cavity, interaction with these two levels causes the splitting to appear, as shown in Fig. 1.7. As for resonance

(resonance is a condition in which the photon wavelength is exactly the same as the exciton emission wavelength), it's wavefunction is shown in Eq. 1.15, which can be described as a superposition of excitonic and photonic wavefunctions [17]. To simply explain it, energy is oscilating between the mentioned two levels (exciton and cavity photon), creating a quasi-particle named a polariton, which has a frequency of $\Omega_R/2\pi$, with the Ω_R being described in the Eq. 1.16. If a two-level system is driven off resonance, then a generalised equation is used Ω_R^G (1.17). Mentioned phenomenon is termed Rabi oscillation. Rabi oscillation can be explained using two harmonic oscillators, in the classical way [29]. In the traditional case, discussed oscillators have oscillation frequencies as shown in Eq. 1.18.

$$\phi = \frac{1}{\sqrt{2}}(\phi_x + \phi_p) \tag{1.15}$$

$$\Omega_R = \frac{g\mathcal{E}}{\hbar} \tag{1.16}$$

Where g is the strength of the dipole coupling/transition matrix element, $\mathcal{E}$ is the electric field amplitude of the laser.

$$\Omega_R^G = \sqrt{\Delta^2 + \Omega_R} \tag{1.17}$$

$$\omega_1^\circ = (\frac{k_1}{m_1})^{\frac{1}{2}} \quad and \quad \omega_2^\circ = (\frac{k_2}{m_2}^{\frac{1}{2}}) \tag{1.18}$$

In the strong coupling regime, coupling between oscillators, which is denoted with a constant κ and changes the formulas of the oscillators' motion into Eq. 1.19.

$$m_1\ddot{x}_1 + k_1x_1 + \kappa(x_1 - x_2) = 0 \quad and \quad m_2\ddot{x}_2 + k_2x_2 - \kappa(x_1 - x_2) = 0 \tag{1.19}$$

Where m, k and x are masses, spring constants and positions of two oscillators. κ - coupling strength between these oscillators.

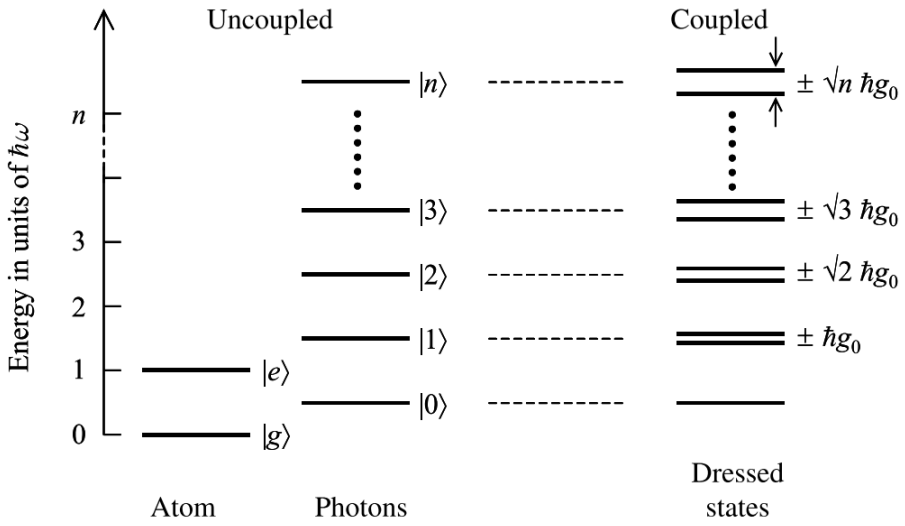

Figure 1.7: Energy levels for different situations. Strong coupling energy level splitting appears because the atom has ground and excited energy levels.

With solutions below:

$$x_{1,2}(t) = x^{\circ}_{1,2} exp[-i\omega_{\pm}t] \tag{1.20}$$

$$\omega^2_{\pm} = \frac{1}{2}[\omega_1^2 + \omega_2^2 \pm \sqrt{(\omega_1^2 - \omega_2^2)^2 + 4\Gamma^2\omega_1\omega_2}] \tag{1.21}$$

Where $\omega_1 = \sqrt{(k_1 + \kappa)/m_1}$, $\omega_2 = \sqrt{(k_2 + \kappa)/m_2}$ and $\Gamma = \frac{\sqrt{\kappa/m_1}\sqrt{\kappa/m_2}}{\sqrt{\omega_1\omega_2}}$ represents frequency anticrossing.

Establishing $m_1 = m_2 = m_0$, $k_1 = k_0$ and $k_2 = k_0 + \delta k$. Changing δk in the range from -k_0 to k_0 indicates that energy level, or frequency, curves shows anti-crossing pattern as in Fig. 1.8b and Fig. 1.9 (real measurement data), moreover in the weak coupling regime, the previously mentioned photonic and excitonic curves cross at $\delta k = 0$, which can be seen in Fig. 1.8a [18]. It was observed that anticrossing splitting increases (energy level deviation in coupled case, compared to uncoupled case) when excitons (the exciton energy level can be changed by altering the quantum well width) and photons (the photon energy is changed by changing cavity width) energy and momentum values get closer to the res-

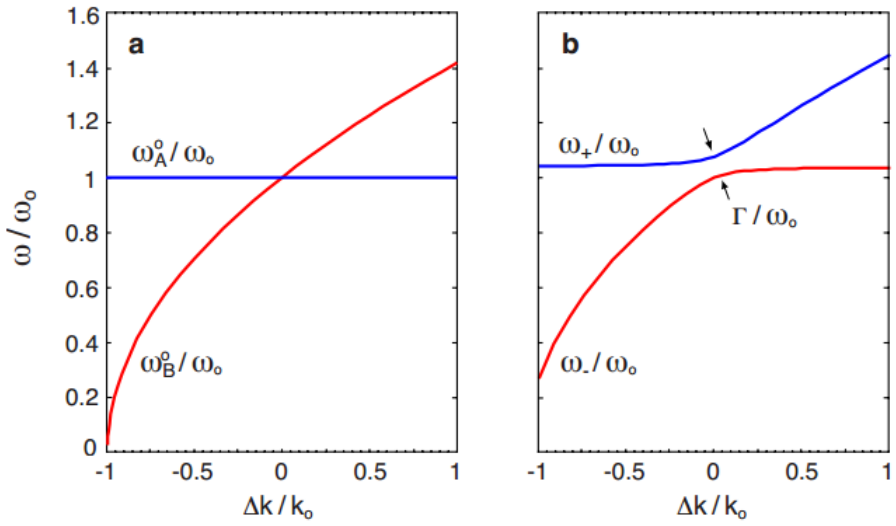

Figure 1.8: Frequency ratio versus the ratio between spring constant difference and the maximum value of the spring constant. Strong coupling explanation in the classical way, using two harmonic oscillators. The strong coupling regime is identified as an anti-crossing between the exciton and photon dispersion curves. It is quantized by a Rabi splitting, the energy difference between the strong and weak coupling cases. a) Figure showing ratio of frequencies for two uncoupled oscillators. b) Figure showing ratio of frequencies for two coupled oscillators [29].

onance, reaching the greatest amount at the crossing point [30]. The strong coupling regime has a condition that the linewidths of photons (this occurrence depends on the reflectivity of DBR, the cavity length and the cavity refractive index [10]) and excitons should be smaller than the Rabi oscillations [17], as otherwise it could not be observed. Strong coupling appearance when phonons are in resonance with excitons can also be seen in this graph (quantized crystal atomic vibrations). This is demonstrated using Eq. 1.16 when increasing detuning (found using the following equation: $E_{cav}(k=0) - E_{exc}(k=0)$) value increases the Rabi frequency, in consequence this can be understood as the electrons being able to jump between two energy levels more quickly as the difference between those two levels decreases. In other words, the cavity modes or the frequency of the light waves captured in the cavity, are equivalent to the emitter's frequency.

Polaritons are a linear combination of excitons (electrons and holes paired by Coulomb interaction) and photons, which might form, for example, into quantum

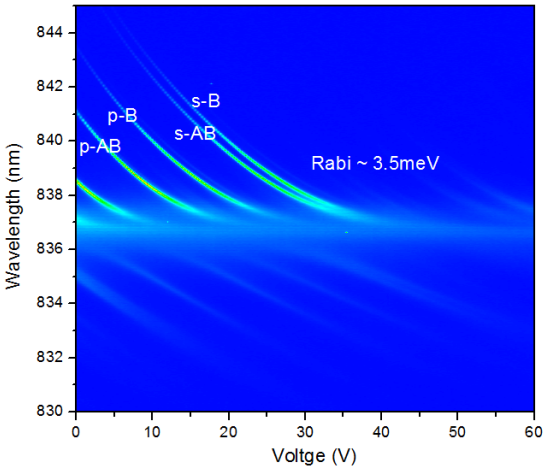

Figure 1.9: Polariton wavelength versus piezo voltage corresponding to the increase of the cavity length. Anticrossing plot taken from real measurements using a coupled open-cavity sample. The observed Rabi splitting is 3.5meV. This figure also shows the mode splitting into bonding and anti-bonding modes, which appears because of coupled concave mirrors. The longitudinal mode is the brightest in the centre, with higher order modes on the left and right (they are very weak because they come from different longitudinal modes).

dots. A quasi-particle can be considered as a particle, because it is a quantum of energy that has position and momentum. Some of the most interesting polariton properties are very low effective mass and strong nonlinearity [17]. Nonlinearity emerges because of the two-level nature of the emitter, which corresponds to an anharmonic (higher frequencies are not multiples of the lowest frequency) energy-level diagram (a Jaynes-Cummings ladder). Because of this nature, the energy required to create a polariton depends on the number of polaritons already in the system, giving strong nonlinearity [31]. Polariton wave function can be obtained from the following expression: $\varphi_{pol} = |X|\varphi_X + |C|\varphi_C$, with C and X being Hopfield coefficients corresponding to the exciton and photon fraction in the polariton. Hopfield coefficients can be calculated by:

$$X^2 = \frac{\delta + \sqrt{\delta^2 + \Omega^2}}{2\sqrt{\delta^2 + \Omega^2}}, C^2 = -\frac{\delta - \sqrt{\delta^2 + \Omega^2}}{2\sqrt{\delta^2 + \Omega^2}} \tag{1.22}$$

Where δ is detuning and Ω is Rabi splitting.

The resonance condition is fulfilled when Hopfield coefficients are equal. Following this, in the resonant case, polaritons are half excitons, half photons [32][33]. Coupling between the photon and exciton appears, because two fermions (electron and hole) join together to create a boson (two half-integer-spin particles together sums up to an integer-spin particle), which can then interact with a photon, a boson itself. Polaritons were observed in the microcavity in 1992 for the first time [34].

Certain selection rules determine if excitons interact with light. GaAs has two types of holes: heavy holes and light holes. Light holes have an angular momentum of $\pm\frac{1}{2}$, because spin projection is anti-parallel to the mechanical momentum projection. Heavy holes have an angular momentum of $\pm\frac{3}{2}$, because the spin projection is parallel to the mechanical momentum projection. In bulk material, these states are degenerate, but the degeneracy is removed in quantum wells, because of the quantum confinement in one direction. Electrons can have only $-1/2$ and $+1/2$ states. As an exciton is formed from an electron and the hole, it can have total angular momentum projections of ±1 and ±2. A photon is a boson and has a spin of 0 and ±1, which means it interacts only with excitons, which have ±1 spin; the described exciton fits this condition. On the other hand, if the exciton is formed with ±2 spin, it cannot interact with photons. Excitons that interact with photons are called "bright excitons", and the ones that do not are called "dark excitons". Excitons directly scatter with the same spin excitons, while opposite spin excitons scatter through dark exciton states [30]. Because of the non-degeneracy in QWs, polaritons are formed from heavy holes and electrons, a combination which gives a total angular momentum projection of ±1.

Polaritons get their small mass from photonic wavefunction ($10^{-5}m_e$), seven orders of range, and self-interactions from excitonic wavefunction, as the photon-coupling cross-section is very small and their interactions appear through other systems [35]. Other properties of polaritons include long coherence and fast dynamics coupling to external light [36]. A polariton's linewidth depends on its excitation power, and the linewidth tends to increase with increasing power

because of spectral diffusion [37][38] and exciton-exciton interaction. Diffusion and exciton oscillator strength decrease due to exciton bleaching, causing strong coupling loss at a high excitation power. The coupling regime depends on g, γ_x and P (phase diagram) [39]. Polaritons derive many properties from the exciting light, such as their spin and dipole moment.

1.2.4 Two-Dimensional Polaritons

The previously mentioned polaritons are a result of 0D single emitters, which deal with discrete states. In contrast, a quantum well in a microcavity deals with a continuum of 2D states: 2D exciton and 2D cavity modes (Fig. 1.10). The difference in a created polariton will be that it will form anticrossing dispersion curves. The size of this anticrossing again depends on the Rabi splitting, which could be increased if the cavity length is decreasing, placing QWs on the antinodes of the cavity field and increasing the quantity of QWs. The coupling strength of the particle is equal to: $V = (\frac{e^2 N_{QW} f_{OSC}}{2\epsilon_0 m_0 n_c^2 L_c})^{\frac{1}{2}}$ (where N_{QW} is number of QWs, f_{OSC} - oscillator strength, L_c - effective cavity length, n_c - refractive index of the cavity) [40]. As the equation shows, the coupling strength increases with an increasing number of QWs (the photon can interact with more excitons), the oscillator strength (the interaction is stronger between excitons and photons) and a decrease in the cavity length.

1.3 Bose-Einstein Condensate

The Bose-Einstein condensate (BEC) was theoretically described by Bose in as early as 1924. BEC is a phase transition occurring when particles start to fill the lowest energy state Fig. 1.11. This transition appears in systems that can be characterized by Bose-Einstein statistics, which involves indistinguishable, bosonic particles with integer spin, for example $0, 1, 2$.

The transition in 3D systems appears when the temperature becomes lower than the critical temperature (T_c): $T_c = (\frac{2\pi\hbar^2}{mk_b})(\frac{n}{g_{3/2}(1)})^{\frac{2}{3}}$ (where m is particle mass, n - particle density and $g_{3/2}(1)$ - Riemann Zeta function) [30]. The equation shows

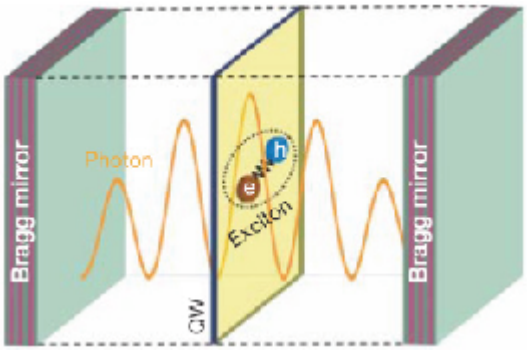

Figure 1.10: Figure taken from [41]. Inside the microcavity, light waves of certain frequencies are trapped between the DBR mirrors, corresponding to the cavity modes. A photon of light excites the exciton in the QW, which recombines, emitting a photon. If this process repeats often enough before the photon escapes the microcavity, a polariton is formed.

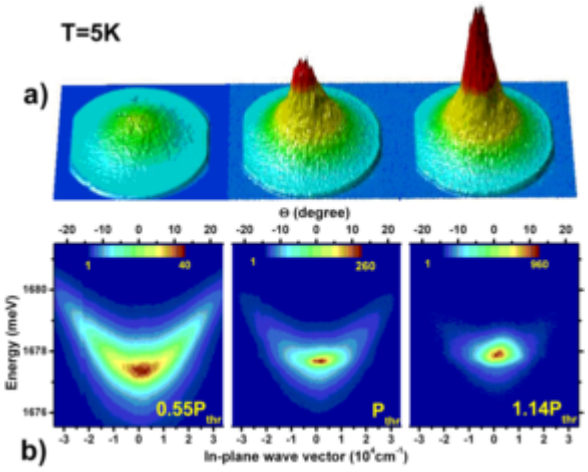

Figure 1.11: System transition to Bose-Einstein condensate. The first row presents how the number of particles occupying a particular region in space changes, and the bottom row presents how the number of particles at a particular energy level changes. With increasing power, more and more particles move to the lowest energy level even after passing the transition power [42].

how critical temperature depends on the mass (the polariton mass depends on the LPB slope, and so it can be changed by changing detuning; the smaller the slope, the larger the effective mass is: $m_p = \hbar(\frac{d^2\omega^{LPB}(k)}{dk^2})^{-1}$). $50\mu K$ temperature [43] is required to condense the lightest element - Hydrogen. Luckily, polaritons get mass from photons; hence, they are so light that condensation can appear at room temperature [44][45], and at low density, they obey bosonic statistics. However, this is possible only in a 3D or more dimensional environment (the problem is that most atomic gases become solid before reaching critical temperature), whereas in 2D (or less), Bose-Einstein condensate appears at a temperature of 0K.

A condensate can appear not only in the equilibrium as the BEC definition was changed to be described by the order parameter, spontaneous symmetry breaking and macroscopic coherence [10]. So 0K BEC can be overcome by achieving a quasi-condensation below the temperature of the Berezinskii-Kosterlitz-Thouless (BKT) transition [46]. BKT is a macroscopically occupied state in 2D with long range coherence, which does not extend to infinity, but decays by algebraic order due to the formation of bound vortex-antivortex pairs.

As mentioned, the coherence length of such equilibrium does not reach infinity, but is still very large. Also depending on dimensionality, critical density is finite ($d > 2$) or infinite ($d \leq 2$) with the chemical potential not becoming zero [10]. In such systems, particles overfilling the critical density go into the ground state [17], with a density of: $n_0(T) = n(T) - n_c(T)$. Critical density is found from: $N_C = (\frac{V}{\lambda_T^3})g_{3/2}(1)$. It therefore depends on the mass and volume. Quasi-condensation is achieved in positive detuning [47][48][49], and metastable condensation in negative detuning [49][50].

Condensate wavefunction depends on the interaction with the reservoir of uncondensed excitons. In addition, its polarisation depends on exciting pump polarisation and relaxation mechanisms as these properties constantly change because of the magnetic field (it affects excitons in quantum wells and thus polaritons as well), scattering and defects, and other factors [17]. The condensation linewidth is inhomogeneously broadened by laser intensity fluctuations as it changes the

number of condensing polaritons [51].

Non-resonant pumping appears when the system is pumped above the upper polariton branch (UPB). The system then forms a high density of coherent free hot carriers (excitons) region, which relaxes to the lower polariton branch by longitudinal optical (LO) phonon interaction and exciton scattering [52]. This happens on a sub-picosecond time scale. Then it continues relaxing towards the lowest energy level by polariton-polariton and polariton-acoustic phonon scattering. It might also scatter to the high k vector LPB branch by acoustic phonon interactions. The dominant mechanism depends on the excitation power and detuning. Relaxation to the lower k-vector region occurs by polariton-acoustic phonon scattering, polariton-polariton interaction and polariton-free carrier interaction [53].

This process works well in the high k-vector range (high angle) as relaxation time is around 1ns, the excess energy is around a few meV and the relaxation steps take 10ps to waste around 1meV of energy [10]. In the low k-vector region, the polariton lifetime becomes 5ps (because of the steepness of the LPB curve which depends on the exciton fraction. Eq. 1.23) and has to lose 5-10meV. In this region, the previous relaxation steps no longer function as to reach the bottom would take at least 50ps (longer than the polariton's lifetime). Few polaritons relax from exciton-like to photon-like, and so there is a greater occupancy at k-states near exciton energy (Fig. 1.12). This situation is called the "bottleneck effect" (Fig. 1.13).

In this region, which lasts only a few picoseconds, the exchange of a few meV energy polariton-polariton scattering becomes more important. In this elastic scattering, one polariton loses energy and momentum, while another one receives it in the same amount. This forces one polariton to go to the low k vector energy and another one to the high k vector energy. Energy could also be wasted through polariton-free carrier interaction, which appears in a sub-picosecond time scale. Free carriers exchange more energy during interaction with polaritons, compared

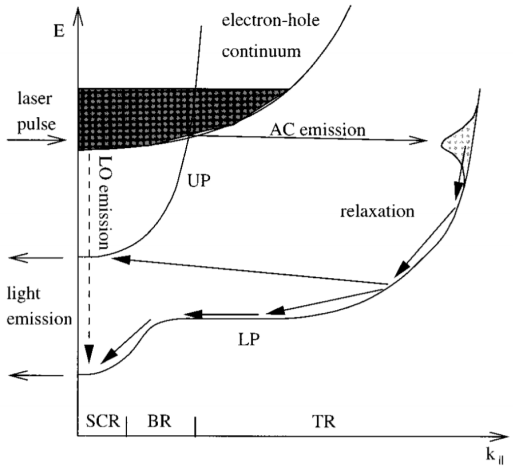

Figure 1.12: Figure taken from [54]. Energy versus in-plane wave number. This sketch illustrates the polariton formation processes from an exciton reservoir created by non-resonant excitation. It can follow two paths: a scattering process by acoustic-phonon emission, or radiative recombination and absorption. Meaning of abbreviations: BR - bottleneck region, LP - lower branch, UP - upper branch, TR - thermal region and SCR - strong coupling region, angular region of good mirror reflectivity and observed emitted luminescence.

to excitons, because of their lower mass [53].

$$\Gamma_k = \frac{|C_k|^2}{\tau_c} \tag{1.23}$$

Equation showing the relationship between polariton lifetime, exciton fraction and photon lifetime in the region of k-vector between 0 and inplane wavevector. Here Γ_k is the polariton lifetime, $|C_k|$ - the Hopfield coefficient, τ_c - the cavity photon lifetime.

Non-resonant excitation makes it harder to identify polariton-polariton interactions in the condensate and distinguish them from interactions with the reservoir of uncondensed excitons [55]. The bottleneck effect appears because the dispersion drop reduces the polariton lifetime to about 5ps [30], and all scattering effects take longer. As the photon fraction increases, the lifetime becomes shorter. Nonetheless, in very good cavities, photon lifetime as high as 100ps can now be achieved. Also, because polaritons become more photon-like, they scatter less effi-

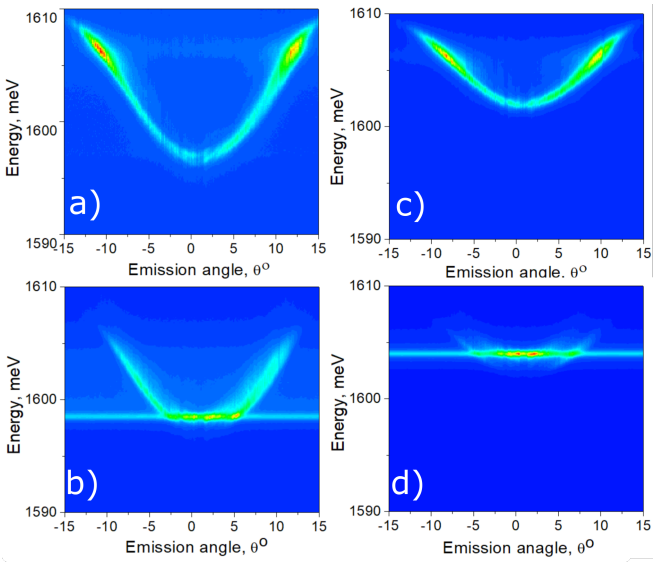

Figure 1.13: Polariton photoluminescence intensity dependence on polariton energy and the emission angle of the sample. a) and c) show the bottleneck effect at different detunings using 1mW excitation power of a 635nm laser. Polaritons are stuck at high k vector energies. b) polariton lasing was achieved at a higher power (64mW) compared to d) (55mw), because of greater negative detuning. b) a situation in which polaritons had to lose more energy to condense at k=0.

ciently with phonons, since this scattering is proportional to the exciton fraction. All these effects make polaritons collect at k-states near exciton energy. This is why this effect is observed only in negative detuning, when the dispersion curve is steeper. To suppress the bottleneck effect, the number of scattered polaritons in the lowest energy state should increase. This is done by increasing excitation power, resulting in an increase of exciton density as well as polariton-exciton and polariton-polariton scattering. This process helps polaritons to lose their energy and relax to lower k-vectors [54][56]. This can be achieved using either resonant or non-resonant excitation.

Stimulated scattering to $k = 0$ appears if the occupation of this state becomes greater than 1, because of bosonic properties. Bosons have a property that as soon as there is at least one boson in the energy level, stimulated scattering is activated and other bosons will start scattering into it at an increased rate of $N + 1$ [57]. Therefore, the higher the occupancy of the state, the higher the transition rate is into this state. This process is called bosonic final state stimulation, leading to BEC [10].

But with increasing power, Coulomb interaction starts to play a greater role. Because of the higher density of polaritons, as they have fermionic nature, this change blueshifts the lower polariton branch emission. At some point, the strong coupling regime (as excitons are ionized) is lost, and weak coupling appears. Samples in which excitons have a large binding energy and samples with a higher number of quantum wells are required to maintain the strong coupling regime at high pump powers. In samples containing a big quantity of quantum wells, the Rabi splitting is greater, whereas exciton density is distributed over the number of quantum wells, so that the threshold for exciton bleaching is increased ([40] [47]).

An emission at a particular energy of the ground state is one of the BEC's signatures. Another is a k-space narrowing of the total emission attributed to the increased long-range spatial coherence and superfluid behaviour [58][59]. Strong coupling can also be lost by a temperature increase. The short lifetime of the

polariton does not allow it to reach semi-classical condensation [60], because its lifetime is too brief for the settlement of the thermal equilibrium with crystal lattice. However, this limitation changes after observation of 100ps lifetimes [61]. This allows polaritons to move by around a millimetre.

The bottleneck effect can also be suppressed by changing detuning (a shallower LPB slope increases the polariton lifetime, LP-LP scattering rate dependence $\propto \alpha_{ex}^2 \rho(E)$) or by resonant pumping [62]. Small and powerful non-resonant excitation can push condensation out from the excitation spot, because the potential is changed by the interaction between polaritons and the high-density exciton reservoir (the exciton diffusion coefficient is small), as achieved in micropillars [63].

Resonant pumping appears when excitons are excited on the LPB branch (the laser energy is chosen to be at the same energy as LPB at chosen angle). Resonant excitation requires lower power to achieve condensation, because they do not have to scatter from exciton reservoir to LPB. The bottleneck effect is also suppressed in this case.

Resonant excitation enables two new mechanisms for BEC formation. The first is called optical parametric amplifier (OPA) and requires an additional probe at k=0, which triggers bosonic state stimulation. The second mechanism is called optical parametric oscillator (OPO). It involves resonantly exciting LPB at a particular energy-momentum pair. Polariton-polariton scattering from the pump to $k = 0$ and $2k_{pump}$ states will result in macroscopic occupation of the mentioned two states, which are called "signal" and "idler" respectively.

1.4 Polariton Lasing

An emerged BEC allows an effect called a "polariton laser", which requires a threshold 100 times lower than a photon laser in the same structure [64]. These two mechanisms are different, because in a polariton laser, the scattering and not emission is stimulated. The Polariton laser threshold is also 100 times smaller

in the case of a linearly polarized pump laser, compared to a circularly polarized one (the same occurs in a photon laser, because the cavity resonance is not the same for TM and TE light). In the case of multimode lasing, interactions come only within the same mode, and so blueshift does not depend on the occupancy of other modes.

In [65], it was found that blueshift depends on occupancy logarithmically, whereas linear behaviour is predicted by theoretical calculations. Polariton lasing was proved by [55], when in their experiment the second threshold lasing was coming from an exciton reservoir and not from the expelled polariton condensate. A polariton laser has a very weak absorption at emission wavelength [17], because the required scattering separates absorption and emission. In photon lasers, in contrast, these two processes are connected. A polariton laser does not need to achieve carrier inversion because of bosonic properties. After one polariton gets into the lasing state, the further scattering process is triggered into this state. Polariton lasers work until strong coupling is lost. Polariton laser is supported by the following required properties: the nonlinear intensity change, a sharp decrease in linewidth and a continuous increase in blueshift.

1.5 Methods of Lateral Confinement of Polaritons

The semiconductor microcavities have a lack of ability to tune the energy of the cavity modes over significantly large ranges, which is the biggest negative side of it. There are couple ways to achieve tunability in small ranges. One of them is thermal tuning, which changes cavity by only a few meV after applying around 50K temperature change [18]. The second method is to incorporate a p-i-n junction. It uses a quantum-confined Stark effect to tune the sample by a few meV. This effect works as follows: in electric field presence, the hole energy increases and electron energy decreases, thus changing the energy of the exciton. This method has additional consequences as electrons and holes are pushed to opposite Quantum Well sides. The overlap between them decreases as well as

the recombination efficiency. Other methods, such as adsorption of gases or condensation of inert gases, might be used, but these are very slow and adsorption is an irreversible process [66].

A photonic crystal cavity containing a Quantum Dot allows reaching very small mode volumes (a diameter of around 2-10 nanometres can be achieved), which gives a high photon and exciton coupling strength, but it suppresses tuning and reduces the quality factor. Quantum dots are favoured because they are almost perfect two-level systems (it requires some time to relax after excitation, in order that it could be excited again), have large dipole moments, are fixed in space and can be controlled by voltage or an electric field. Heating can still be used, but it is a very slow method and has a small range of tunability, because at higher temperatures QD linewidth increases due to phonon scattering, which increases with rising temperature [16].

Another type of microcavities are pillar microcavities (Fig.1.14). Pillar microcavities are another way of confining cavity modes in the plane, just as in an open cavity with a concave mirror. Its structure is the same as in the full cavity, but with small dimensions in x and y directions. Light is confined in the micropillar in x and y directions because the semiconductor refractive index is bigger than the refractive index of surrounding air and light bounces back from the boundary into the semiconductor (this phenomenon is called total internal reflection). Micropillar losses increase with decreasing diameter, because surface roughness starts to play a greater role as post-growth etch does not produce an atomically smooth surface.

Another way to achieve confinement in the microcavity would require creating periodic potentials over the sample. The first idea is to chemically etch the sample surface [65][67], but this method has a drawback. The potential cannot be tuned and forbids research of interaction effects, so a surface acoustic wave (SAW-tuneable wave travelling through the surface of the material, which changes volume, refractive index, lattice parameters and band gap [68] proportionally to the intensity) device was introduced on the sample (Fig. 1.15). This would form

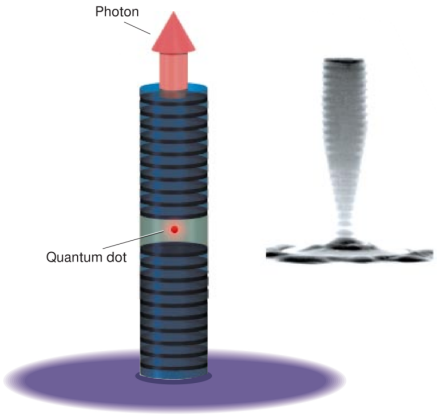

Figure 1.14: Figure taken from [1]. A schematic picture of a micropillar is shown on the left and its cross-section after growth and etching. A micropillar is simply a microcavity that is small in plane dimensions.

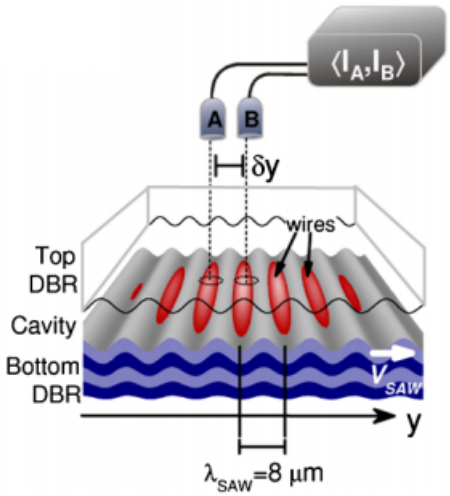

Figure 1.15: Surface acoustic waves induced in the microcavity using a SAW device placed on top [42].

an oscillating strain potential. In exceptional circumstances it would separate atoms appearing in the Bose-Einstein condensate into an array of sub-μm-wide wires [69] aligned along SAW potential minima and traveling at acoustic wave velocities because of their dynamic nature. Use of a second, perpendicular device would create confinement in all three dimensions. SAW energy is lost within the SAW wavelength into the material [68], which limited confinement size because of small penetration in previous experiments [42][70]. Also, application of SAW broadens and flattens k space emission, because of small dimensions and application of Heisenberg's uncertainty principle ($\Delta k \frac{\pi}{\delta y} \frac{2\pi}{\lambda_{SAW}}$). On the other hand, it does not affect pump rate and losses as SAW power does not change condensate emission [42].

SAW is created by inter digital transducers (IDTs) placed on top of the sample, which is made out of metal electrodes. The SAW wavelength and field width depend on their parameters. SAW effects material in two ways: 1) the conduction and valence bands oscillate out of phase (does not allow for the exciton to

dissociate at high SAW power), which is strain induced, created by a propagating SAW, which does not carry a piezoelectric field; 2) the conduction and valence bands oscillate in phase (because of changed modulation, created holes and electrons are separated spatially, and so excitons are dissociated at high SAW power. Crystals without a centre of inversion, like ZnO, GaAs, GaN, follow this path), which is induced by a piezoelectric SAWs. This effect could be created using metallic grating, but it would not be possible to tune it.

In the work of [42], surface acoustic waves (SAW) were used to achieve wire-like condensates moving with acoustic velocity. In this experiment, a 37 MHz frequency SAW generator device was placed on the surface of the full cavity, which limited the used frequency range. This occurs because only long wavelengths of SAW can be used in the case of full, solid microcavity, since penetration of SAW into the sample is on the SAW wavelength scale. Polariton modulation is created because polariton energy is spatially modulated along the SAW propagation direction through two mechanisms. First, the quantum wells' band gap potential is modulated. Second, microcavity resonance energy is modulated in-phase. The vacuum gap between DBRs could place it straight on the bottom DBR, which in consequence would allow the use of higher frequency waves (around 2 GHz) with applied acoustic potential where it is needed (theoretically, it has to be applied to QWs and not to DBRs). This allows investigation of the BEC and work towards a single photon emitter.

Because of polariton wire formation, long coherence is lost, but in presence of a high condensate density, coherence is restored again. Coherence can be varied by a change of SAW power. This is explained by the change in tunnelling between two close wires, which leads to a separate phase change. The phase does not depend on the excitation laser phase [71], which shows spontaneous U(1) symmetry breaking [72] when condensation appears. Coherence reduction in the direction perpendicular to the SAW travel direction comes from 1D polariton phase-fluctuation phenomena [60][73]. Coherence can be increased by the increased excitation power (which increases coherence in x and y directions) as increasing polariton-polariton interaction blueshifts energy and finally overcomes

the confinement energy (more pronounced at low SAW powers).

1.6 Polariton Blockade in a Single 3D Cavity and in Coupled Cavities

At the moment, the main reason behind the need for a single photon source is quantum information science. It has been shown that using this type of light, compared to classical light, will allow a better performance of some type of calculations. Another use is a guaranteed, unconditional security in communication. This requires information encoding using quantum states such as momentum and polarization.

Single photon sources are important because they emit photons one by one, with equal gaps between them, whereas thermal or chaotic light sources tend to have greater joint photon detection. Light coming from single photon source is called antibunched.

A single photon source device could be developed using an open microcavity device with embedded QWs, where polaritons are formed. This device could be an improvement to the quantum dots (QDs), which are used in the current technology as well as nitrogen vacancy centres in diamonds ([74]), single molecules ([75]), and so on. The emission wavelength of QDs cannot be predicted because of the method of their growth and the three dimensional confinement, whereas it should be possible to prepare arrays of 0D microcavities with QWs as an active media, where polaritons emit at the same energy.

One possible way to achieve antibunched light is to use a polariton blockade, a nonlinear optical process appearing because of the nonlinear polariton-polariton interactions that do not allow a second polariton to get into the cavity. This can be explained by a simple example of the single cavity mode characterised by an optical nonlinearity (U) and cavity linewidth γ. $U > \gamma$ is a required condition in this situation. Optical nonlinearity means that injection of the single photon into the cavity moves the mode energy by U amount.

The polariton blockade process can be explained as follows: If resonant excitation is used, after the first photon gets into the cavity, mode energy is moved out of the resonance with the laser and a second photon cannot be injected. The result is only one photon in the cavity, permitting the creation of a single photon source. This effect strongly relies on the strength of the polariton-polariton interaction. One way to achieve the required nonlinearity is by using a very small quantum box with parameters of 200nm. It is impossible to achieve such sizes at present. In microcavities, nonlinearity is high, but the energy shift is small because polariton interaction is still too small for this effect to appear [36].

Coupled cavities are a way to get a single photon source using the polariton blockade process, because of the appearing quantum interference effect, which is not observed in single cavities. This method should also create anti-bunching even with a weak Kerr nonlinearity ($U << \gamma$) in 0D photonic cavities [36][76][77], which would prevent second photon from entering the system at resonant injection [52], as the resonant frequency is shifted by more than a linewidth (it is usually believed that strong nonlinearity is required and that polaritons have inherited this from excitons). This was analytically shown to be possible by [76], because of the destructive quantum interference effect appearing between two coupled microcavities. This paper predicts that the optimal nonlinearity is $U_{opt} \simeq \frac{2}{3\sqrt{3}\frac{\gamma^3}{J^2}}$ (in which γ is the mode broadening and J is the intermode tunnel coupling energy).

Another way of achieving a polariton blockade is by using SAW waves. A condensate is a state of matter in which the lowest energy state is occupied by all atoms (Fig. 1.11). A simpler explanation is that the bottom of the present potential is occupied by the atoms. In case the frequency of the acoustic wave is sufficiently big, the potential becomes small enough that every single potential minimum could be occupied by only one atom. To achieve it, BEC particles have to overcome the phase transition between superfluidity and a Mott-insulator (the transition requires external potential-SAW). This can happen in a polariton system, because polaritons are bosonic particles, which have repulsive interactions between each other due to excitonic wavefunction. This transition depends on

the ratio between polariton-polariton interaction energy (U) and tunnel coupling energy (J).

The mentioned ratio is changed by altering the SAW amplitude [78][79]. Deeper potential leads to weaker tunnelling, and in the case of U being bigger than J, the system becomes a Mott insulator, because polaritons will not be able to tunnel to a neighbour wire. This will lead to wire occupation with an average of one polariton, and coherence is totally lost. This is a reason why to have a lot of shallow potentials requires a very high frequency. This SAW would move polaritons at the acoustic speed ($v_{saw} = 3 \cdot 10^3 m/s$, which was proved by a phase change rate using classical second order intensity autocorrelation measurement) to the boundary of the sample, where it would emit photons independently of each other. Because of the potential minimum containing single atom, only one photon would be emitted every time. This should be possible because of high nonlinearity and narrow polariton linewidth.

A similar experiment was published by [80], but the frequency was not high enough. The SAW method is very promising, because a slowly propagating wave does not heat excitons and allows manipulation of cold exciton gases [69]. Long-range exciton transportation has already been demonstrated [69]. It was also shown that transportation efficiency increases with gate voltage $< -6V$ applied perpendicular to the SAW plane [69]. SAW changes not only refractive index of the spacer level, but also its thickness [81].

To achieve a polariton blockade, polariton linewidths of $50\mu eV$ are required, which mostly depends on the sample quality. The expected polariton linewidth is found using the equation: $\gamma_{pol} = \frac{\gamma_{ex}+\gamma_{ph}}{2}$, but in reality, smaller linewidths are measured because of an effect called motional narrowing.

1.7 Open-Access Microcavity - A New Method for Strong Lateral Confinement of Polaritons

1.7.0.1 Open Microcavities

Open semiconductor microcavities operate on the same principles as simple semiconductor microcavities. The single difference is that in the open microcavity the light passes through free space, whereas in general microcavities it would pass a layer of semiconductor. Consequently, the gap between DBR mirrors can be changed freely, and full control of photonic modes is achieved. This difference also allows the use of dielectric mirrors, which have better reflectivity and less penetration by light. Because of the dielectric mirrors and high semiconductor relative permittivity, it had been demonstrated that over 80% of vacuum energy is concentrated in the semiconductor, around 10% in dielectric and 5% in the air gap [18]. In full microcavities, dielectric DBRs are not used because of lattice mismatch. A good example of open cavity usages are optical sensor fields and lasers [15].

Some of the possible opec-microcavity mirror forms are given in Fig. 1.16. Curved mirrors are fabricated using a focused ion beam ([19]), and DBR mirrors are grown on top. This feature allows the confinement of light not only in the z-dimension, but also in the other two spatial directions, which cannot be confined by the microcavity itself, and so the system becomes zero-dimensional. This makes the cavity modes discrete and splits them into longitudinal and transverse modes, because the difference between the k vectors is bigger than the polariton linewidth [14]. This new shape directs light into a smaller space and also allows very small mode volumes of λ^3 order, a change which creates a higher density of light power. The main challenge of open microcavities comes from the surface roughness of the created spherical mirrors; if not for this problem, the finesse would exceed the finesse of macroscopic cavities of over 1 million [82].

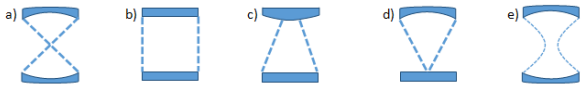

Figure 1.16: Open-cavity mirrors can have different forms. This figure shows couple examples of them. a) concentric (spherical) b) plane parallel c) concave-convex d) hemispherical e) confocal

Because of the circular shape of mirrors used to confine light (they are also less sensitive to alignment, compared to the planar-planar cavity), the modes are Gauss-Laguerre modes with axial symmetry. Curved mirrors have another advantage compared to plane mirrors, their finesse is bigger by almost 100 times [18]. A Q-factor of 35000 was achieved in a recent open-cavity system at $L = 9\mu m$ (cavity length) with $RoC = 19\mu m$ and $16\mu m$ (Radius of Curvature) [83]. Figure 1.17 shows that at first, the quality factor increases with greater cavity lengths, because the time photon spends in the microcavity becomes longer. However, the quality factor peaks when the light scattering of the surface becomes more important. This happens for two reasons. First, because increasing cavity length expands the area, the light covers the concave mirror, which in turn increases light scattering and losses. Second, the stability criterion for the photon mode $L < R_c$ (where R_c is curvature radius of the concave mirror) is approached, so the losses of the cavity mode become greater. The use of separate DBR mirrors in open microcavities allows changes in the separation between mirrors, and this makes it possible to tune the cavity mode to any desirable wavelength, whereas it was fixed for all previously mentioned cavities.

An open microcavity solves the most important disadvantage of full microcavities - it's tunability. This allows to perform more different experiments using the same device. An open microcavity allows the researcher to observe photon and exciton energy level anticrossing (to know if the sample is actually in the strong coupling regime), easily set the mode at the resonance of the emitter, investigate the sample at the same spot (the microcavity composition stays the same) or to investigate different detunings with only one cooldown of the system. Changing the cavity length also changes the polariton lifetime and relaxation kinetics, as depending on the detuning, the lower polariton branch deepness and steepness

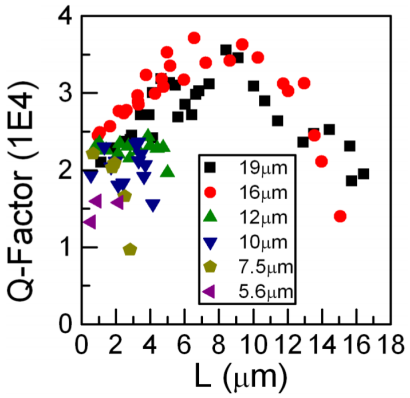

Figure 1.17: Polariton Q-factor dependence on cavity length for concave mirrors with different Radii of Curvature. The Q-factor increases at first, while it is mostly influenced by photonic lifetime, but starts to decrease when effect of the surface becomes stronger [83].

change. Increasing the cavity length causes the photon to spend more time in the cavity and the quality factor therefore increases (it shows the capability of confining light), but this comes with at the cost of reduced photon and exciton coupling, which is expressed: $g \propto \frac{1}{\sqrt{L+L_{DBR}}}$ (where g is coupling strength, L - cavity length, L_{DBR} - penetration into the mirrors).

An open cavity also allows the use of higher-frequency SAW waves, because IDTs can be placed directly on the bottom mirror. This requires smaller penetration, which depends on the SAW wavelength, to achieve desired effects. Hence, lower-wavelength SAW waves can be used. This method also reduces SAW's effect on the DBR mirrors and concentrates it in the active region for better results with smaller losses.

Quantification and detection of chemical species in microfluids is one of the most promising uses of the open-cavity device. [84]. Microfluids are fluids with a volume in the range of 10^{-9} to 10^{-18} litres. Such a device would be very useful in fields like biology, which involves a lot of very expensive reagents. Another advantage of the open-cavity system is efficient and quick work. 1cm path length cuvettes are dominating in the usual vis/UV spectroscopy devices, however in an open-cavity, 10 to 100 micrometres range would be possible. The multiple passes

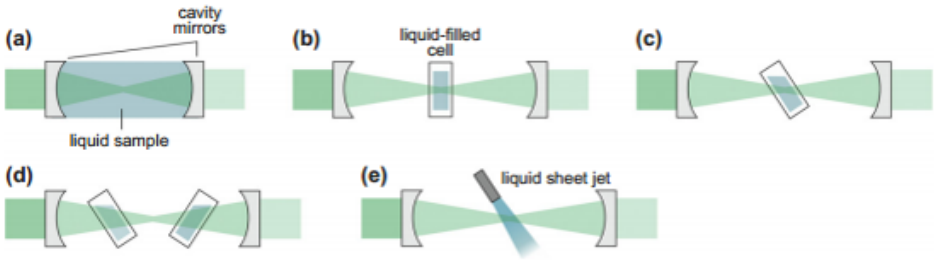

Figure 1.18: There are different ways to place liquid samples into an open cavity. Some possibilities are shown in this figure.

of the light through the sample (Fig. 1.18) is the secret behind the promising success of open cavities, which greatly enhances sensitivity to the concentration of the molecules in the sample, compared to single-pass methods, and boosts path length. This was already achieved in gasses (1988) and liquids (2002).

1.7.0.2 Laguerre-Gaussian Modes

The small radius of curvature mirrors on open cavity samples are made on a planar substrate using FIB milling [85]). The condition of $L_{phys} < RoC$ has to be met to get stable modes in the cavity [86]. These circular concave mirror features create a circular symmetric beam profile, which can be described the best with the Laguerre–Gaussian (LG) modal decomposition.

The Eq. 1.24 is used to describe Laguerre–Gaussian mode profiles. Eq. 1.24 is presented in the cylindrical coordinate basis with l - the azimuthal index (representing the beam's angular momentum with possible positive, zero or negative values) and p - the radial index (can be zero or positive). The LG transverse modes are degenerate, if they satisfy $|2l + p|$ equation. All the transverse modes have an orbital angular momentum, which has a phase rotation of $2\pi l$, if $l > 0$, giving phase vortices.

$$E_{lp}(r,\phi,z) = e^{il\phi}\left(\frac{r\sqrt{2}}{\omega(z)^2}\right)^{|l|} A\frac{\omega_0}{\omega(z)} L_p^{|l|}\left[\frac{2r^2}{\omega(z)^2}\right] e^{\frac{ikr^2}{2R(z)}} e^{\frac{-r^2}{\omega(z)^2}} e^{-tan^{-1}(\frac{z}{z_0})i(2p+l+1)} \tag{1.24}$$

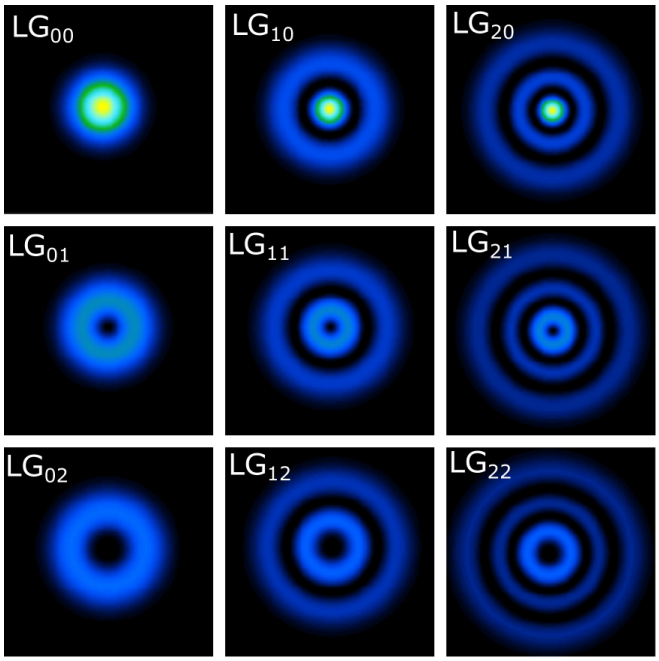

Figure 1.19: Beam profiles of 9 Laguerre–Gaussian modes labeled as LG_{pl}. This type modes were observed in open cavity system. Taken from [87].

Here L_p^l is the generalised Laguerre polynomial, A is a normalization constant, $\omega(z)$-beam width at distance z.

1.7.0.3 Coupled Cavities

Improved concave mirror fabrication methods lead to the possible creation of photonic molecules where microcavities couple to each other electromagnetically. It can be directly compared to organic molecules, as similar bonding-antibonding modes are created. For example, it is possible to fabricate two concave mirrors so close to each other (or mostly overlapping, with the centre-to-centre distance being smaller than the double radius of the mirrors and resembling the shape of a peanut) that they couple and modes hybridise into bonding-antibonding modes, the energy structure of which is similar to a diatomic molecule like H_2. Current technology already allows the manufacture of even more astonishing structures like concave-mirror lattices or zig-zag chains. It is planned to investigate such structures for new effects and physics in the future.

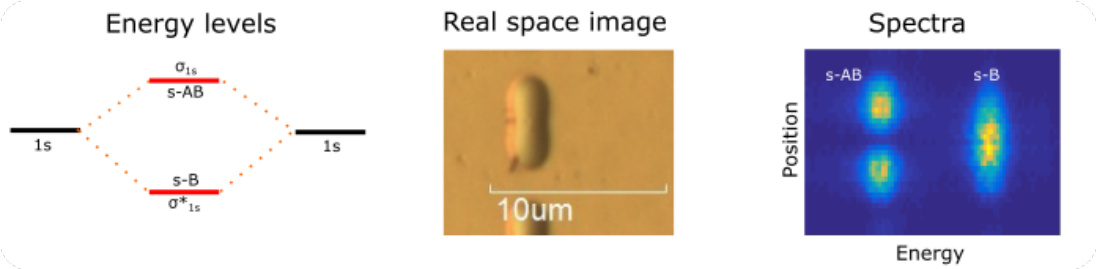

Figure 1.20: On the left, there is a schematic drawing of coupled mirrors' energy levels. The image of the used coupled concave mirror shows its peanut shape at the centre. The spectral image on the right shows the energy state of a coupled mirror longitudinal mode splitting into bonding and anti-bonding modes.

Just like in molecules, in coupled mirrors there cannot be two degenerate energy levels, so they split in energy. The lowest is the bonding state, and the highest is the anti-bonding state. Because of repulsive force, its potential increases, which is called mode hybridization (Fig. 1.20). In the figure, two lowest-energy bonding-antibonding modes are visible, but higher-mode splitting was also achieved. Splitting between them depends on the degree of coupling between micropillars or concave mirrors. Coupling in coupled mirrors depends on centre-to-centre distance; the smaller the distance, the bigger the coupling. Coupled mirrors, just like coupled excitons and photons, show anti-crossing. Without coupling, one mode would go from high energy to low energy, another mode would go from low energy to high energy and at one point, both modes would have the same energy.

A very similar experiment to the two joined concave mirrors was performed using two identical coupled pillar microcavities. In this case, coupling was shown through a splitting of the modes [88]. Some properties were noticed: the energy of the lowest energy state increased with a decreasing diameter of the isolated micropillar, and mode splitting increased with a decreasing distance between pillars. When pillars were coupled strongly (coupling depends on how much the pillars overlap), the anti-node appeared to be in the centre between the pillars; when the pillars were coupled weakly, two anti-node regions were visible in the centres of pillars. The problem is that to observe antibunching in such a system requires a fast, single-photon detector, because of the quantum interference effect,

which disappears with small changes in system parameters [76].

1.8 Motional Narrowing

Motional narrowing is an effect when a spectral line in a disordered system is decreased by some averaging process or in other words, mode linewidth being narrower than expected from calculations. A good example is a polariton linewith being narrower than the expected linewidth, which is expected by knowing photon and exciton linewidths (linewidths of particles composing polariton). It is more noticeable in 1D than in 2D samples [89]. This appears to be the case because of decreased mass (a polariton is lighter than an exciton), because classical motion becomes more quantum mechanical and because spatial averaging over the smaller disorder potential appears (caused by interface roughness, alloy fluctuations and other factors) [33].

The motional narrowing effect is stronger for LPB compared to UPB in the strong coupling regime. This happens, because UPB experiences a lot of scattering events between the two mentioned branches and it accounts for additional broadening. This explains the observation that the linewidth of the lower polariton branch is smaller than the upper polariton branch. Most of the polaritons relax from upper polariton into lower polariton, and so the upper polariton is dimmer. This effect is more pronounced in 2D than in 1D cases, because fluctuations are larger in an equivalent size of 2D sample [42]. The upper polariton linewidth is also wider because polaritons are scattered into higher k exciton states [42]. A simulation of an oscillator model predicts equal lower- and upper-branch linewidths for infinite exciton mass. With increasing mass, separation becomes visible [42]. In the first place, the lower polariton branch is wide because of inhomogeneous broadening, structural QW disorder, which appears because of In alloy-fluctuations or difference in QW thickness. This inhomogeneous broadening is around 10 times larger than homogeneous broadening (appearing because of exciton spontaneous recombination or dephasing) [31]. One of the ways to reduce linewidth is to reduce QW roughness. All the transverse modes couple to the QW exciton with the same strength, because of weak coupling strength dependence

on in-plane exciton momentum [90].

1.9 Sample Structure and Growth

It is important to discuss sample structure and growth. Couple different samples were used to get results used in this thesis, but only the growth and structure of SiN/SiO_2 top mirror with concave features and $Al_{0.1}GaAs/AlAs$ bottom mirror with a single $GaAs/Al_{0.1}GaAs$ quantum well (MQW) will be discussed as other samples were fabricated using same techniques with only couple things being different, for example the number of QWs, DBR materials, etc.

Despite better reflectivity using dielectric materials, bottom DBR is grown using semiconductors, to reduce the mismatch between lattice constants between QW and DBR, and so improving Q-factor of polaritons. The QW was designed to be located at the optical field antinode, the highest electric density. A design simulation example can be seen in Fig. 1.21. Materials of alternating DBR layers are also chosen to have the biggest difference in refractive indexes (giving best reflactivity) with the smallest difference in lattice constants (giving best sample quality).

Bottom sample is grown using a Molecular Beam Epitaxy (MBE) technique. The process starts by heating up very pure elements, which should be deposited in the layers, placed in separate cells. This material slowly evaporates and condenses on the sample heated to around $(500 - 600°C)$ creating ultra-thin layers by growing one atomic layer at a time. To increase purity of the grown sample, MBE requires high or ultra-high vacuum.

The top sample fabrication starts with a milling of a concave feature milling on a substrate, usually SiO_2, using a Focused Ion Beam (FIB) technique as this process allowed to achieve the highest Q-factors at the moment. Gallium ion (Ga^+) beam can be focused to as little as 7 nm diameter giving < 0.7 rms surface roughness of the concave mirror, milled by changing dwell time depending on the beam position. The next step is to coat the concave mirror template with

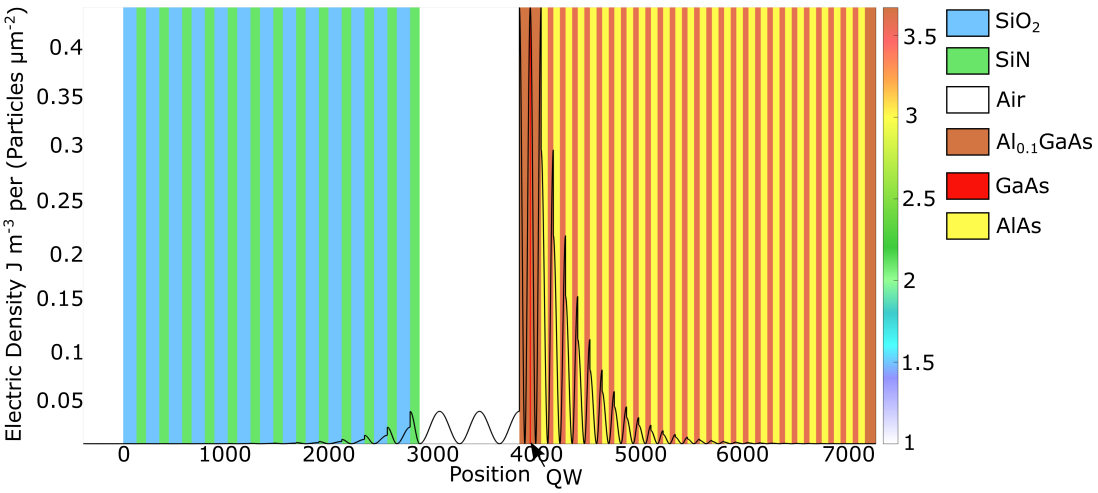

Figure 1.21: Electric density simulation for a 10nm GaAs QW in a 1λ cavity with 13 pairs of SiN/SiO_2 top mirror and 27 pairs of $Al_{0.1}GaAs/AlAs$ bottom mirror. The simulation was performed using MATLAB with an applied transfer matrix method. The QW is a red line at the electric field antinode. The colour of the microcavity structures corresponds to the refractive index and can be determined from the scale on the right. The black line corresponds to the electric field density at a particular part of the microcavity, and its value can be determined from the scale on the left.

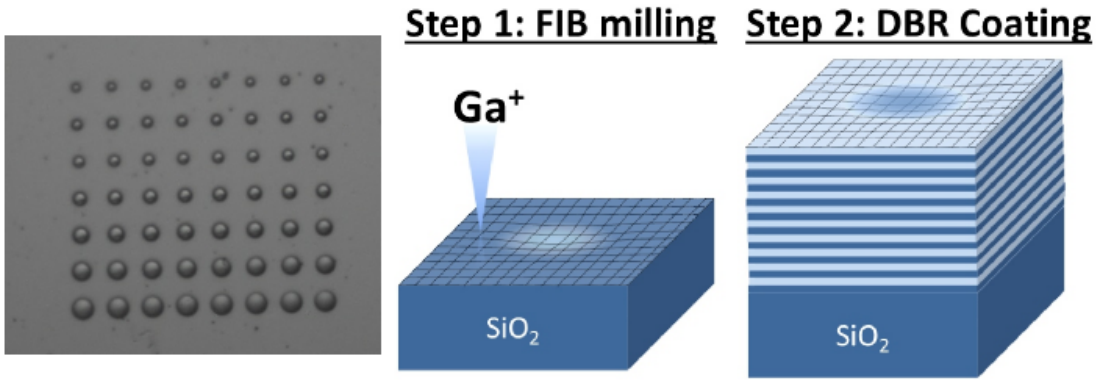

Figure 1.22: Investigated top mirror sample is on the left. Concave mirror radius varies from $RoC = 5.6\mu m$ (top row) to $20\mu m$ (bottom row). Schematics of concave mirror FIB milling on the top sample and the concave feature after it's coating with DBR. Figure taken from [91].

dielectric DBR, in this case 13 pairs of SiN/SiO_2 (Fig. 1.22). Multiple concave mirrors were milled on one sample, which varied from $5.6\mu m$ to $20\mu m$ diameter.

Chapter 2

Experimental Devices and Methods

2.1 Introduction

2.2 Open-Cavity Device

In this section, the original device will be presented. Over time, it was improved in many ways, which will be reflected in corresponding chapters. It contains two piezo stacks made by Attocube Ltd (Fig. 2.1), which allow precise control of the separation between the two DBR mirrors. The bottom sample is attached to 5 piezo stages: ANPx101/RES and ANPy101/RES are used to move the sample sideways to choose different excitation places, ANPz101/RES is used to control cavity length, and ANGp101/RES and ANGt101/RES are used to change angles between samples to make them as parallel as possible. These piezos are marked in the figure as X, Y, Z, P and T, respectively. The top sample is attached to 3 smaller piezo stacks: ANPz51/RES allows excitation light to be focused on the sample, and ANPx51/RES and ANPy51/RES allow a choice of which concave mirror structure on the top sample should be used. These piezos are marked in the figure as Z, Y and X respectively.

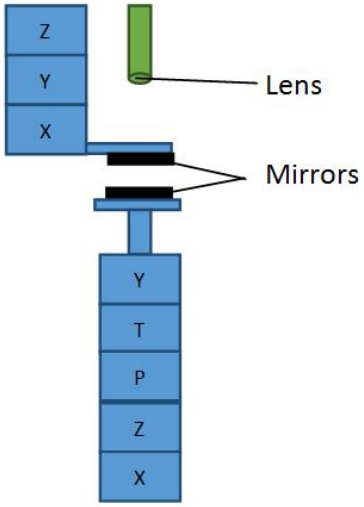

Figure 2.1: Sketch of the piezo stacks. The top stack contains three piezo stages, which can move in x, y and z directions. The bottom stack contains five piezo stages, which can move in x, y and z directions as well as tilt around the x and y axes (T and P piezo stacks respectively).

Figure 2.2: The piezo stages are attached to a supporting structure inside a 1.5-metre tube. This tube is lowered inside of a 100l helium dewar so that the temperature could be kept at 4K for a few weeks without refilling the liquid helium.

The whole open-cavity system is shown in the sketch (Fig. 2.3) and in pictures (Fig. 2.4). The system has three main parts: an optical table on the dewar (Fig. 2.4b), the dewar (Fig. 2.4a) and the optical table (Fig. 2.4c). The main 635nm laser is mounted on the optical table (Fig. 2.4 number 7) and is connected to the fibre launcher on the small optical table (Fig. 2.4 number 1) by a factory-made multimode fibre. The laser from the fibre launcher is directed to the centre of the small optical table (Fig. 2.4 number 3) using 1-inch mirrors. If needed, the laser is configured in this section (for example, changing the polarisation of an excitation). At Fig. 2.4 number 3, a 45° mirror directs the laser down through 50:50 beamsplitter cube into the 1.5m long tube (Fig. 2.2, which is placed inside of helium dewar Fig. 2.4a) and to the lens (Thorlabs NA=0.55 aspheric B-coated), which focuses the laser on the sample (Fig. 2.1). The beamsplitter cube can be placed into different transmittance, depending what is more important, higher excitation power or more efficient emission collection. Part of the laser coming out from the beam splitter is used to measure laser power.

The same NA=0.55 lens collects emitted light and sends it through the tube back to the beam splitter, where the light is directed to a fibre bundle (Fig. 2.4 number 4) using mirrors. Fibre bundle is a $4 \times 4mm$ array of single-mode fibres, each of which acts as a pixel and allows the transmission of the image. In case k-space is required (when performing angular resolved spectroscopy), four 1-inch lenses are added to keep the k-space image confocal (Fig. 2.3). Two of the lenses go to the tube and two on the optical table, marked by a dashed blue symbols. There is a Pellicle beamsplitter (transmission: 92%, reflectivity: 8%), which directs a small amount of collected light to a CCD camera (Fig. 2.4 number 2). This allows the sample image to be seen and the laser to be focused on the required concave mirror. If there is a need to modify the collected light (for example, to choose a particular polarisation), it is done in the section between the beamsplitter cube and the fibre bundle, because the fibre bundle destroys light properties and leaves only its image. There is also a 700nm-long pass filter just in front of the fibre bundle to stop reflected laser light when non-resonant excitation is used and the sample emission is above 700nm, as it was noticed that strong light causes a noise, which might influence measurements, in the fibre

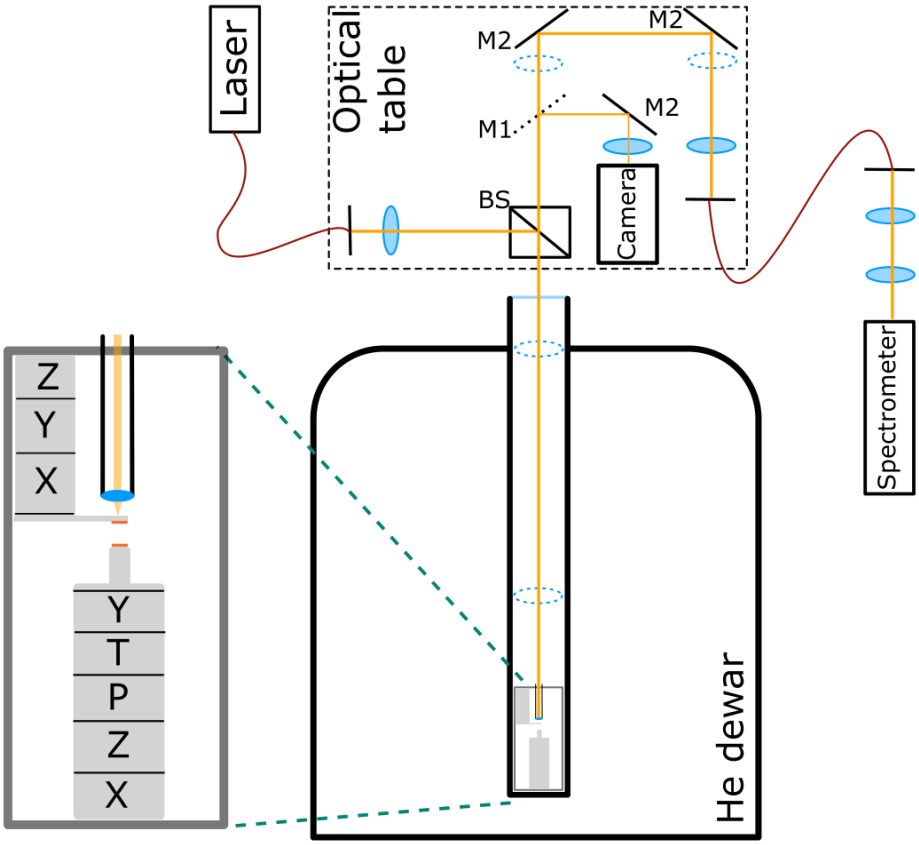

Figure 2.3: Sketch of an open-cavity device. BS represents the beam splitter, M1 - thin film beam splitter, M2 - golden mirrors.

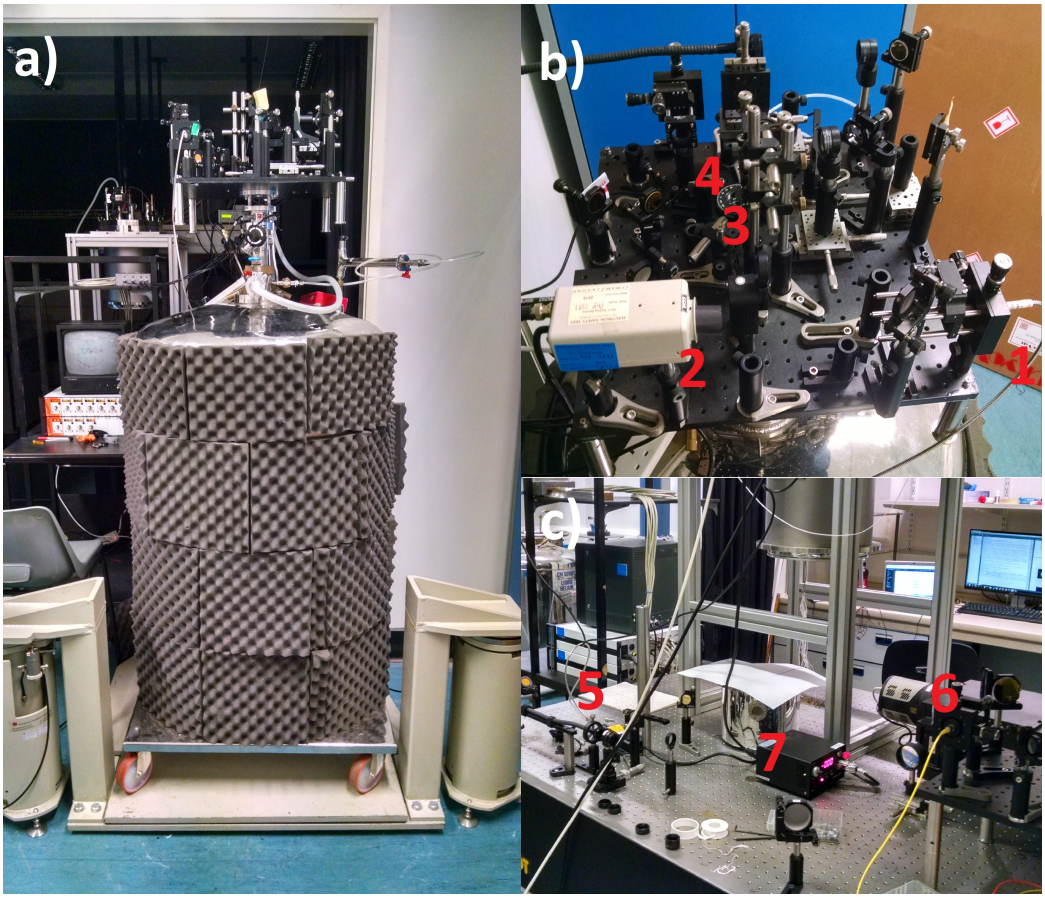

Figure 2.4: An open-microcavity system consisting of a helium dewar (a), a small optical table (b) and an optical table (c). The small optical table is used to direct the laser at the sample, which is inside the helium dewar, and the emission signal to the fibre bundle. Finally, the signal is analysed in the spectrometer on the optical table.

bundle at all wavelengths.

On the optical table (Fig. 2.4c), collected light is directed to the slit of the spectrometer. Here, the image size can be changed by changing lenses in front of the fibre bundle and spectrometer. An Acton SP2750 spectrometer was used with a spectral resolution of $50\mu eV$. Its focal length was $0.75m$, and there was a possibility of choosing between three gradings: 600 lines/mm, 1200 lines/mm and 1800 lines/mm. More lines disperse light more and closer peaks can be resolved, but these advantages come at the cost of reduced peak intensity. A Pixis 256 CCD camera is used in the spectrometer, which uses a deep thermoelectric cooling, which reduces dark current (noise in the spectra) without using liquid nitrogen cooling.

There are two ways to use spectrometer for imaging. First of all, it can be used for real space imaging. In this case spectrometer's vertical slit is fully opened, the light is directed straight to spectrometer's CCD camera and the image is recorded. The second way is required to image incoming light spectra. This time spectrometer's vertical slit is closed to be in the range of $20 - 100\mu m$ in order to select only a narrow slice of the image. Then the selected slice is directed to reach the grating which disperses light horizontally according to the energy it was composed from. The result finally reaches the spectrometer's CCD camera and the according spectra of the selected slice of the image is recorded.

There is also a negative side of using open microcavities. The most significant disadvantage is the stability problem, mirrors oscillate independently, because they are not connected to each other by a semiconductor layer. To reduce the stability issue, the original system was placed on the top of a specially built cradle system to cut off frequencies coming through the ground. Everything was covered with a sound-isolating foam box, which decreases vibrations coming through the air and reduces the influence of air flow. Incoming cables were also attached to a sturdy pole, which itself was attached to the optical table with the spectrometer on top, and left a bit loose, to damp the oscillations coming through the wires. One more way of stabilising the system was the attachment of a piece of steel

to the end of the tube (Fig. 2.2), which prevented the tube from swinging and reduced oscillations relative to the helium dewar. Some copper wool was added between the bottom piezo stack and the wall of the tube, to reduce the lateral movement of the bottom piezo stack. It is also not easy to bring open-microcavity DBRs very close together as deflection from the parallel alignment by a small angle causes the DBRs to contact somewhere, and even the smallest particles do not allow them to stay parallel. Not perfect positioning of the mirrors also reduces efficiency, because trapped waves move slightly to the sides of the DBR mirrors [17]. An open-cavity system can be seen in Fig. 2.1 and Fig. 2.2.

Cavity modes are standing waves in the cavity, formed from the travelling and reflected waves. To understand cavity modes, it is important to know the difference between cavity length L and effective cavity length L_{eff}. The cavity length is described as the distance between the mirrors, while the effective cavity length also accounts for penetration into the DBRs and the QW region ($L_{eff} = L + L_{DBR1} + L_{DBR2} + L_{QW}$. In case of a hemispherical-type open cavity, the effective cavity length must be smaller than the radius of the curve (RoC) of the mirror in order to get stable cavity modes: $L_{eff} < RoC$ ([87]). The reflectivity spectra of the cavity reveals that the cavity modes are equally spaced in frequency. This can be observed using a white light source Fig. 2.5. The dips in the reflectivity are attributed to different longitudinal and transverse modes, in case of $20\mu m$ cavity length. The decreasing cavity length increases the separation between the mode. This trend continues down to only one longitudinal cavity mode visible at $2\mu m$ cavity length. The cavity length equation (Eq. 2.1), which allows the estimation of effective cavity length by knowing the frequency difference ($\Delta\nu$) between two longitudinal modes, shows the mentioned trend. In summary the shorter cavity lengths lead to the bigger difference in frequency between peaks or the free spectral range. Longitudinal modes are followed by evenly spaced transverse modes, which appear because the mirrors are not perfectly parallel and the modes are drifting to sides.

$$L_{eff} = \frac{c}{2\Delta\nu} \tag{2.1}$$

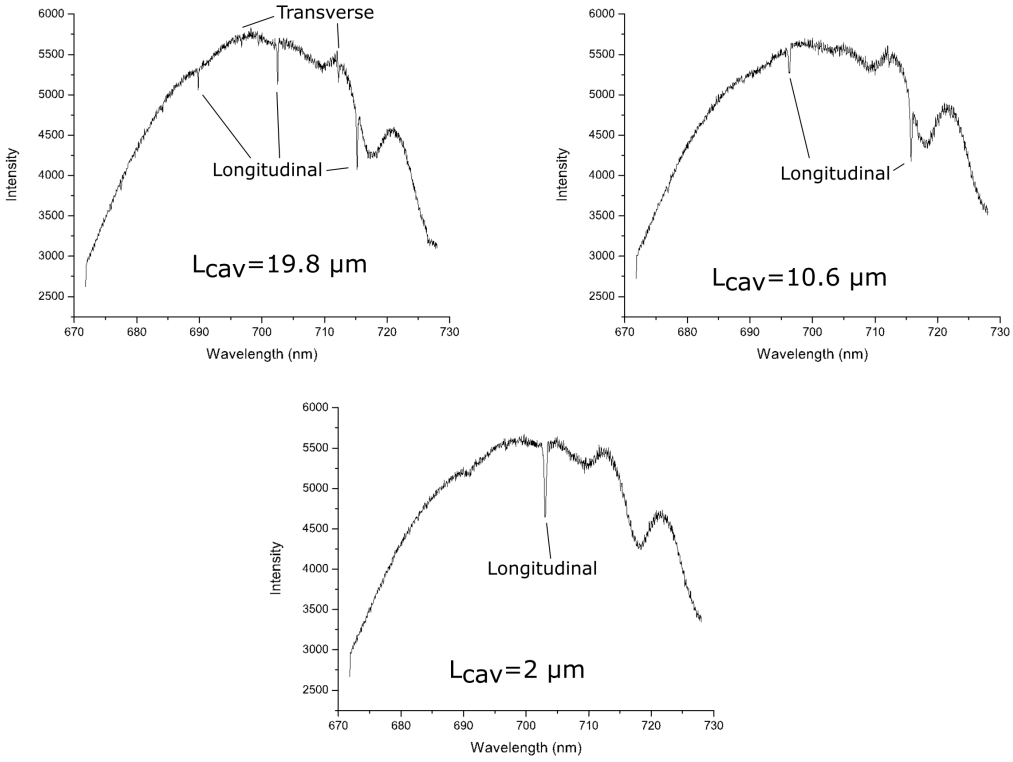

Figure 2.5: Intensity of the light reflected from the sample versus wavelength for different length cavities ($2\mu m$, $19.8\mu m$ and $10.6\mu m$) showing a changing number of cavity modes, which decreases with decreasing cavity length.

The beam waist size on the top mirror in an open cavity depends on the cavity length and the mirror radius as shown: $w_0 = (\frac{\lambda L}{\pi})^{1/2}(\frac{R}{L_{eff}} - 1)^{-1/4}$, where R is the top mirror curvature, L - mirror separation, L_{eff} - effective cavity length. The cavity volume can be found from: $V = \frac{\pi w_0^2 L_{eff}}{4}$. Volume in an open cavity is bigger than in a full cavity, because of the concave feature, but the higher Q is more important when studying quantum electrodynamic (QED) effects [16]. Mode area, when the radius of curvature is much bigger than the cavity length is much smaller ($L << R$), is $A = \frac{(LR)^{\frac{1}{2}}0}{2}$. The actual radius of curvature can be determined from the equation: $\Delta L = \frac{\lambda}{2\pi}\Delta(n+p)(\frac{L}{r_1})^{\frac{1}{2}}$, where n and p are Hermite mode indices [92].

2.3 White Light and Resonant Laser Reflectivity Technique

This section will describe the technique used to get concave mirror modes using white light reflectivity and a resonant laser in a reflectivity configuration. It is very difficult to get modes in resonant laser reflectivity immediately, because of the level of the alignment required. This is why an intermediate step of white light reflectivity was introduced as it is easier to get resonant laser modes after they were observed in white light reflectivity.

First, the system is aligned to get a nice longitudinal mode, which is placed just above the resonant laser wavelength, using a non-resonant laser. Then the non-resonant laser in the fibre coupler is replaced with white light coming from a single-mode fibre. Single-mode fibre was chosen to create a better match between the white light and the concave cavity mode. If the white light or the resonant laser is bigger or not the same shape as the cavity mode, then more light will be reflected and less will actually get into the cavity, which will make the reflectivity dip very small. The white light spot is placed on the concave mirror, and the lens in the fibre coupler is adjusted in all three dimensions to give the best mode dip. Then the end of the single-mode fibre, which is placed in the white light source, is taken to the fibre coupler, which couples the resonant laser to a single-mode fibre.

The same fibre is used, and its end in the fibre coupler on the optical table is not moved. This is done because different fibres focus on slightly different places on the sample, and the alignment would be lost.

The bottom sample is fine-tuned to get the resonant laser mode in reflectivity. This is done by increasing the voltage on the z-stage in very small steps and taking the spectra. Then the resonant laser peak is plotted against the voltage, where a sharp decrease in reflectivity intensity means a concave mirror mode. This mode was observed using both white light and resonant laser for $20\mu m, 12\mu m$ and $7\mu m$ diameter mirrors.

The experiment was repeated for coupled cavity modes. It was proved that it is possible to choose which mode to excite, either bonding or anti-bonding. This requires a small laser spot. To excite the bonding mode, the focused laser is placed in between two coupled concave mirrors to match the bonding mode position. All attempts to get the anti-bonding mode with a focused resonant laser failed, but it was achieved (Fig. 2.6b) by placing a very unfocussed circular ring-shaped excitation spot from the resonant laser on one of the coupled mirrors (Fig. 2.6a). The reflectivity was observed for different coupling strength coupled mirrors. During some experiments, the dip reached 20% deep, and for small mirrors, it was asymmetric for unknown reasons.

2.4 Cross-Polarisation of the Laser

A polariton blockade requires a resonant excitation of polaritons. This introduces difficulties using a reflectivity configuration of the open-cavity device, because most of the laser power is always reflected from the sample, and this signal overcomes the emission signal. Transmission setup would not have such a problem as the laser light is blocked by the sample and the emission is collected from another side. In reflectivity mode, spatial filtering could be used if the emission does not occur in the same place as the excitation, but this is not the case in the current sample. A non-resonant laser could be spectrally filtered using special long pass filters, as their wavelength is far lower than the emission

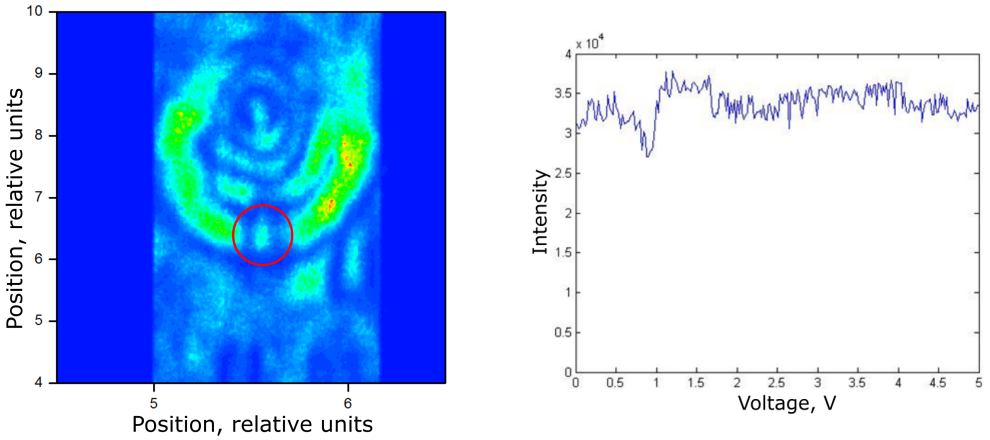

Figure 2.6: Left - real space image of sample's reflectivity signal in relative units with color representing it's intensity, right - intensity of the reflected light versus voltage/relative cavity length. A coupled concave mirror excitation using an unfocussed resonant laser in the left image (mirror circled with red). Another coupled mirror is just below the circle. A mode dip in reflectivity representing the anti-bonding mode (at around 1V) in the right image. The bonding mode is not seen.

wavelength. Unfortunately, a polariton blockade requires excitation using a resonant laser that is at the wavelength of the emission. One more option is to use the cross-polarisation technique. This technique is derived from the knowledge that reflected light retains its previous polarisation, whereas emitted light from QWs is unpolarised.

Experiments were performed using a single InGaAs QW on the bottom semiconductor DBR and 825nm stopband dielectric concave mirrors of various diameters on the top DBR. Two linear polarisers were also introduced in the system, one in the excitation light path and one in the collection light path. This ensures that the excitation laser is attenuated as much as possible in the collection path. Also, a $\lambda/4$ waveplate was introduced into the system as can be seen in the new system configuration shown in Fig. 2.7.

Firstly, cross-polarisation was tested on a flat semiconductor mirror. The cross-polarisation steps were as follows. First, the linear polariser was set at the angle that would give the most laser light. Then another linear polariser was placed

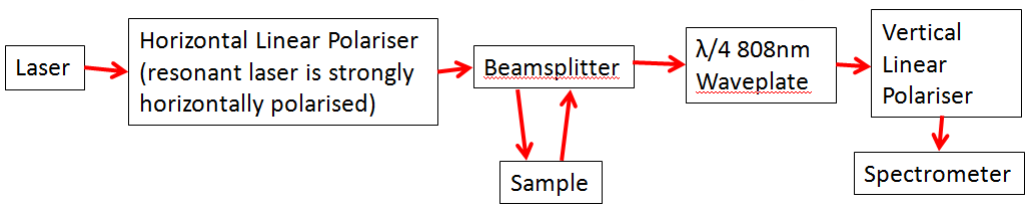

Figure 2.7: Scheme of the light path in a cross-polarisation setup. Two linear polarisers and a $\frac{\lambda}{4}$ waveplate were introduced on the optical table to reduce the resonant laser reflection.

after the beam splitter at the angle to pass the smallest amount of reflected light. A $\frac{\lambda}{4}$ waveplate was used to fix a slight ellipticity of the light, appearing after it passes several lenses and a beam splitter, and convert it to a linearly polarised form, so that the laser could be successfully blocked. The waveplate is again turned to pass the lowest amount of light. The last step is to further optimise the second linear polariser and the $\frac{\lambda}{4}$ waveplate to get the lowest amount of light possible.

This method allows an extinction ratio of $6 \cdot 10^{-5}$; in other words, it reduces the laser power by almost 17000 times. This number is identified by comparing the total signal strength before and after attenuation as can be seen in images (Fig. 2.8). It can be seen that cross-polarisation does not block the whole laser spot. This happens because scattering slightly changes polarisation; thus, not everything is blocked by the second polariser, and the pattern of weaker and stronger laser reflections is formed. This pattern is not constant and changes with the $\frac{\lambda}{4}$ waveplate's rotation. Later measurements showed that such an extinction ratio was not enough to reduce the laser reflectivity.

The cross-polarisation extinction ratio can be further improved by spatially selecting only a dark area marked by a red circle (Fig. 2.8). This spatial selection is done horizontally, by closing the slit on the spectrometer, and vertically, by choosing an appropriate region of interest on the spectra using WinSpec software. This significantly improves the extinction ratio, but it is harder to quantify the final result as an increase in laser power was required to observe the signal. It is important to note that this method reduces reflected laser power in the area

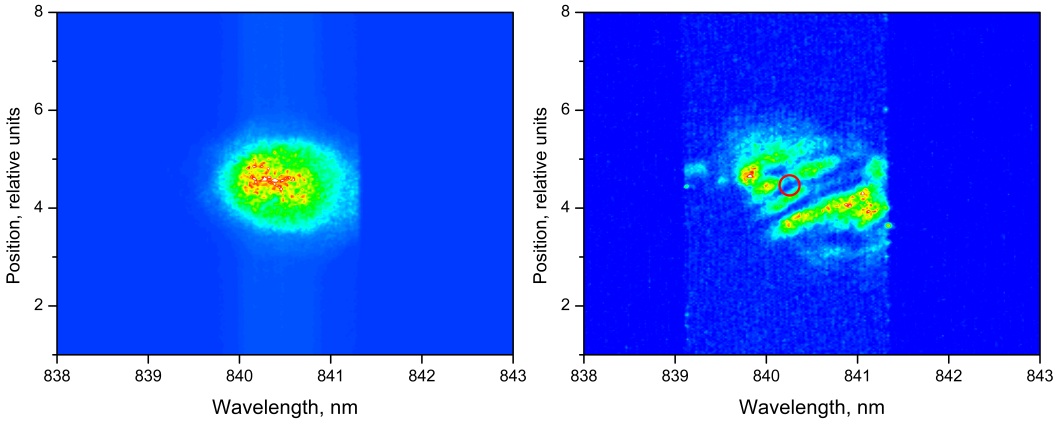

Figure 2.8: A laser spot before cross-polarisation (on the left) and the laser spot after cross-polarisation (on the right). A visible pattern appears because of slightly changed polarization during reflection. The red circle marks the area measured using spatial filtering.

covered by only a few pixels.

Next, cross-polarisation was tested on a 16μm-diameter concave mirror. First, a non-resonant laser was used to adjust the longitudinal mode to slightly higher than the wavelength of a resonant laser, 840.2nm (Fig. 2.9). Second, the linear polariser was already present in the system. Then the excitation focus and the excitation position on the mirror were optimised using the technique described previously in the thesis to get the best longitudinal mode signal. This was followed by a white light reflectivity (Fig. 2.10) and a resonant laser voltage scan to make sure that the mode was still there and that it was observable in reflectivity mode. In this case, a small dip is visible where the mode is. The next step is to mark where the laser spot centre is (Fig. 2.11 Left), introduce a second linear polariser and $\frac{\lambda}{4}$ waveplate and reduce intensity to the minimum by rotating them. This will give a pattern instead of a nice spot (Fig. 2.11 Right). The following step is to spatially choose a few dark pixels where the laser spot was (by closing the slit and choosing an appropriate region of interest in the spectra). Further optimisation is required to reduce intensity counts as much as possible by rotating the second linear polariser and $\frac{\lambda}{4}$ waveplate. After optimisation, the system is ready for a cross-polarised laser voltage scan.

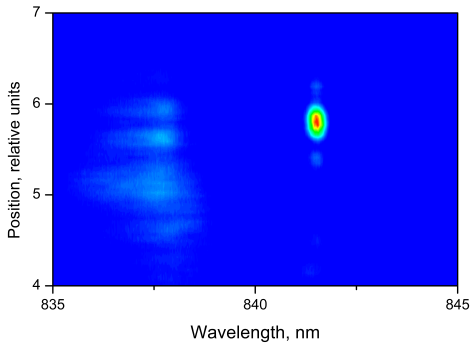

Figure 2.9: Longitudinal mode placed just above the wavelength of a resonant laser (840.2nm), using a non-resonant laser.

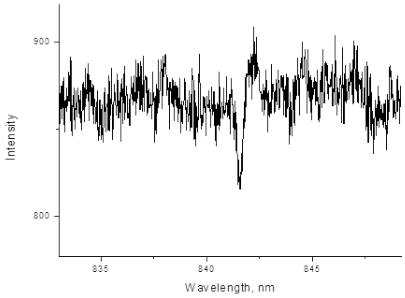

Figure 2.10: Longitudinal mode placed just above the wavelength of a resonant laser (840.2nm) and observed using a white light source.

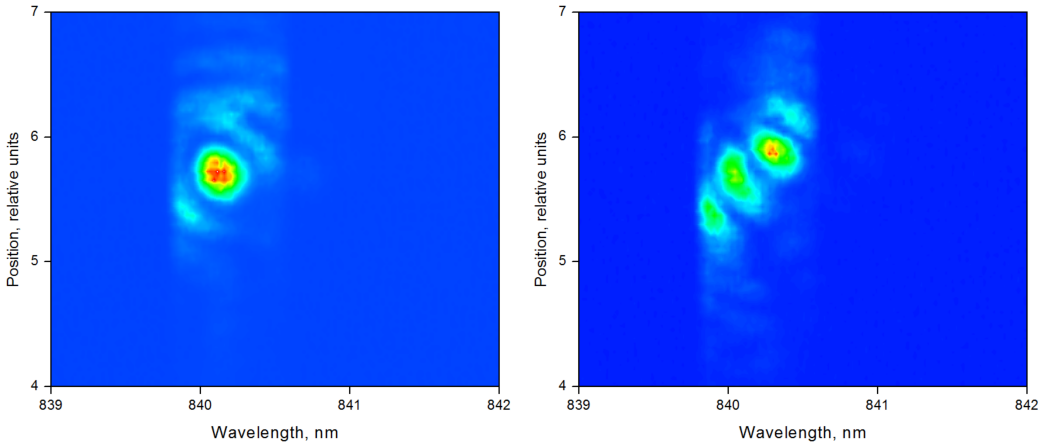

Figure 2.11: The signal of a resonant laser on a concave mirror before (left) and after (right) cross-polarisation. It will be further optimised to reduce the intensity in the position of the marker. Then a few pixels in this spot will be spatially filtered.

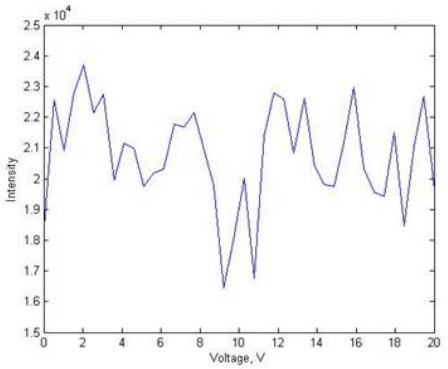

Figure 2.12: Reflected signal intensity versus voltage/relative cavity length. Longitudinal mode in a reflectivity scan using a resonant laser before cross-polarisation. The observed split mode is weak.

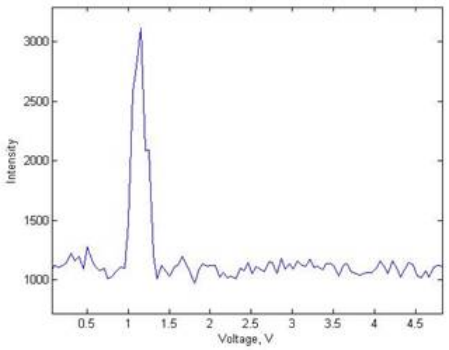

Figure 2.13: Sample emission intensity versus voltage/relative cavity length. A reflectivity spectra scan observing the emission of longitudinal mode, after cross-polarisation using a resonant laser, 3 times over background signal.

Using a $16\mu m$-diameter concave mirror, the occurring mode peak is very clear and overwhelms the background of reflected laser light by 3 times (Fig. 2.13). The peak is observed because the light emitted from the cavity is stronger than the laser reflected from the sample. The same cross-polarisation and optimisation steps were repeated to find the longitudinal mode signal using $6\mu m$ and $6\mu m$ coupled concave mirrors. Surprisingly, a $6\mu m$ concave mirror shows an even stronger longitudinal mode, and the coupled cavity signal is around 30 times stronger than the background (Fig. 2.14). This allows not only the bonding and anti-bonding modes to become visible, but also the first transverse mode, which is much weaker. The explanation could be that smaller concave mirrors have a higher power density.

This is required to achieve a polariton blockade in coupled concave microcavities as the laser can be suppressed enough to see the emission. More importantly, the signal is very intense, using a coupled concave cavity, and even stronger compared to a single concave cavity. Both the longitudinal and first transverse modes can be observed.

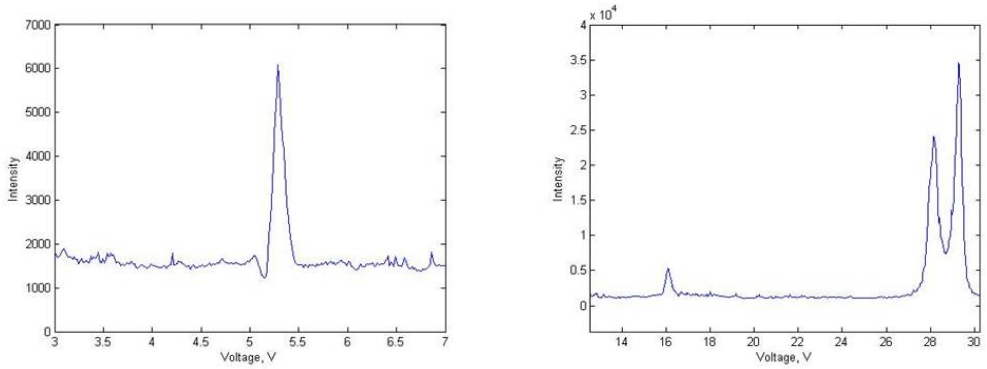

Figure 2.14: Sample emission intensity versus voltage/relative cavity length. Longitudinal mode, in a cross-polarised laser scan, using a $6\mu m$ concave mirror (left) and a $6\mu m$ coupled concave mirror (right). Coupled concave mirrors provide a stronger signal than a single concave mirror. A trace of a transverse mode is observed using a coupled mirror.

In conclusion, a good laser extinction ratio is observed when combining laser cross-polarisation with a spatial filtering. This allows the viewing of the longitudinal mode 3 times stronger than the background in concave mirrors and almost 30 times stronger using coupled concave mirrors. The resonant excitation is very efficient as a 103nW power resonant laser was used during cross-polarisation measurements, but it was still strong enough to give signal strength counts of tens of thousands. The current setup is ready to be used for G2 measurements in order to observe possible antibunching arising using a coupled concave cavity as described in [76].

2.5 Improved Design

The open-cavity design was improved to allow the collection of light to be transmitted through the sample. Samples were moved from a horizontal to a vertical position as can be seen in Fig. 2.15. This creates enough space to introduce 2 mirrors, which direct light to and from the sample. Two 15mm focal length and 5mm-diameter lenses were placed just above mirrors to concentrate light onto the sample. The top sample was made to be stationary to reduce the number of piezos required to form a cavity, in order to increase the sys-

tem stability. The bottom sample was placed on 5 Attocube Ltd closed loop nanopositioners: the x and y directions were controlled by ANPx101/RES, the z direction by ANPz101/RES, tilt by a goniometer stage ANGp101/RES and a rotational stage ANR101/RES. Three piezos were used to allow excitation light to be focused on a chosen concave mirror. These stages include ANPx51/RES for xy-direction control and ANPz51/RES for the z direction. A collection lens was also attached to an ANPz51/RES piezo for a z-direction control, allowing focusing. Because of the resistive readout used in these piezo stages, the readout accuracy is $\pm 200\mu m$. Ranges of movement vary 3mm and 5mm for ANP51 and ANP101 respectively, and 360° and 6.6° for ANR101 and ANGt nanopositioners respectively. Fine-tuning of the piezo stages (sub-nm range) is achieved by applying a 0-70V DC voltage. Housing was again made from titanium in order to abolish mechanical vibrations. Figure 2.15 shows a sketch of the setup, and figure 2.16 shows images of the already working system.

It was noticed that the new configuration is less stable, because the swinging of piezo stacks corresponds to a greater displacement (around 2nm) of cavity length, compared to the previous setup, in which samples were horizontal. One attempt to reduce swinging involved by placing copper wool between the housing and the piezo stacks, but the lower piezo pushing power or the increased rigidity of copper wool at a temperature of 4K required another solution. In another attempt, copper wool was placed on the sample holder, which would make the piezo stack and the housing touch, and so would not allow the stack to swing. This showed a small improvement, so another method of simply touching two samples was used for most of the measurements. It limits the cavity length, which can be reached, but the cavity mode is still freely tuneable. The current Q-factor was measured in this configuration.

The advantage of the current design is an easy switch between reflectivity and transmission configurations. This happens because reflectivity and transmission signals travel in parallel and very close to one another. This allows both signals to pass all the optics (mostly 1-inch lenses and mirrors), and a slight move of the mirror in front of the fibre bundle switches between reflectivity and transmission

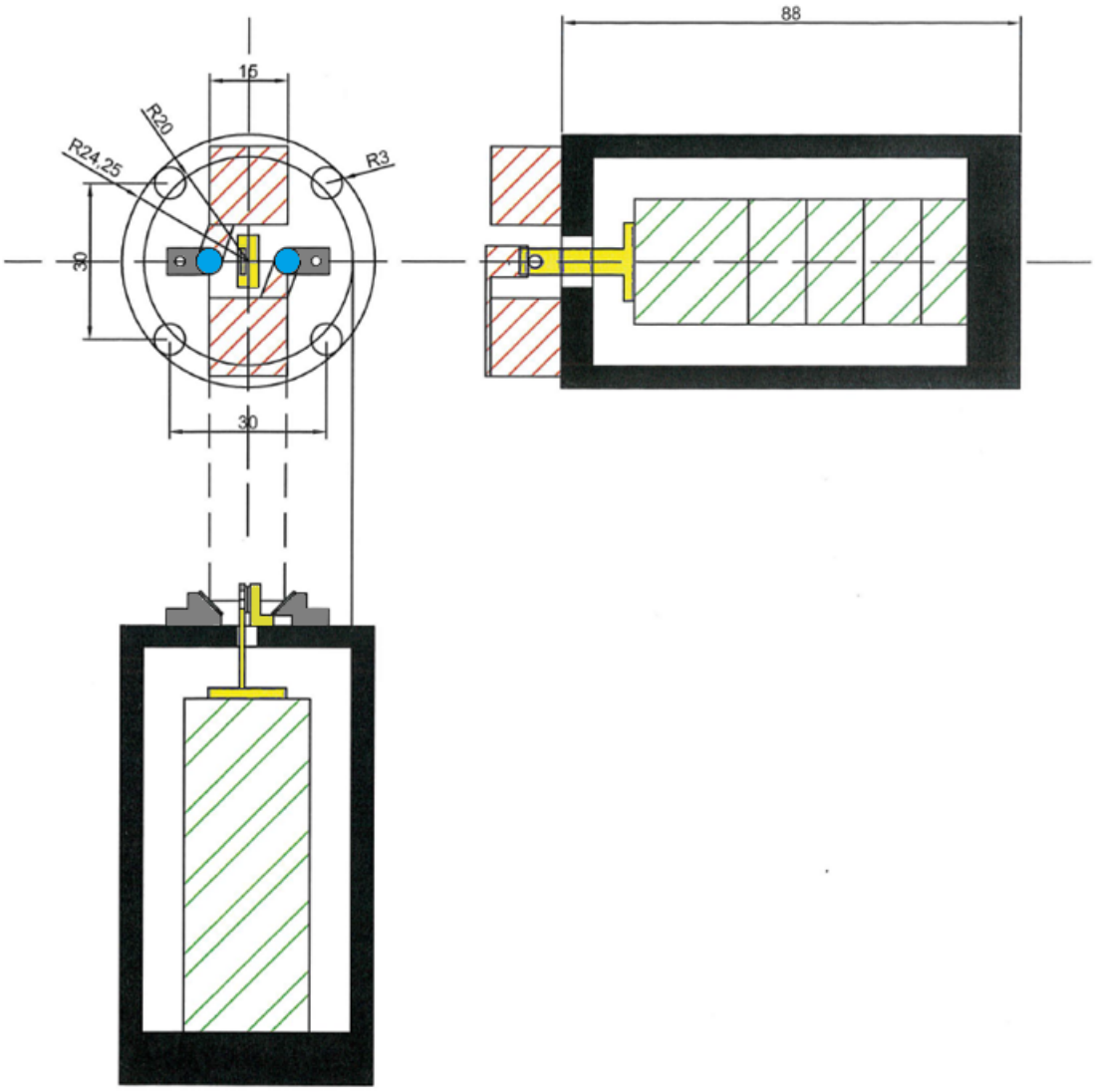

Figure 2.15: Sketch of the transmission setup cross-section in three directions. Black colouring shows titanium housing, green is the bottom piezo stack, red - lens piezos, yellow - sample holders, grey - mirrors, blue - lenses.

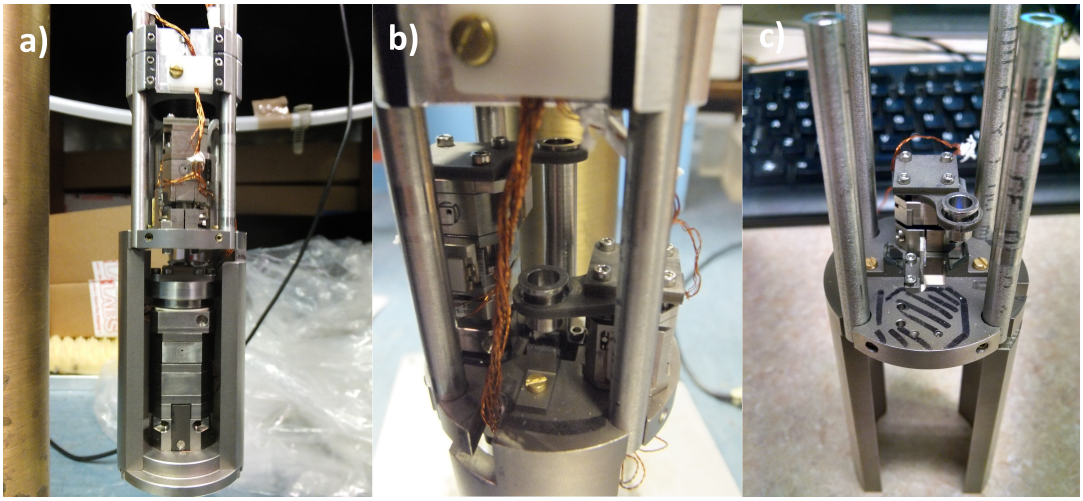

Figure 2.16: Images of an open-cavity insert inside a bath cryostat. a) Full image showing two nanopositioner stacks. b) Sample area with two piezo stacks controlling excitation and collection lenses placed in tubes. c) Sample area with mirrors, the top sample and a piezo stack (another piezo stack and the bottom sample are removed).

signals.

2.6 New Transmission Cryostat Design

A new transmission bath cryostat design was proposed to reduce the complexity of the alignment in the current open-cavity setup and to improve experimental capabilities. The sample area will be less compact and with easier optical access. More space in the sample area allows using more piezo stages, which are required for transmission setup. The new cryostat will also allow the spectrometer and the sample to be on the same optical table as well as ease alignment of the system. The sketch is presented in Fig. 2.17.

The new bath cryostat consists of 4 main volumes. The first is the largest and encloses the other 3 volumes. It is pumped out to reach high vacuum to reduce heating from outside. Another volume is an 8-litre liquid Nitrogen vessel that shields the helium volume from outside effects and reduces its consumption. It was designed to be filled with liquid nitrogen every day. The third vessel

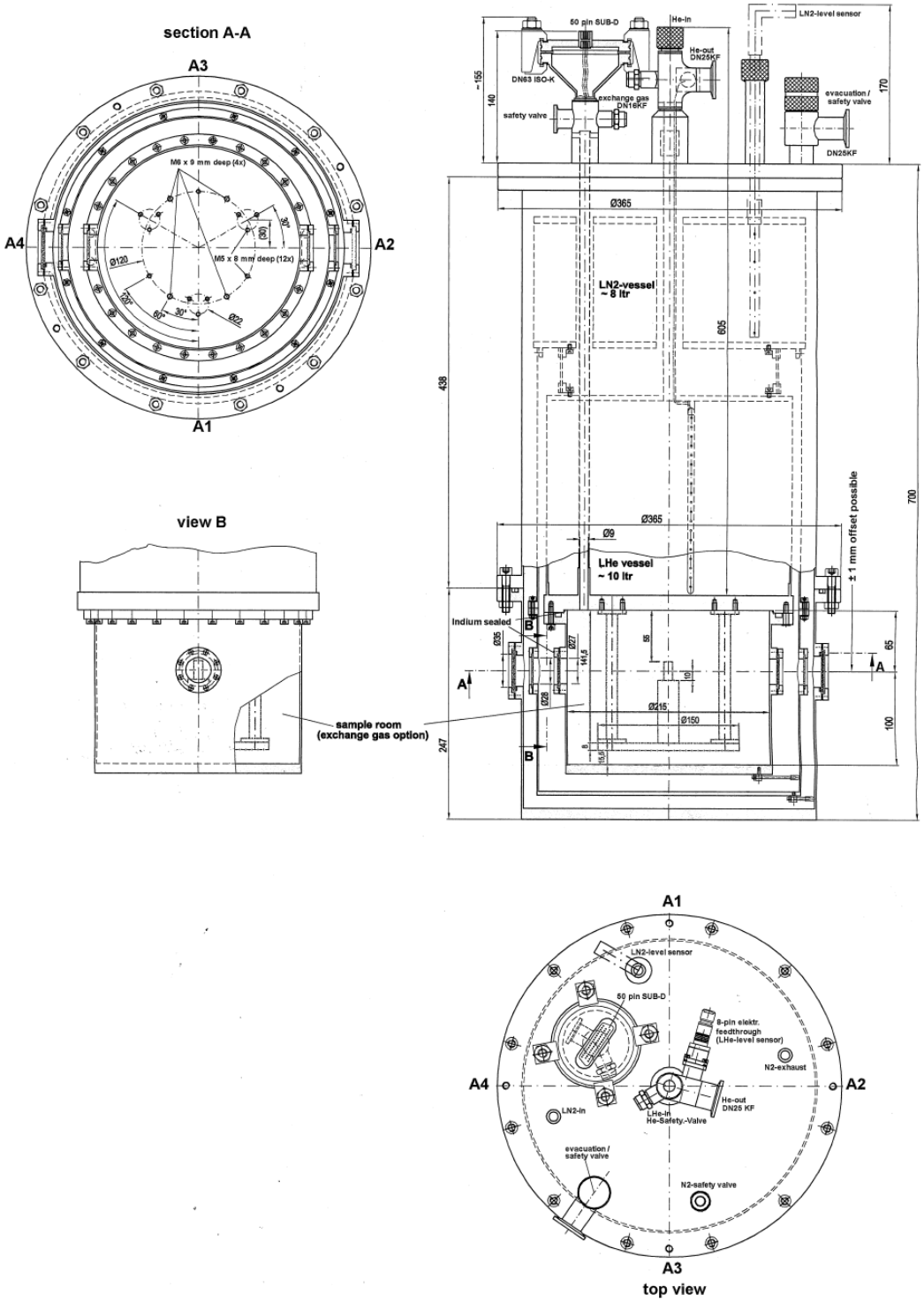

Figure 2.17: Sketch of transmission cryostat cross-sections in the vertical axis and the horizontal axis crossing the sample volume. It also shows the valve configuration on the top of the cryostat. The cryostat consists of 4 volumes: the LN2 vessel, the LHe vessel, the sample room and the outer jacket.

is a 10-litre volume for liquid helium. This part is designed to be filled every two days and put between liquid nitrogen and sample volumes. The volume consumption depends on the heat load of experiments. A 1W additional heat load will increase helium consumption to as much as 1.4l/h. In thermal equilibrium, this boil-off rate should decrease to 0.15 l/h. The last is the sample volume, which is connected to the helium volume by a brass plate. This plate allows heat conduction and keeps the sample volume at a temperature of 4K. Its large size allows the placement of three piezo stacks attached to the sample plate, which in turn are attached to the brass plate by three sturdy, not heat-conducting, rods. Because the sample vessel is pumped to vacuum and only a very small amount of helium gas is let inside of the system to allow heat transfer, the sample plate is connected by three flexible metal connections to improve heat exchange. The sample volume also has two 1-inch diameter windows on opposite sides for easy light access to the sample.

There are 50 thin wires inside of the cryostat connected to a 50-pin SUB-D connector on top of the cryostat. This allows the piezo stages to be connected to a control box. Ten piezo stages can be properly connected as every piezo stage requires 5 pins. However, in case the heater and the thermometer will be placed inside of the sample volume and additional stages will be needed, some piezo stages will be connected only with 2 pins. This is possible because every piezo stage has 2 pins for control and 3 pins for the readout. Some readout pins can be abandoned as, for example, it is not necessary to know the position of piezos controlling lenses.

All the piezos from the old setup are used in this system along with additional new piezos. There are two 7.5mm focal length and NA=0.32 lenses attached to the x, y and z piezo stages. Currently, one of the samples is fixed (it can be either the top or bottom sample), but it is planned to upgrade the system by placing 2 piezo stages in order to control the sample in the z and y directions. The last piezo stack consists of 5 piezos, of which two control sample angle (one rotational, ANR101, which can rotate 360°, and one tilt piezo) and the other three control the stack's position in x, y and z directions.

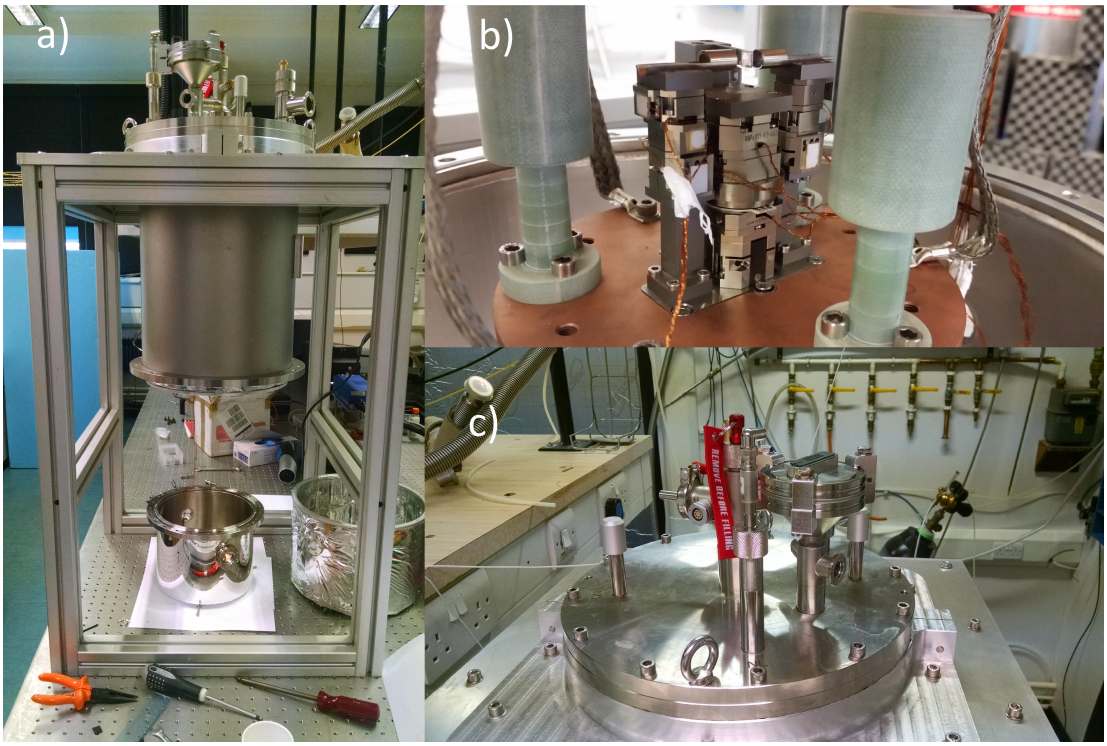

Figure 2.18: Figure showing a transmission cryostat. a) Full transmission system with all covers removed, but in place on the optical table. Two cryostat caps are visible. b) All piezo stages mounted on the sample structure in the cryostat's sample volume. c) Access valves to all 4 cryostat volumes and a 50-pin connector on top of the cryostat.

2.7 Transmission Setup Operations

All valves for accessing the four mentioned volumes are placed on the top of the cryostat (Fig. 2.18c). The system warm up, sample change and cooling down procedures are as follows. To warm up, the nitrogen and helium volumes should first be emptied. They can evaporate at a normal pace, but to make sample change faster, a thin, long funnel is inserted, which speeds up the evaporation process. After this evaporation, the system is left to warm up by itself, as there is no heater inside of the sample volume at the moment (though one is being designed). There is also no thermometer showing the temperature inside, and thus, the fairly accurate piezo capacitance is used instead. The piezo capacitance at room temperature is around $1.3\mu F$, and at 4K, it becomes $0.2\mu F$.

After warm up, the bottom part of the cryostat is unscrewed and removed. This gives the user access to the screws attaching the radiation shielding layer, which is also removed. The last step is to remove the sample room cap. As it is connected straight to the helium volume's brass plate, an indium seal is used, but due to the design, a flexible metal seal can be used as well. A common rubber seal cannot be used because of the low temperature, at which it would freeze and start leaking. In our case, the indium seal becomes too badly damaged for a second use, and so it is removed from the brass plate and the groove.

To make sample changes easier, all the piezos are placed on a small single plate, which screws into the main plate (Fig. 2.18b). It is removed when there is a need to change the sample. After the sample is changed, the small plate with piezos is screwed back as well as all three cryostat caps, with the new indium seal applied to the sample room cap.

The cooling procedure starts with vacuum pumping of the outer cryostat layer. The better the vacuum that is achieved, the longer the helium will last. The sample chamber is also pumped to vacuum, but a small amount of helium is let in to act as a heat exchange gas. Then both nitrogen and helium volumes are filled with liquid nitrogen by simple buckets and a long funnel. The helium tank is filled with liquid nitrogen for pre-cooling and then is blown out after the system settles down. Then it is filled with liquid helium using a specially made transfer line. The system is able to reach a temperature of 4K. Finally, liquid helium and nitrogen are topped up to full after the system settles down, and the helium chamber is connected to the helium recovery line.

All the optics, except the two lenses on piezo stages, are mounted on the optical table and aligned before cooling down. The cryostat window is above the usual optics level, because enough space had to be left to remove the shieldings, and so periscopes are used to lift the laser beam to the required height. Finally, after cooling down, the bottom sample is moved to form the cavity. First, the cavity is excited with a continuous, non-resonant red laser at 635nm. This helps to bring mirrors close together, by moving the piezo stage attached to the bottom mirror,

because laser interference fringes become visible at small cavity lengths and they stop moving when samples touch.

Chapter 3

Optical Properties of Polaritons in Open-Access Microcavities in the Low Density Regime

3.1 Introduction

Polariton states are characterised by Rabi splitting (dependent of the strength of exciton-photon coupling), exciton-photon detuning, the effective mass of photonic mode, etc. Formation of various nonlinear polariton phenomena (condensation and solitons) depends on these properties. There is a lot of theory describing change of these linear properties of the polaritons. So far most of the research has been focused on the study of polaritons in solid microcavities with fixed cavity length and hence fixed value of Rabi splitting and effective photon mass ([47], [17], [93]). Mostly this accounts to being possible to tune full microcavities over only a very small ranges. Another reason is that different cavities have to be grown to investigate effects over big cavity length ranges. This introduces unavoidable differences in grown sample structure and composition. Open cavity allows avoiding these problems, can produce results directly comparable between different cavity lengths and give results to prove or disprove current theories. The aim of this chapter is to investigate in details how the polariton Rabi-splitting, polariton dispersion, coupling in coupled microcavities, etc. changes with increase

of the separation between the mirrors from several hundred nanometers to 10's of micrometers. Coupled cavities' effects are interesting because they can be used for fabrication of lattices and study of lattice polariton phenomena in the regime of condensation.

3.2 Rabi vs. Cavity Order

Rabi splitting is very important, as its size determines the curvature of the lower and upper polariton branch dispersions, and it determines the exciton/photon fractions in the polariton wavefunction at a given energy separation from the bare exciton level. This influences the polariton relaxation processes and hence the threshold for polariton lasing and condensation. At room temperature, the value of Rabi splitting for stable, strong exciton-photon coupling should be bigger than the polariton linewidth (of the order of 10-25 meV) determined by polariton-phonon interactions. This is the reason that much work has focused on ZnO (58meV [94]), GaN (31meV [95]) and organic semiconductors, which have the Rabi splitting larger than broad polariton linewidths at 300K (due to interactions with phonons) enabling the room temperature polariton lasing. Other materials like AlGaAs and InGaAs, used in an open-cavity system, require a low temperature of 4K: because of low Rabi splitting and the small exciton binding energy ($\tilde{1}$0meV), the excitons get ionised at high temperatures.

A few methods exist to try to increase Rabi splitting, such as using a higher number of QWs ([24]). On another hand, this method increases absorption; it is harder to put all QWs on the cavity field antinodes, and the thickness of the cavity is usually increased, which decreases Rabi splitting. The higher absorption makes it harder to observe the upper polariton branch (UPB) and precisely determine the Rabi energy value. The following experiment was performed to investigate more about how the Rabi energy and the effective mass of the photon cavity mode changes with cavity length. It is already known that the Rabi energy should decrease with increasing cavity length, because the percentage of the electric field density overlapping with QWs reduces as the cavity length increases ([96]). There have been no experiments performed to investigate the Rabi change in such

an extensive cavity-length range of over 20μm using exactly the same structure microcavity. This is mostly because of the small tunability of full microcavities.

The order of the cavity mode was determined by counting the number of longitudinal modes passing the exciton energy when the cavity length was increased from touching mirrors up to the desired cavity length. Going from cavity mode order m to m+1 corresponds to the change of the cavity length by $\frac{\lambda}{2}$ or $385.75nm$ (for $771.5nm$ exciton emission). The effective cavity length in resonance with the exciton can be written as $L_{eff} = (l+4)\lambda_X/2 + L_{DBR}$, where λ_X is the exciton wavelength and L_{DBR} is the penetration length of the optical field into the DBRs. Here the integer l is defined as the cavity mode order of the cavity.

Previous experiments showed that the upper polariton branch has not been observed in samples with 12 QWs due to their high absorption and efficient relaxation ([87]). Therefore, Rabi splitting had to be estimated using curve fits. With increasing cavity length, absorption decreases, and at the 60th cavity order, UPB becomes clearly visible (Fig. 3.1).

An anticrossing scan of the LPB energy at k=0 vs. the cavity length proves that system is still in the strong coupling regime (Fig. 3.2). With decreasing cavity length, the UPB became more and more obscure, and longer exposure was used. At the touching point, it would be impossible to determine UPB just by looking at the spectra, but it is clear afterwards by following its change from the long cavity length.

The Rabi change vs. the longitudinal cavity mode order was determined by moving the top mirror, so that the energy of cavity mode moves through the exciton energy. As a result of strong exciton-photon coupling, anticrossing between the lower and upper polariton branches has been observed, which determines the Rabi splitting size. The experimental effective cavity length range was from 2λ to 32λ, with corresponding longitudinal orders labelled from 0 to 60. The cavity length at the touching point was deduced by knowing that the used active region of the cavity was designed and grown to be 2λ in the case of the parallel mirror

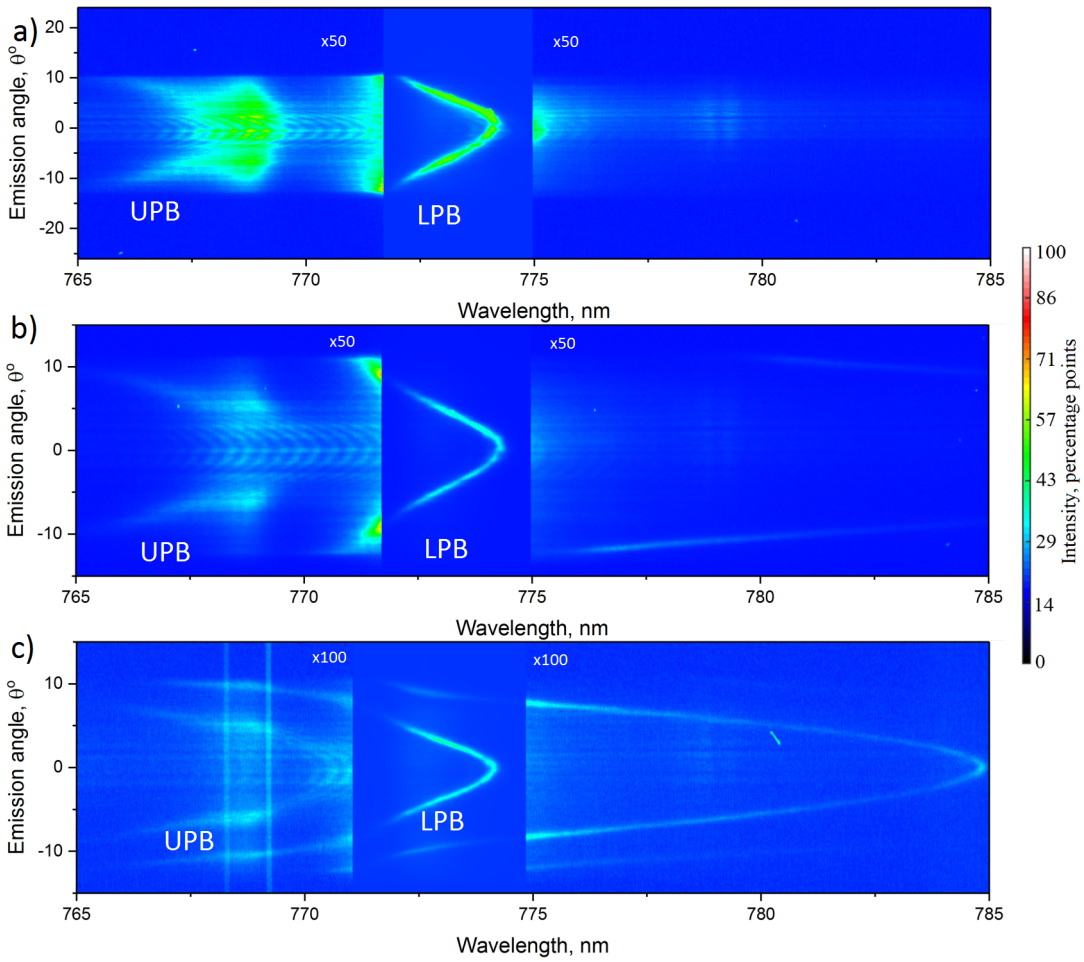

Figure 3.1: Figures of polariton emission wavelength vs. emission angle with color representing emission intensity using 12 QWs, which show polariton dispersions at three different cavity lengths. a) Cavity modes at 10th order (effective cavity length is approximately $7.8\mu m$), b) cavity modes at 35th order (effective cavity length is approximately $27.1\mu m$), c) cavity modes at 60th order (effective cavity length is approximately $46.44\mu m$). UPB (left side of the image) is clearly visible even with the high absorption of 12 QWs, and it is possible to easily determine Rabi splitting. A second LPB very negatively detuned corresponding to a lower longitudinal order also appears for l=29 and l=51 due to the reduced free spectral range.

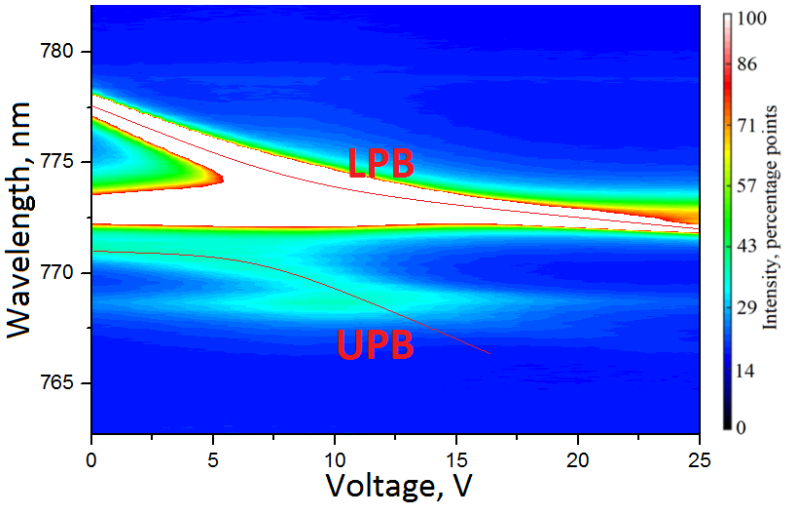

Figure 3.2: Polariton wavelength versus voltage/relative cavity length and color representing emission intensity. This anticrossing graph shows that at great cavity length (36th order, effective cavity length is approximately $14\mu m$), the system is still in the strong coupling regime. This is because exciton and cavity dispersions (marked in the figure with thin red lines) do not cross each other, a sign of polariton formation.

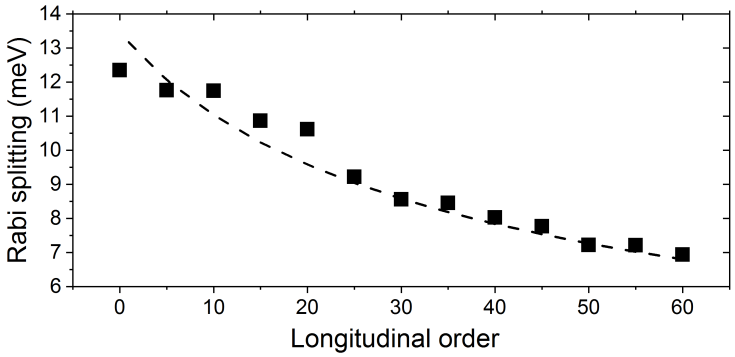

Figure 3.3: Rabi splitting size dependence on longitudinal order/relative cavity length. Rabi splitting decreases nonlinearly from 12.3 meV at 60th order to 7 meV at 0th order. Every additional order corresponds to an additional $385.75nm$ of the cavity length. Dashed line represents theoretical fitting of the Rabi splitting as a function of L_{eff}.

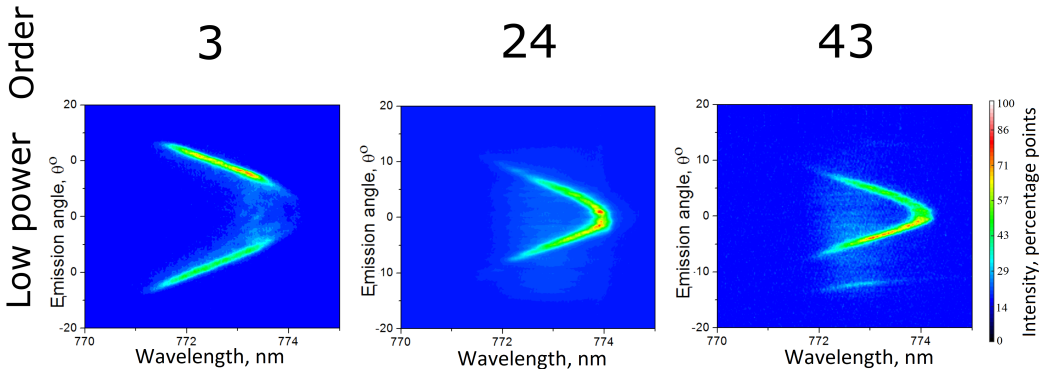

Figure 3.4: Polariton emission intensity in emission angle-wavelength space showing LPB curvatures at different cavity wavelength orders, but with the same LPB bottom wavelength of 774nm. Because of the decreasing Rabi splitting, LPB becomes steeper with increasing cavity length.

touching. Further lengths were calculated by counting the number of longitudinal modes. As expected Rabi splitting decreases with increasing order (Fig. 3.3), it was theoretically shown that Rabi splitting should scale as $1/\sqrt{L_{eff}}$, where L_{eff} is the cavity length plus the electric field penetration into the DBR mirrors ([17]).

During this experiment, Rabi decreases by 1.78 times from 12.3meV to 7meV with the change of effective cavity length from 2λ to 32λ. The overall cavity length change was measured to be $23\mu m$. This relationship is nonlinear and can be fitted with $\Omega_{Rabi} \propto 1/\sqrt{L_{eff}}$. It is possible that the maximum Rabi could be slightly higher, because it is unclear if the DBR mirrors are touching or there is a speck of dust preventing them from touching. The Rabi is decreasing because of decreasing overlap between QWs and the electric field energy. Changes in the LPB curvature are direct evidence of changes in the Rabi, which can be clearly seen from the LPB images at different orders (Fig. 3.4). LPB becomes steeper with increasing cavity length, because the Rabi splitting is decreasing, which leads to smaller effective polariton mass. The results are directly comparable to one another, because all measurements were taken with the LPB bottom always being at the same wavelength (774 nm).

3.3 Polariton Emission Intensity vs. Different Cavity Length

3.3.1 Data

After the Rabi vs. cavity length experiment, another experiment was carried out to test how a change in the Rabi and the cavity length will influence the sample emission. This led to a surprising result: the sample emission oscillated as a function of the cavity mode order. This led to a more detailed investigation of the effect.

The experiment's steps were as follows. Sample emission as an angular resolved spectra was taken at low power excitation ($200\mu W$) using single-mode (excitation at 734nm) and multimode fibres (excitation at 743nm) for excitation. Excitation wavelengths were different by an accident, but it does not impact any physics behind this experiment. Two different fibres were used: the bigger multimode fibre core allows more power to be coupled through it, but the single-mode fibre creates a higher power density and a smaller excitation spot. LPB was set to be fixed at 1601.94meV energy (774nm wavelength), 5meV below exciton energy level (1607.13meV, 771.5nm). The fixed energy allows the comparison of results from different cavity orders. Then, to observe the total intensity of the measurement, the emission intensity was integrated over k-space and plotted against the cavity order. The graph (Fig. 4.4) shows how the intensity is oscillating and decreasing overall with increasing cavity length. Both single-mode and multimode excitation has the same tendency. The only differences are that multimode excitation peaks at slightly higher orders and its peaks are broader.

Polariton emission intensity oscillates when the cavity mode order is changed, with the maxima observed using single-mode excitation at orders 4, 23 and 41. The total intensity varies from $12.4 \cdot 10^6$ to $5.3 \cdot 10^6$ at maximum points and stays quite level at minimum points at just below 10^6. The total intensity decreases 2.3 times at peak values (in this section, "peak values" refer to the orders at the highest total intensity values). The oscillations have a period of 18.5 orders.

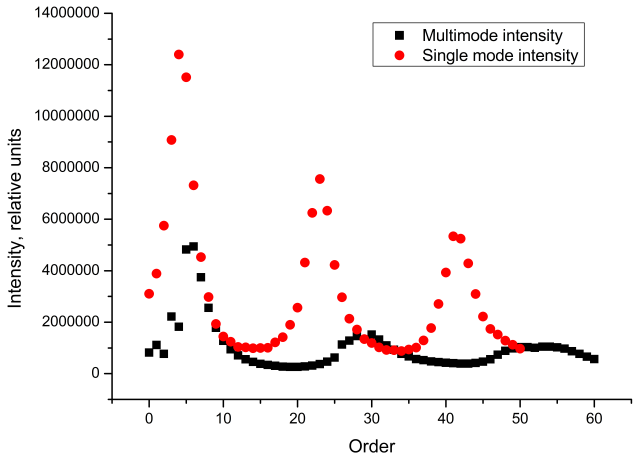

Figure 3.5: Emission intensity versus cavity order/relative cavity length showing integrated emission with a mode at a wavelength of 774nm with low power excitation for single-mode and multimode fibre.

Similar behaviour is observed in the case of excitation using a multimode fibre, but the maxima are observed at orders 6, 29 and 52. The total intensity varies from $5.6 \cdot 10^6$ to $1.1 \cdot 10^6$ at maximum points and is around $0.4 \cdot 10^6$ at minimum points (these numbers are not directly comparable to results using single-mode fibre). This shows that the total intensity decreases by 5 times at peak values, which is twice as large an amplitude than observed when using a single-mode fibre, but also with maximum value almost twice as low. In this case, the oscillation period is 23 orders.

3.3.2 Explanation

A good explanation of this effect is a destructive interference effect. Inside of the microcavity, light reflects from the DBR mirror and interferes with the light going in the opposite direction. If the cavity length is not the multiple of the light wavelength, then the reflected light decreases the intensity of the standing wave inside of the cavity, and the actual power inside is lower than expected.

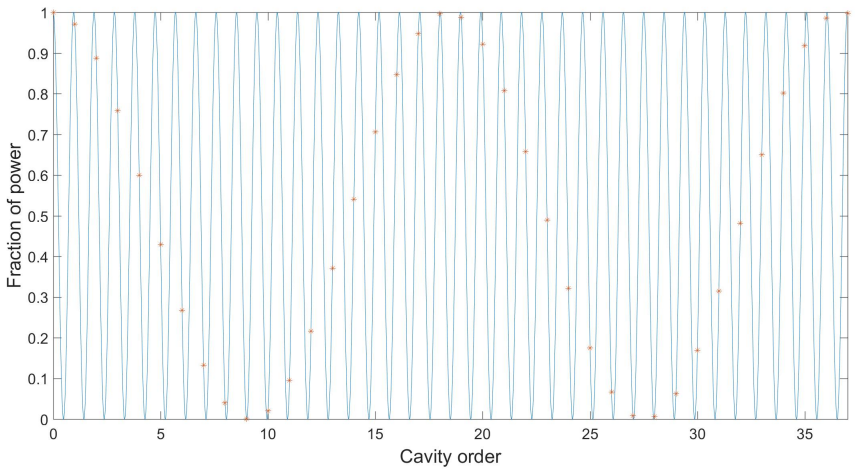

Figure 3.6: Power fraction versus cavity order/cavity length. Destructive interference effect in an open cavity using an excitation at a wavelength of 734nm (blue line). Depending on the cavity length, the excitation power inside the cavity oscillates from full power to 0. During the measurement, the cavity was optimised for maximum collection at the sample emission wavelength of 774nm. This means that the sample was measured at cavity lengths that are multiples of 774nm wavelength. This caused the effective excitation power not to be maximum during measurements, but at powers marked by red stars. This clearly repeats the oscillation measured in the integrated emission measurement.

This should also directly change the cavity reflectivity as the destructive interference at the wavelength of the excitation laser would decrease the amount of the light that penetrates inside the cavity and would increase the reflectivity at this wavelength. This also explains the intensity maxima oscillating at different order intervals as different wavelengths were used, which means that the destructive interference strength is different at different cavity orders for single-mode and multimode fibre excitations.

This is a good explanation in this case, because the excitation and emission wavelengths are different. This means that the destructive interference appears at the excitation wavelength, because the cavity is always set for the maxima at the wavelength of QWs' emission (774nm). Accordingly, the actual excitation power in the cavity is oscillating as the excitation power wavelength gets in and out of the phase. The observed oscillations have a period of 18.5 orders using a single-

mode fibre excitation and 23 orders using a multimode fibre excitation. This effect can be theoretically calculated. The excitation wavelength for the single-mode (multimode) excitation is 734nm (743nm), and the emission wavelength is 774nm (774nm). The wavelength difference is 40nm (31nm). The excitation power is oscillating and so $\frac{734nm}{40nm} = 18.35$ ($\frac{743}{31} = 23.97$). This agrees well with the experimental data. The multimode fibre result, because of the fibre's larger radius, can give additional destructive interference effects, which would not be covered by a simple theoretical calculation and therefore reconciling the difference between the theoretical prediction and the measured data is different. Nevertheless, the MATLAB simulation was performed to prove this for the single-mode excitation case (Fig. 3.6). Using 734nm for excitation and 774nm for emission gives an oscillation period of 18.5 orders, which is an excellent agreement with the theoretical prediction.

3.4 Coupled Cavities

3.4.1 Introduction

The top sample with coupled mirrors was received from the University of Oxford, containing rows of coupled mirrors with different centre-to-centre distances arranged in a 13x13 array. These distances varied from $10\mu m$ to $7\mu m$ and allowed the investigation of the transition from uncoupled to coupled cavities. The mirrors can be seen in an optical microscope image in Fig. 3.8. The main parameters of the concave mirrors are the radius of curvature of $6\mu m$ and the diameter of $4\mu m$. The sample features were created using a focused ion beam (FIB) milling process into a silica substrate and then coating it with 11 pairs of SiO_2/TiO_2 quarter wavestacks, discussed in "Sample Structure and Growth" section in Chapter 1. This sample was characterised and used to investigate the influence of the top sample's angle on coupled cavities' resonance and the influence of the cavity length on coupling strength. The coupling strength determines the energy difference between bonding and antibonding states in the case when the energy detuning between unperturbed cavity modes is zero. For these experiments, the bottom sample with a 31 paired $Al_{0.85}GaAs/GaAs$ DBR, and a single $In_{0.04}GaAs$

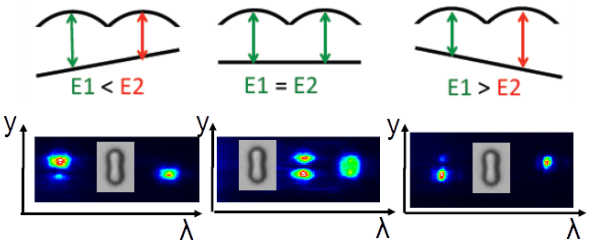

Figure 3.7: The figure shows the modes at different sample angles. Two separate modes are visible at large angles, which indicates that the modes do not couple and are placed in different coupled mirrors. On the other hand, the same modes become bonding-antibonding modes when the samples are parallel. The energy of modes adds to the resonance, and the emission is collected from either the mode covering the centres of both coupled mirrors or from the mode covering the region between the concave mirrors.

QW was used.

3.4.2 Manipulation of Coupled Cavity Resonance using Angle

An open cavity allows changes not only in the cavity length, but also in the angle of the top sample. This enables investigation into the possibility of bringing coupled cavities into or out of coupling by changing the resonance between the energies of the cavities. This process is possible because by changing the angle of the sample, one cavity length increases and another decreases (or increases by a smaller amount, depending on where the rotation axis is), which decouples the cavities.

The cavity-coupling dependence on sample angle measurements was measured, and Fig. 3.7 helps to visualise the results. The energy detuning between the cavity modes in different mirrors is greater at a large angle between the mirrors, which corresponds to two different energy levels at different positions. With a decreasing angle, the mode energies become similar, and a photonic molecule is formed with bonding and antibonding modes, where the bonding mode covers the position between the two mirrors. Splitting between modes also decreases.

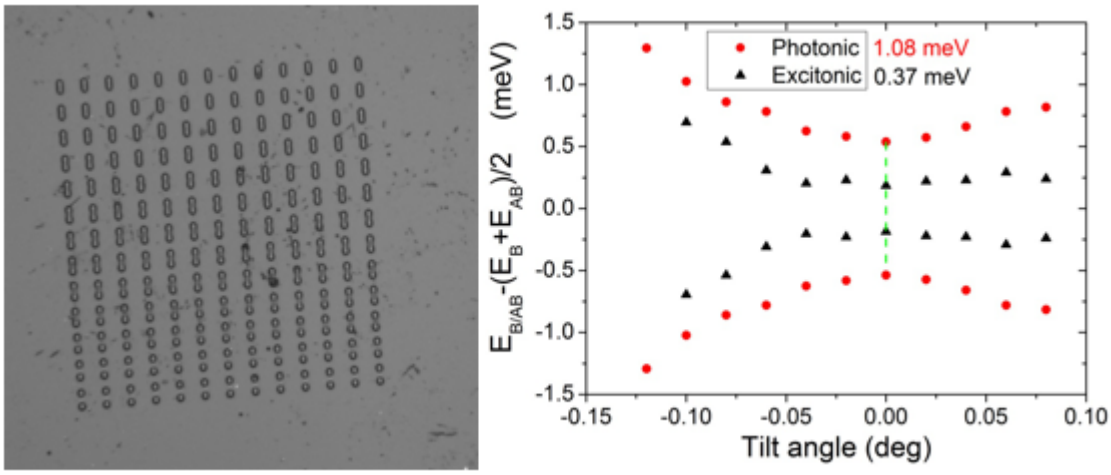

Figure 3.8: Investigated coupled mirror sample is on the left. All concave mirrors have $RoC = 6\mu m$, but the centre-to-centre distance varies from $10\mu m$ (bottom left) to $7\mu m$ (top right). The coupled concave mirror bonding, anti-bonding mode anti-crossing with changing angle is on the right. The anticrossing was found to be greater for more photonic than excitonic polaritons. The separation changes from $0.37meV$ to $1.08meV$.

The results of this experiment can be seen in Fig. 3.8. Here the energy of ground-state bonding-antibonding modes can be seen for different cavity angles. 0° represents the configuration when both mirrors are perfectly parallel. This is shown in Fig. 3.8, where the greatest coupling is achieved when the mirrors are parallel, and the coupling decreases with an increasing angle. The results show that by changing the angle from $-10°$ to 10°, the energy of the cavity resonances changes correspondingly, but never crosses. The smallest difference between the modes shows the size of the coupling strength. The measurement was repeated for excitonic and photonic polaritons (explained in Fig. 3.9) with 0.37meV and 1.08meV coupling strength respectively. The greater splitting in the more photonic case can be explained by the fact that cavity coupling happens through the photonic part. Thus, the larger the photonic part, the stronger the coupling.

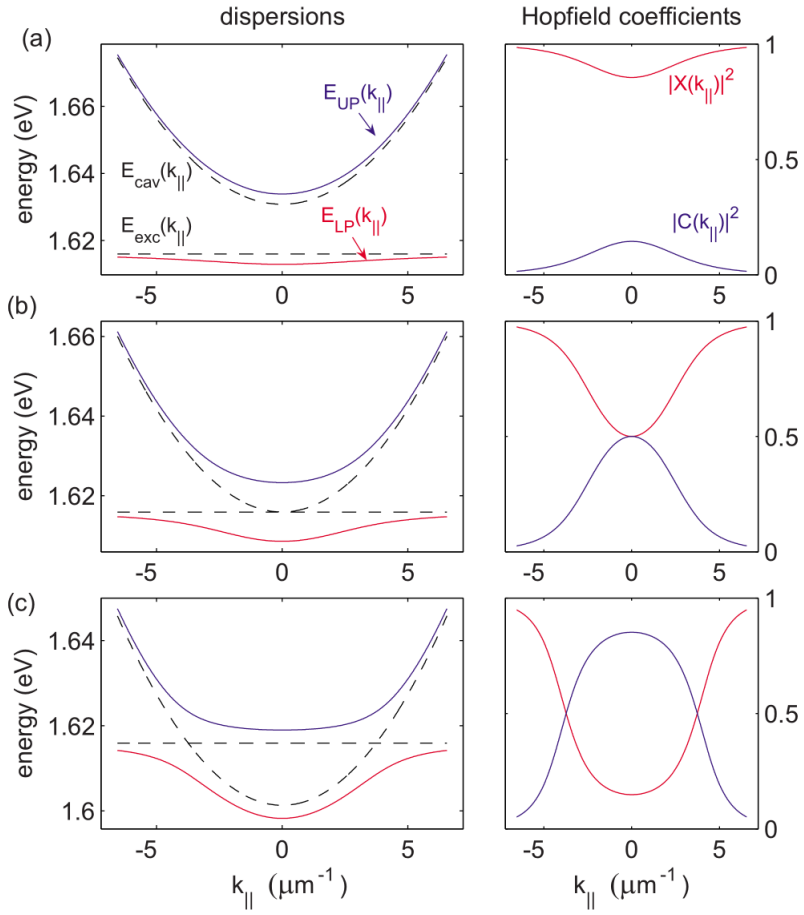

Figure 3.9: Figure taken from [32]. Left column represents polariton energy dependence on the in-plane wave number and right column represents Hopfield coefficient dependence on the in-plane wave number. Row a) shows situation at positive detuning, b) at resonance and c) at negative detuning. Excitonic polaritons are associated with positive polariton detuning as exciton's Hopfield coefficient ($|X(k_{||})|$) is higher than the photon's Hopfield coefficient ($|C(k_{||})|$) at 0 in-plane wave number, which means that properties of such polaritons are closer to the properties of the excitons. Following the same logic photonic polaritons are associated with negative polariton detuning.

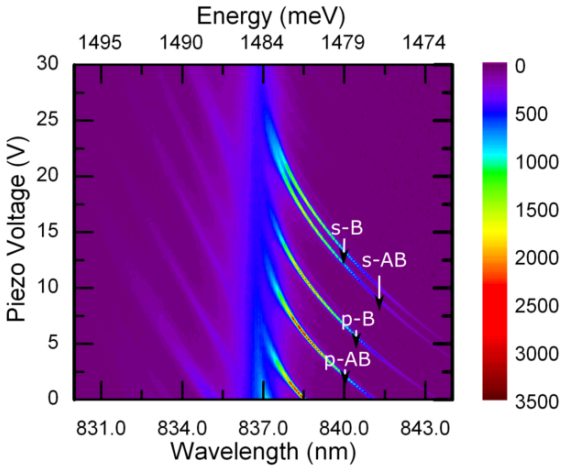

Figure 3.10: Sample emission intensity as a function of wavelength or energy and piezo voltage, which increases cavity length. Anticrossing can be seen as emission lines do not cross exciton energy at 1485 meV, showing that polaritons can form in a coupled cavities system. Anticrossing is visible not only for the longitudinal bonding-antibonding modes, but for other modes as well. Drop in intensity is seen above 1485 meV, because polaritons scatter to lower energies.

3.4.3 Sample Characterisation

First, the anticrossing scan was performed to make sure that the strong coupling regime is possible using coupled cavities. Fig. 3.10 shows clear anticrossing and proves that polaritons can be formed in such a system. Measured Rabi splitting is 3.5meV for 7.7μm centre-to-centre distance coupled cavities with an exciton at 1485meV.

Two other interesting parameters of coupled cavities are bonding-antibonding (B-AB) modes splitting dependence on detuning and coupling strength dependence on centre-to-centre distance between concave mirrors. The data extracted from Fig. 3.10 allows the determination of B-AB modes splitting for changing detuning. It was observed that the mode splitting decreases linearly with increasing positive detuning (Fig. 3.11a).

The coupling strength was determined by measuring the smallest splitting between B-AB modes while tilting the angle between mirrors for many different coupled cavities with centre-to-centre distances varying between 7.5μm and 7.9μm.

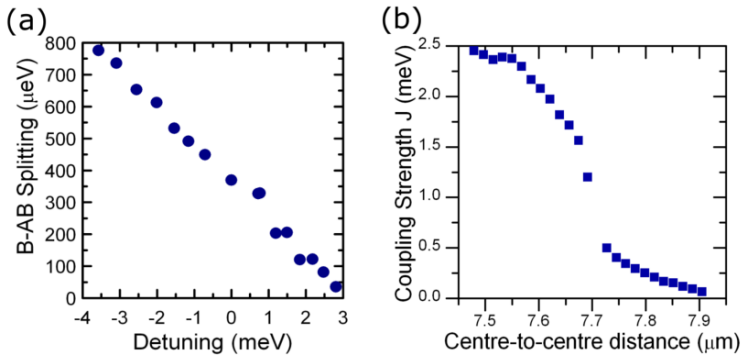

Figure 3.11: a) B-AB mode splitting changes with changing detuning for a $7.7\mu m$ centre-to-centre distance between concave mirrors. It is showing a clear decreasing trend, with increasing positive detuning. Data were extracted from the anticrossing scan (Fig. 3.10). b) Coupling strength for various centre-to-centre distance concave mirrors, showing a clear transition at $7.7\mu m$.

This technique will be described and investigated more in the next subsection. A very sharp transition between coupled and uncoupled cavities was observed when the centre-to-centre distance is less than $7.9\mu m$ (Fig. 3.11b). Another coupling strength threshold was clearly achieved at $7.7\mu m$, when it increased sharply from 0.5meV to 2.4meV. This can be explained by a very small beam waist of longitudinal modes. The highest measured coupling strength value reaches $2.5meV$ at $7.5\mu m$ centre-to-centre distance and becomes 0 at $7.9\mu m$.

3.4.4 Coupling Strength Dependence on Cavity Length

As already mentioned in the theory section, the coupling between two concave mirrors can be changed by milling concave mirrors at different distances between their centres. Also, the same effect can be achieved by changing the angle between two DBR mirrors, which does not change coupling, but changes the resonant condition by making them resonant or out of resonance [97]. Another in situ method has also just been published, which involves an inter-cavity coupling strength change with a changing cavity length [98]. This effect occurs because mode waists increase with greater cavity lengths and photonic modes overlap more in the top DBR mirror (Fig. 3.12). Thus, non-coupling cavities begin coupling, and the coupling strength of already coupling cavities increases. This thesis will

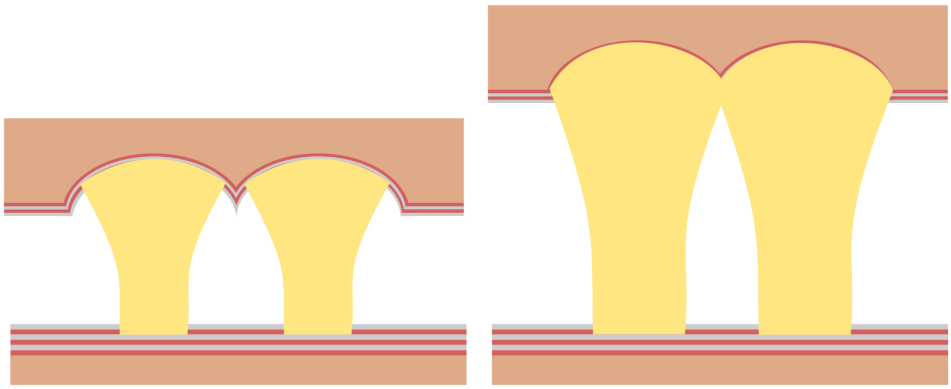

Figure 3.12: Illustration shows how the mode waist increases with increasing cavity length in an open-cavity system. This leads to increasing photonic mode interaction, increasing coupling strength and increasing separation between polariton bonding and anti-bonding modes.

cover a systematic study of this effect, which has not been done previously.

In the experiment, the bonding mode was tuned to 844nm-1469.1meV (and then everything was repeated at 840.5nm-1475.2meV) at different cavity lengths, when the cavity mode order changed from 0 to 9. It was not possible to measure higher cavity mode orders, because at longer cavity lengths, the mode linewidth becomes too great. This is caused by diffraction losses, and it becomes impossible to determine the precise positions of modes. The experiment was performed at two different wavelengths to check how coupling strength depends on detuning. It was set to be 844nm-1469.1meV to observe more photonic and 840.5nm-1475.2meV to observe more excitonic polariton properties, which correspond to the detuning of -14.15meV and -8.05meV respectively.

The reference coupled cavity wavelength was needed, because it was required to have the bonding mode at the same energy. Also, the emissions from 4 coupled cavities were seen and measured at the same time to increase the number of studied cavities and minimise the risk of measuring a defective cavity. The reference cavity was measured at two wavelengths to study if there is any difference in behaviour between excitonic and photonic polaritons with respect to changing cavity length. The initial difference between more photonic and more excitonic

polaritons is that more photonic polaritons have greater initial mode coupling.

The coupling strength was extracted by varying cavity angle and finding the minimum energy difference between bonding and anti-bonding modes. This method ensured that the detuning between both cavity modes was zero and that the energy difference between formed B and AB modes corresponded directly to the coupling strength.

The experimental results revealed that the coupling increases nonlinearly with increasing cavity length and plateaus at greater cavity lengths (figure 3.13). The same trend was noticed both for more excitonic- and more photonic-like polaritons. We observed that the ratio between the initial and the final coupling strengths at 0th and 9th cavity mode orders were different for all mirrors (mirrors differ by initial coupling strength - different separation between cavities), but stayed very similar, ranging from 1.25 to 2.92. Every coupled mirror had the same ratio in both more excitonic and more photonic cases. All coupling strengths flatten out at the highest cavity orders, and curves suggest that they would not increase much more even at much greater cavity lengths. This probably happens when the mode covers the whole concave mirror at a large separation between the mirrors, and its size cannot increase any further. The measurements were accurate because most of the measured mode wavelengths moved by less than 0.8meV (Fig. 3.14). This experiment shows that coupling strength between concave mirrors can be precisely chosen depending on the required situation.

3.5 Refractive Index Investigation and Effective Mass

The open cavity allows easy changes in the separation between the two DBR mirrors. This has an effect on the effective refractive index of the cavity, because the cavity region consists of three different regions: bottom DBR, top DBR and air space. There is a thin layer (usually the thickness is between λ and 2λ) of semiconductors containing quantum wells on top of the bottom DBR with

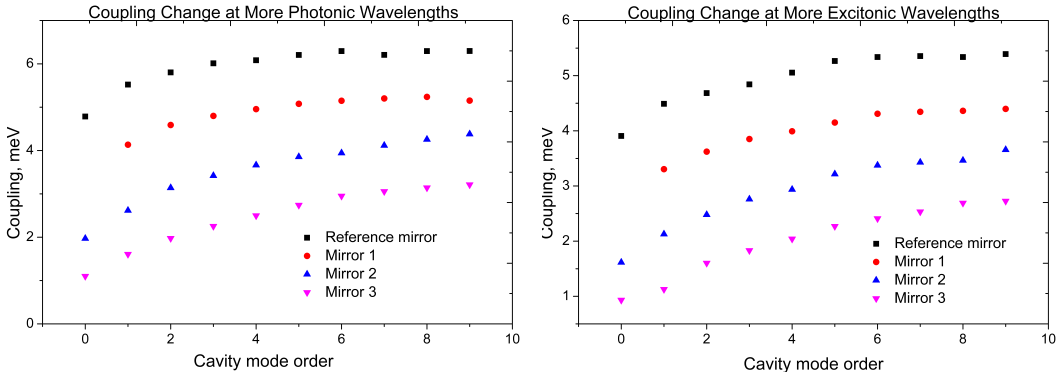

Figure 3.13: Illustration shows how the mode splitting (mode overlap) changes with different cavity lengths for more photonic polaritons (on the left) and more excitonic polaritons (on the right). The different curves represent different coupled mirrors with different separations between cavities, and the black squares are from the reference coupled cavity with a separation of 7.7μm. All mirrors show a coupling increase, but at greater cavity lengths, the increase stops or slows.

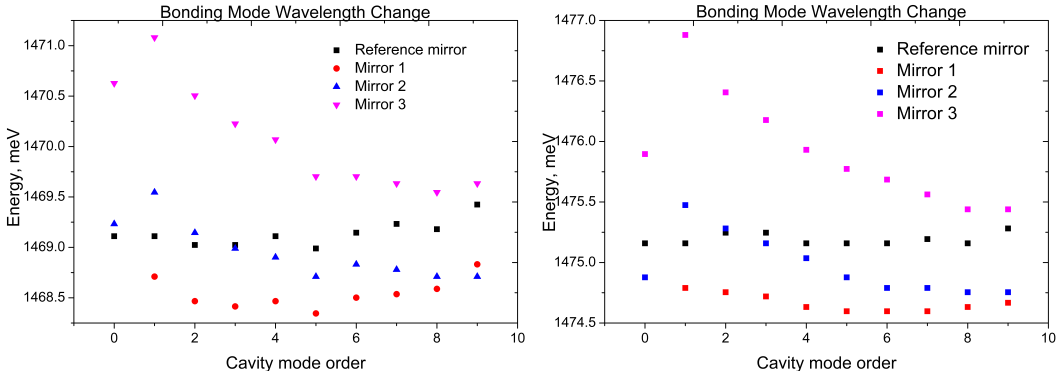

Figure 3.14: Illustration shows how the wavelengths of modes change with different cavity lengths for more photonic polaritons (on the left) and more excitonic polaritons (on the right). The different curves represent different coupled mirrors with different separations between cavities, and the black squares are from the reference coupled cavity with separation of 7.7μm. Most of the modes are quite stable and move by less than 0.8meV.

a constant refractive index of around 3.5. Another part of an open cavity, the air gap, has a refractive index of 1, but the thickness changes depending on the order and detuning. This change also influences the effective refractive index of the whole cavity, which depends on the proportion between the thickness of semiconductor layer and the air layer. The thicker the air layer, the lower the effective refractive index is. With increasing cavity length only air space increases and hence the refractive index should decrease.

The experiment was performed to measure the change in the effective refractive index of the cavity region with changing cavity length, which was determined in both strong and weak coupling regimes. Theoretically, the refractive index should not depend on this effect. It was also expected that the refractive indices of different cavity orders will not have the same values as the cavity length is always increasing, going from negative to positive detuning and increasing cavity orders, which should always decrease the semiconductor proportion in the cavity. The measurements showed that this is not the case.

The experiment was performed at two different regimes: weak and strong coupling, which depend on the applied laser power ($21mW$, below lasing threshold, and $200\mu W$ respectively). Weak coupling was chosen as a reference, because there should be no effect when polaritons do not form and it should have the effective mass of the pure photon. K-space images were taken at every order from the 0th order (the 0th order represents a 2λ cavity and then increases by $\frac{\lambda}{2}$ for every consecutive order) until the 8th order using planar mirrors. At the longer orders, the signal became too weak to measure. Multiple detunings were also measured for every order and then fitted with UPB and LPB curves (Fig. 3.15). Fitting was done using prewritten special MATLAB code. It required entering parameters manually and checking if calculated curves were visually overlapping with the curves from the spectra.

Using the MATLAB code, the refractive index was found by fitting calculated UPB and LPB (using Eq. 3.1 and Eq. 3.2) curves on the measured spectra (Fig. 3.15). These calculations require to know the exciton energy and Rabi

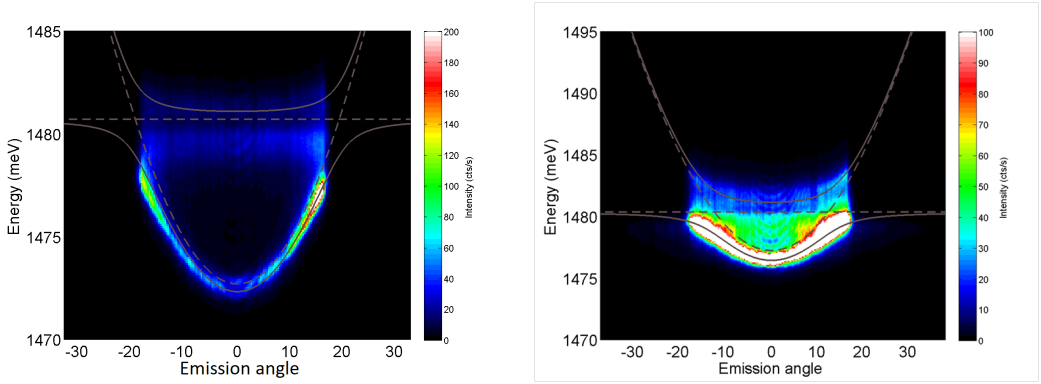

Figure 3.15: Images represent polariton emission intensity into energy-emission angle space. Fitting examples on k-space images from the experiment for a very negatively detuned cavity on the left and around 0 detuned on the right. It is harder to fit very negatively or very positively detuned cavities as either LPB or UPB is flat, and fitting depends only on one of the branches.

splitting, which were determined in previous experiments, the photon energy and the detuning, which were varied to fit data the best. First of all, the detuning value was varied until it matched theoretical and experimental values of the UPB or the LPB minima. Then having two mentioned parameters, the detuning and exciton energy, photon energy can be calculated (Eq. 3.3). The next step is to find the dispersion energies by applying Eq. 3.4 on previously computed photon energy using appropriate angle range and choosing the effective refractive index value, which would make the theoretical UPB and LPB fit the experiment data the best.

$$E_{UPB} = \frac{E_{PH} + E_X}{2} + \frac{1}{2}\sqrt{\delta^2 + \Omega_{rabi}^2} \tag{3.1}$$

$$E_{LPB} = \frac{E_{PH} + E_X}{2} - \frac{1}{2}\sqrt{\delta^2 + \Omega_{rabi}^2} \tag{3.2}$$

Where E_{UPB} is the upper polariton branch energy, E_{LPB} - lower polariton branch energy, E_{PH} - photon mode energy, E_X - exciton mode energy, δ - mode detuning, Ω_{rabi} - Rabi splitting

$$E_{ph}^{min} = \delta + E_x \tag{3.3}$$

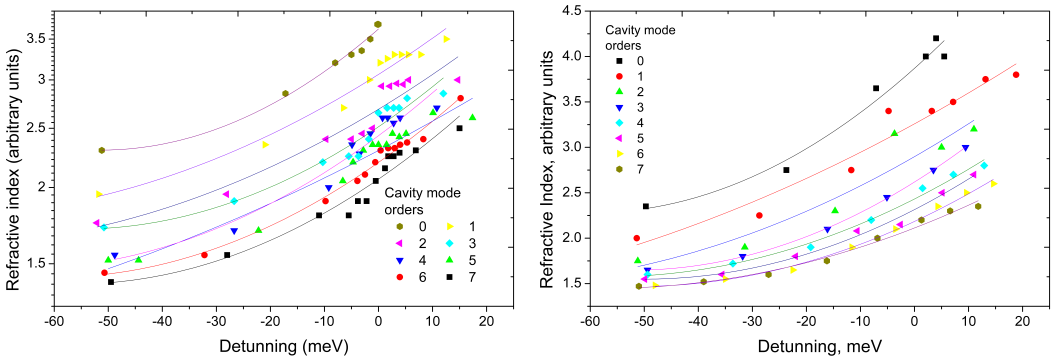

Figure 3.16: Refractive index dependence on detuning (from -50meV to 15mev) and increasing cavity length (7-8 orders) in strong (on the left) and weak (on the right) coupling regimes. The lines correspond to a second-order polynomial fit ($x^2 + x + c$), which shows very good fitting.

$$E_{ph} = \frac{E_{ph}^{min}}{\sqrt{1 - (sin(\frac{2\pi\Theta}{360n}))^2}} \tag{3.4}$$

Equations for the photon energy minimum and energies of photon dispersion. δ represents detuning, E_x - exciton energy and n is refractive index.

Experiment results are presented in the Fig. 3.16. In the strong coupling regime, the highest measured refractive index was 3.7, and the smallest was 1.4. The average of the second-order polynomial equation coefficients gives $4.56 \times 10^{-5}x^2 + 6.03 \times 10^{-3}x + 0.41$ with an average R^2 of 0.945. There is a slight jump in the refractive index around 0meV detuning, because UPB had to be used to fit the polariton dispersion curve instead of LPB, which becomes too flat to judge fit. In the weak coupling regime, the highest measured refractive index was 4.2, and the smallest was 1.46. 4.2 is more than the refractive index of GaAs (3.95), which has the highest refractive index in the sample, this is attributed to the accuracy of the measurement. The average coefficients were $2.72 \times 10^{-4}x^2 + 3.36 \times 10^{-2}x + 2.71$ with an average R^2 of 0.96. R^2 values show that a second-order polynomial describes the pattern very well.

Change in the effective refractive index directly influences the effective mass of polaritons (with LPB at the same energy) as the longer the cavity, the longer

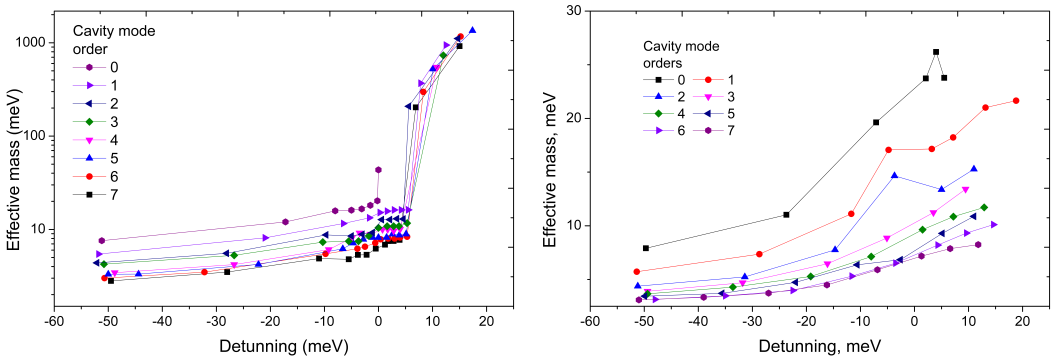

Figure 3.17: Effective mass dependence on detuning in strong (on the left) and weak (on the right) coupling regimes. A clear transition at 5 meV is visible, when the effective mass increases instantly around 20 times in strong coupling regime. In the weak coupling regime, the effective mass increases very slowly with increasing detuning and cavity length.

polariton is in the photon state, which is extremely light. In other words, the effective refractive index changes dispersion curve steepness, which shows the effective mass of polaritons. It was investigated how the effective mass is dependent on the detuning and the cavity length. The effective mass was found by applying the second derivative on the cavity dispersion energies (Eq. 3.5), which were measured in the effective refractive index experiment.

$$m = \frac{\hbar^2}{\frac{d^2 E_{LPB}}{d(k)^2}} \tag{3.5}$$

Here m is the effective mass, $\hbar$ - Planck's constant, k - light wavevector and E_{LPB} - the lower polariton banch energy

The results show a very steep effective mass change (at positive 5meV detuning) with increasing detuning in the strong coupling regime (figure 3.17 left), whereas in the weak coupling regime, change is gradual and much smaller (figure 3.17 right). However, the change in weak coupling regime is also nonlinear. Additionally, in a strong coupling regime, the effective mass changes over 200 times, from around $2.6{\cdot}10^{-3}\mathrm{m}_e$ (5meV) to over $0.51\mathrm{m}_e$ (1000meV). In a weak coupling regime, in contrast, the effective mass goes from around $4.1{\cdot}10^{-3}\mathrm{m}_e$ (8meV) to only $13{\cdot}10^{-3}\mathrm{m}_e$ (25meV). This difference shows that transition between excitonic

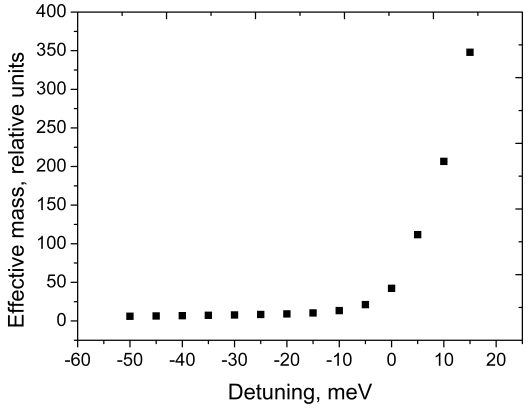

Figure 3.18: Illustration shows how the simulated effective mass increases with increasing cavity length in an open-cavity system and replicates results measured by the system. It confirms that the effective mass starts to increase rapidly after crossing 0mev detuning.

and photonic polaritons is very rapid, with the possibility to changing the effective mass over 100 times.

The steep effective mass increase with the increasing detuning was unexpected and so simulation was carried out to check the reliability of the result. It was done by calculating the effective mass using Eq. 3.2 and Eq. 3.1 with fixed parameters, with only the detuning value being varied. As can be seen (Fig. 3.18), it also shows a steep increase in effective mass just above 0 detuning, which confirms the rightness of the previous experiment.

This experiment also shows that the effective mass depends on the cavity order. It decreases as the cavity length increases at negative detuning in both weak and strong coupling regimes. In both regimes, the effective mass fits in the 0-10meV range at -50meV detuning and increases by a factor of 2-3 between the 0th and the 7th cavity mode order. At positive detuning in the weak coupling regime, the difference between the effective mass at the smallest and greatest cavity lengths increases, whereas in the strong coupling regime, the data does not show any significant dependence trend of the effective mass on the cavity length. Unexpectedly, the effective masses cross values of different cavity orders

and do not increase step-by-step in the weak coupling regime, but this can be explained by a very weak interaction between excitons and photons.

3.6 Birefringence and TE-TM splitting

Two effects can cause polarisation splitting in a microcavity. The first is called TE-TM splitting. It appears because the reflection phase depends on the polarisation phase reaching the DBR mirrors ([17]). This effect increases at greater reflection angles. The second effect is birefringence, which is caused by a material having two different indices of refraction, and it is the same for all angles. It happens, because of the anisotropy in the binding forces between the atoms, which are forming the crystal. These are usually uniaxial crysals belonging to the hexagonal, tetragonaland trigonal crystal systems, which have a direction that any passing light has the same speed. The mentioned direction is called the optic axis.

An experiment was performed to investigate how birefringence and TE-TM splitting effects change with different detunings. TE-TM splitting is interesting because it is an effective spin-orbit coupling for the photon. K-space emission was measured in two different polarisations, and the resulting spectra were subtracted from each other to see the difference between the dispersion curves. Two different detunings (-13.25 meV and -8.25) were measured, one more negative and one more positive (Fig. 3.19). The results (Fig. 3.19) showed that TE-TM splitting is present in the more negative detuning, but there is no birefringence as different polarisation dispersion curves are at the same energy, but the energy of curve branches separates. In the more positive detuning, in addition to TE-TM splitting, a birefringence of 0.24meV was observed. These spectra do not show a change of TE-TM splitting magnitude.

This can be explained by the fact that at a more positive detuning, polaritons are more excitonic, which means that the fraction of time that the light spends in the semiconductor layer increases. It also shows that used material is birefringent. In addition, this shows that polarisation splitting can have different effects on the

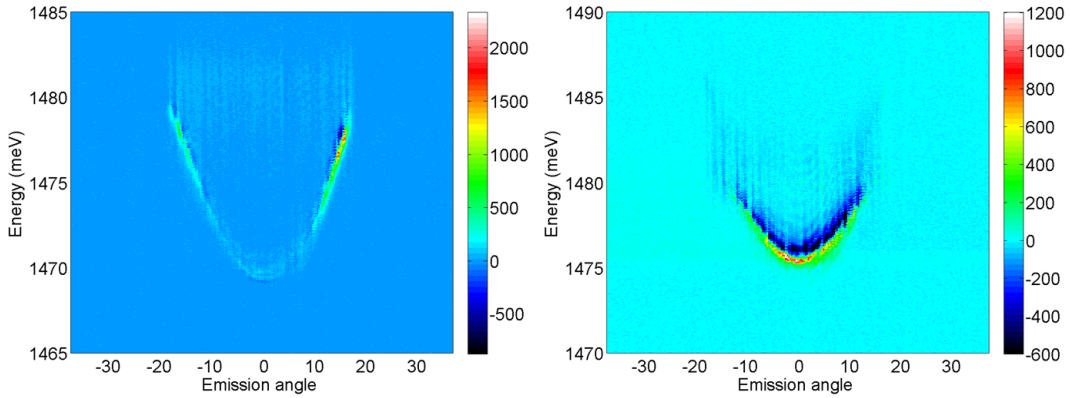

Figure 3.19: Polariton emission intensity in emission angle-wavelength space. TE-TM splitting and birefringence dependence on detuning. The data was obtained by measuring horizontal and vertical polarisation and subtracting their intensities from each other at every pixel. Because of this method, the graph shows two dispersions overlaid on each other, and the intensity varies from negative to positive values. Dark blue represents the horizontal polarization dispersion, and green represents the vertical polarization dispersion. The more negative detuning on the left experiences only TE-TM splitting, whereas the more positive detuning on the right also shows a birefringence effect.

Q-factor at different detunings as usually the signal is detected without a polariser and both polarisations combine into one peak. A better Q-factor can be achieved by using materials that do not cause a birefringence effect or one that is large enough to separate into two peaks. Another way is to design the cavity to not have birefringence at the required wavelength or to use non-birefringent materials.

While the main QW material, $GaAs$, has a cubic crystal structure and should not have birefringence effect, it is surrounded with other materials, which, for example, have Al and some other materials. This changes the crystal structure as well as it might induce stress, which might cause appearance of birefringence. Polarisation of the light has not been measured to check if it is elliptical, which should be the result of the birefringence.

3.7 Conclusion

This chapter concentrated on presentation of polariton linear properties such as cavity emission or Rabi splitting dependence on the cavity length. It also showed the possibility of coupling coupled cavities by changing the centre-to-centre distance or by varying the sample angle. It was also shown that coupled cavities' coupling strength increases when the cavity length becomes longer because of increased photon tunnelling between the coupled concave mirrors. However, the coupling strength increase has limits for different coupled concave cavities. The birefringence and the TE-TM effect change were observed for different detunings. The effective mass transition in the strong coupling regime was observed as well as the refractive index change while increasing the cavity length. Finally, the possibility of having polaritons in coupled cavities was proven.

Chapter 4

Polariton Condensation Under Non-Resonant Pumping in Open-Access Microcavities of Different Lengths

4.1 Introduction

Interest in the investigation of polariton condensation at various cavity lengths arises from the possibility of accessing a range of different Rabi splittings, which is not possible in solid cavities. Using open cavities allows the use of the same sample structure and composition. The number of QWs stays the same, so the exciton density per QW remains small at the condensation threshold, preventing the collapse of the strong exciton-photon coupling. During these experiments, it was noticed that the power required for the polaritons to condense varies widely over different cavity lengths. In addition, it was oscillating with increasing cavity length because of the oscillating excitation power in the cavity. This observation was surprising, as the required power for condensation had been expected to change gradually due to the gradually changing Rabi splitting. This chapter will focus on these unexpected findings and other experiments. All these measurements were taken using planar parts of the mirror. During experiments, the

sample was excited at the first Bragg mode using a laser with a wavelength of 734nm.

The sample used for the most of the experiments discussed in this chapter consisted of 12 GaAs/AlGaAs quantum wells (MQWs). They were divided into three sets of four QWs. Each set was designed to be located at the optical field antinode, the highest electric density. The GaAs wells are 7nm in width, and the barriers are 3nm, made out of $Al_{0.95}Ga_{0.05}As$. The exciton linewidth is 3meV, and the PL emission is at 771.5nm. The bottom DBR was made out of 30 alternating layers of $AlAs/AlGaAs$. The top mirror is a flat dielectric DBR with concave mirror features made out of 10 dielectric $SiO_2/TiO2$ alternating layers of $\lambda/4n$ thickness. Strong coupling in the sample was observed with a Rabi splitting of 12meV for the shortest cavity length of 2λ, but it varies with cavity length.

4.2 Polariton Condensation Using a Non-Resonant Laser

Evidence of polariton lasing was achieved in an open-cavity system using a non-resonant laser excitation of 635nm, outside the stop band of the DBR, an SiO_2/TiO_2 11 paired DBR top sample and 12 GaAs QWs grown on 31 paired $Al_{0.2}Ga_{0.8}/AlAs$ bottom DBR sample with a Rabi splitting of 15 meV (Fig. 4.1). Other conditions during the experiment were a concave mirror with an RoC of 7 μm and zero detuning.

One of these graphs is a power scan (Fig. 4.1 left), which allows the identification of the lasing threshold, when a nonlinear increase in emission intensity is observed. This means that emission intensity is increasing with increasing excitation power at the same rate (linearly), until a particular power (40mW), when emission intensity increase rate suddenly becomes bigger and thus there is no continuity with the previous linear increase any more, showing so called nonlinear increase. At a critical density, the filling factor of the ground state is close to 1, and therefore, relaxation becomes stimulated by the final-state occu-

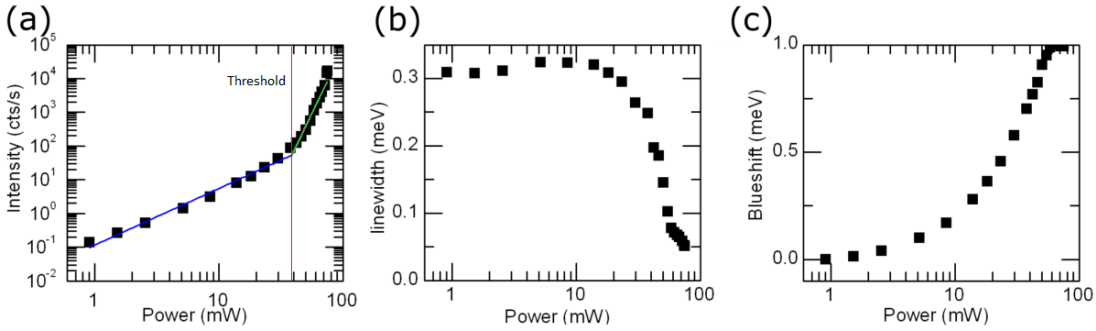

Figure 4.1: Evidence suggesting polariton lasing. From left to right: the emission intensity starts to increase non-linearly at 40mW power (threshold power marked by a red line), the polariton linewidth drops significantly and the system is blueshifting. This condensation was achieved for the longitudinal mode.

pation leading to a nonlinear increase of its intensity. A clear lasing threshold was observed at around 40mW power, and it can be associated with a nonlinear increase in intensity. Also the linewidth decreased from 300 μeV to 50 μeV, which becomes limited by spectrometer resolution, indicating the increase of the polariton's temporal coherence. The last evidence is an increasing blueshift, which reaches 1 meV and stops at high powers because the sample heating compensates for polariton-polariton interaction. The observed blueshift is much smaller than the energy separation between the photon mode and the LPB, which is 7 meV and was deduced by knowing the Rabi splitting and the detuning. This proves that the observed nonlinear increase in intensity and the increased temporal coherence is the result of polariton condensation.

Polariton condensation using a non-resonant big spot laser in a planar cavity has already been investigated in an open-cavity system [87]. The result was an intense emission line between the dispersion curve branches at a momentum space of around $k = 0$ (Fig. 4.2a, b). This can be explained by the increased potential created by the exciton reservoir.

It was theoretically proven that condensation can appear at $k \neq 0$ using a small excitation spot in the planar cavity ([99]). This can be explained by the polariton ballistic propagation from the big population region or localised states appearing

in disordered cavities. In other words, in the centre of the small spot, a potential barrier is created due to the polariton-exciton interactions. Condensed polaritons propagate from the region with high to low potential energy, gaining kinetic energy and finite momentum. As a result, the polariton condensate emission gains a ring-like structure in the momentum space.

During this experiment, a single-mode fibre was used to excite a spot of a few microns in diameter to observe the results of such a condensation. These results can be seen in the momentum space images in Fig. 4.2c, d, e and f. This effect was measured in two modes: image mode and spectral mode. The image mode shows the whole signal, which reaches the spectrometer (Fig. 4.2)e, f. In contrast, the spectral mode is a chosen vertical slice showing the energy level allocation. The polariton dispersion curve below the threshold (Fig.4.2c) has a shape of a cone. In the image mode, it fully covers the whole observable area (Fig. 4.2e). Above the threshold, the polaritons move to a finite k vector of the dispersion curve (Fig. 4.2d), which creates a circle form in the image mode (Fig. 4.2f).

4.3 Polariton Condensation Dependence on Rabi Splitting

In the previous chapter it was shown that changing the Rabi splitting directly changes the LPB curvature. With a decreasing Rabi - in other words, increasing the cavity length - the LPB curvature becomes steeper. In this section, results will be presented from the investigation of how this influences polariton condensation.

For this measurement, just as in the LPB curvature's dependence on the Rabi splitting measurements, the LPB energy was set to 774nm on three different orders: 3rd, 24th and 43rd. Then the power was increased until the polaritons passed condensation transmission. Finally, measured k-space LPB curves before and after the condensation threshold were compared.

Fig. 4.3, shows that with decreasing Rabi splitting, condensation appears at a higher wavelength, which means lower energies. It decreases from 1605.05meV at

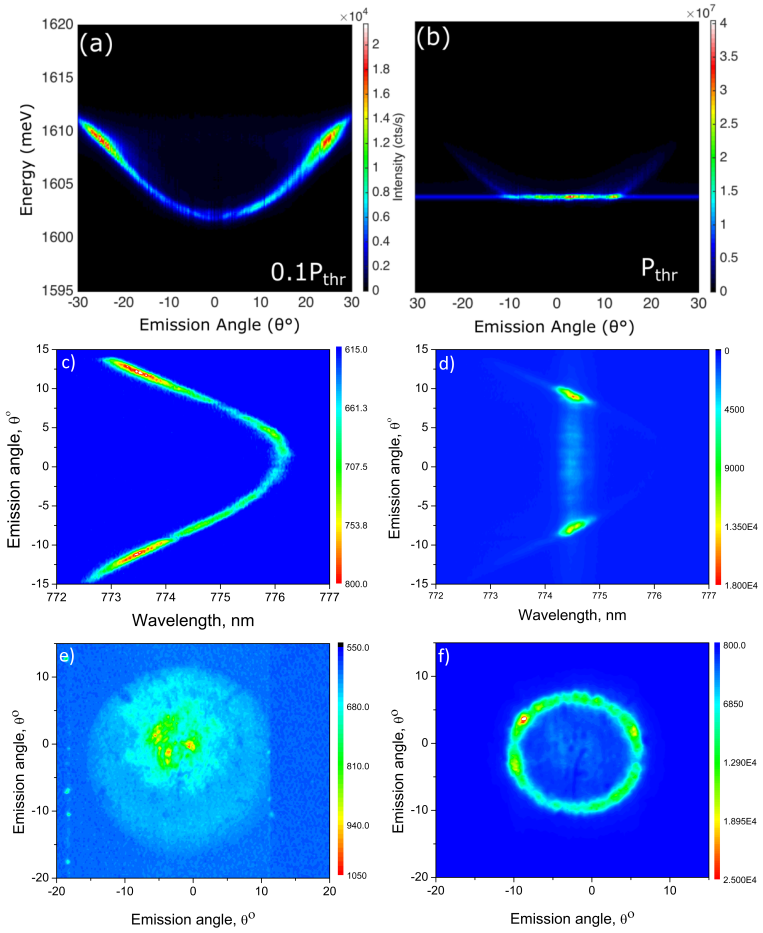

Figure 4.2: Polariton emission intensity in a),b) energy-emission angle space, c),d) emission angle-wavelength space and e),f) k-space. Condensation appearing around k=0 at blueshifted cavity mode energy using a multimode fibre excitation (a, b, taken from [87]) and condensation appearing at $k \neq 0$ using a single-mode excitation (c, d, e, f). Polariton emission in wavelength vs. emission angle space, showing the polariton dispersion below (images on the left at 500μW) and above the threshold (images on the right at 38mW). A, b, c and d were received using momentum space signal in spectral moe of the spectrometer, whereas e and f were momentum space signal observed in imaging mode.

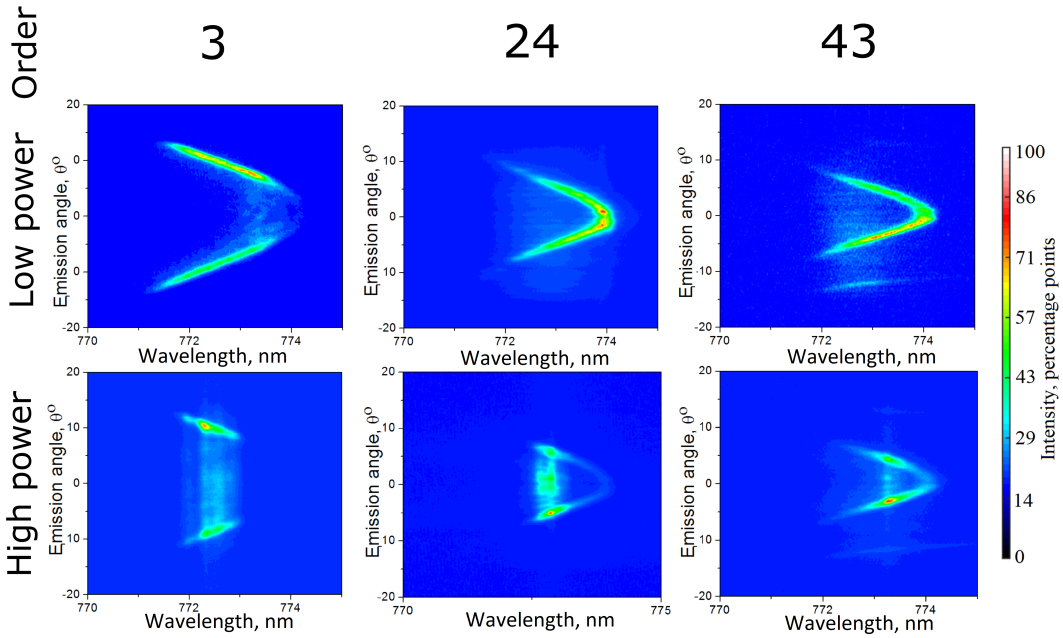

Figure 4.3: Figures represent sample emission intensity in emission angle-wavelength space. Condensation dependence on the Rabi and LPB curvature change. It gives evidence for a condensation energy drop with a decrease in cavity length by 1.5meV. Also, it is evident that the condensation stays on the LPB.

3rd order to 1603.43meV at 43rd order. This is a 1.5meV decrease in condensation energy by increasing the cavity length by 15.5μm. It can be associated with decreasing density of states and polariton mass, which allows the polaritons to scatter lower in energy during condensation. It is also evident that condensation appears on the LPB all the time.

4.4 Condensation Threshold Oscillation

After the Rabi vs. cavity length experiment (Chapter 3), another experiment was performed to test how a change in the Rabi and the cavity length will influence the polariton condensation threshold. This led to the following result: the polaritons' threshold of condensation oscillated as a function of the cavity mode order. This led to a more detailed investigation of the effect.

As measured and explained in the previous chapter, the emission intensity oscillates with the cavity length. The pump field excites a Bloch mode in the DBRs. With a variation of the cavity length, the amplitude of the pump field and the overlap of the pump field with the QW region varies, which leads to the oscillation of the effective power with the cavity mode order and hence the variation of the PL emission intensity and the condensation threshold.

This directly leads to the oscillation of the condensation threshold (Fig. 4.4, Fig. 4.5). This conclusion was reached after measuring threshold values using a power scan technique performed at the same LPB energy (1601.94meV, 774nm) at different cavity orders. Another key observation was that the condensation threshold gradually increases with greater cavity lengths. The lowest thresholds have been observed at the cavity mode orders when the emission intensity is maximised, corresponding to the maximum effective pump power in the QW region. When the emission is low, the condensation threshold is too high, so it could not be reached using a single-mode fibre.

Using a single-mode fibre excitation, the lowest threshold value is 3.6mW at 4th order. It increases to 14mW and 28mW at orders 24 and 41 respectively. The laser's 35mW power is not high enough to measure the highest thresholds in between. The repeating cycle is 18.5 orders. The threshold values show an increase of 7.8 times. Power coupled through a single-mode fibre was not enough to achieve condensation at every order, but the results still show a clear trend. There is a possibility that condensation might not appear at some wavelengths at all.

In the case of the excitation using a multimode fibre, it was possible to send more power through the fibre and hence achieve condensation at every single measured order. This gives a clear picture of the occurring effect. The results show that using a multimode fibre has the same tendency as using the single-mode fibre, but because of greater diameter, the effects are slightly harder to simulate, the peaks are at slightly different orders and they are not as sharp as those created by using a single-mode fibre (Fig. 4.5). Another difference between

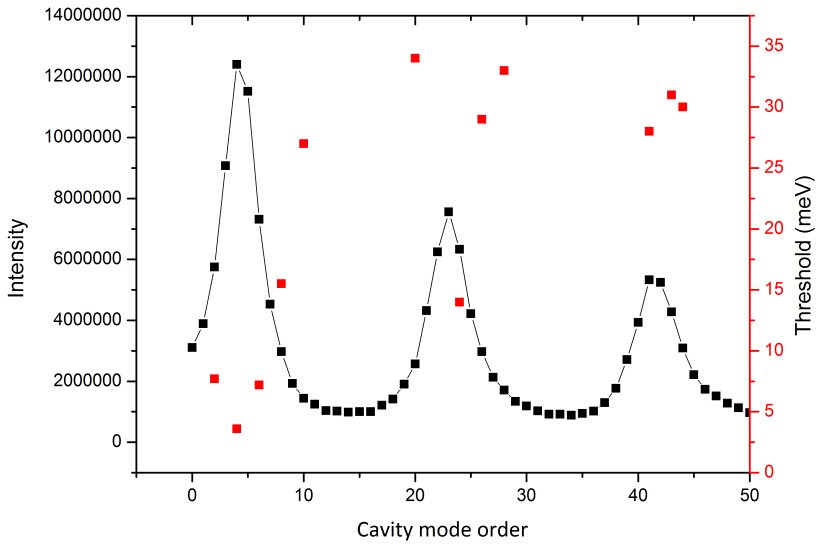

Figure 4.4: Sample emission intensity and lasing threshold versus cavity mode order/relative cavity length. Integrated emission with low power excitation and a condensation threshold at 774nm wavelength for a single-mode fibre. At orders when the PL emission intensity is low, the condensation threshold is so high that it could not be reached.

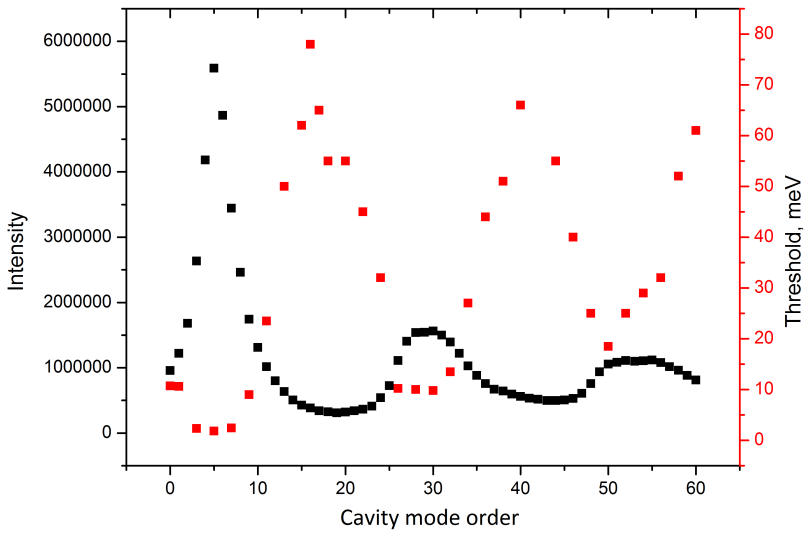

Figure 4.5: Sample emission intensity and lasing threshold versus cavity mode order/relative cavity length. Integrated emission, with low power excitation, and condensation threshold at 774nm wavelength for a multimode fibre.

the fibres is the angular divergence. It is greater using the single-mode fibre, but it is unknown if this plays a role in the measured effect.

For multimode fibre excitation, the lowest threshold value drops to 1.8mW at 5th order. Then it rises to 9.8mW and 18.5mW at orders 30 and 50 respectively. The repeating cycle is 23 orders. The maximum thresholds in between appear to be decreasing from 78mW to 66mW at orders 16 and 40 respectively. This value is different from the result for the single-mode laser. The increasing minimum threshold and decreasing maximum threshold values show that this oscillation is dampening with increasing cavity length. From the results, it is possible to conclude that a multimode fibre allows the attainment of threshold values that are up to twice as low and a greater variation in the lasing threshold, compared to the single-mode fibre results.

Since the effective pump power inside the microcavity changes with the cavity mode order, instead of plotting the absolute value of the condensation threshold,

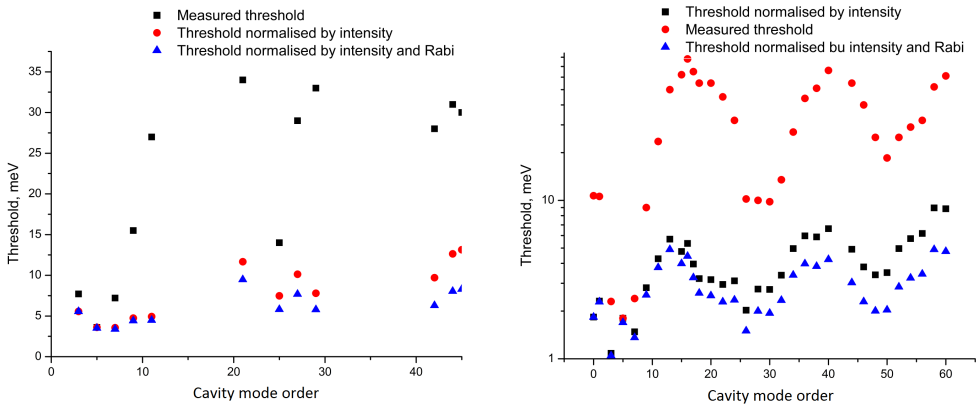

Figure 4.6: Sample lasing thresholds versus cavity mode order/relative cavity length. Threshold normalised with total intensity data and Rabi splitting values using single and multimode excitation laser.

it is reasonable to plot the effective threshold. This was obtained by multiplying the absolute condensation threshold by the normalised PL polariton emission below condensation threshold, which is normalised to the minimum intensity observed at a particular cavity order. Then the effective threshold was normalised to the Rabi splitting as the main experiment goal was to discover if the Rabi splitting is the only effect influencing the effective threshold change with increasing cavity length. This was done similarly to the previous normalisation: the effective threshold was multiplied by the ratio between the highest Rabi splitting and the splitting at the particular cavity mode order (Fig. 4.6).

The results show that the largest impact on the absolute threshold comes from the decreasing total intensity. It is especially visible when the multimode fibre is used. The Rabi splitting contributes a very small amount to the increasing threshold, compared to the total intensity. After taking account of these two effects, the lasing threshold is still increasing. Using a single-mode fibre, it increased more than twice, from 3.5mW to around 8mW. It increases from 1mW to around 4mW, a fourfold increase using the multimode fibre. The reason for this could be that with an increasing cavity length, a smaller part of electric field overlaps with the QWs, but this was not investigated further at the moment.

4.5 Blueshift

Investigation of the blueshift is also important to prove that polariton condensation and not photon lasing was actually achieved. There is much debate about what proof would be the best in this case. Generally, proof of the blueshift being less than the difference between the cavity mode and LPB is enough ([17]). However, a problem arises because this assumption does not take into account the redshift of the cavity mode, and it is not possible to measure it because UPB is not visible ([47]). This problem is why the best way is to show the ratio of the blueshift and the difference between the cavity mode and LPB. With an assumption that the UPB redshift is not greater than the LPB blueshift, the value of the previously mentioned ratio lower than 0.5 means that lasing is polaritonic and not photonic as the cavity mode did not redshift low enough in energy.

Blueshift is the difference between the energy of the condensate and the energy of LPB at 0 k-vector using low excitation power $E_{blueshift} = E_{condensate} - E_{LPB(k=0)}$ (Fig. 3.4). E_{cav} (the energy of the cavity mode) is calculated using the energy of LPB at 0 k-vector with low excitation power, the Rabi splitting at a particular order and the exciton energy. From the Fig. 4.7, it is visible that the blueshift is very small compared to the difference between the cavity mode and LPB. The blueshift is more or less constant, and the difference between the cavity mode and LPB is drastically decreasing with increasing order. Nonetheless, the ratio of the blueshift and the difference between the cavity mode and LPB even at the highest cavity lengths is still only around 0.5 (Fig. 4.8). It is safe to assume that it was polariton condensation over the whole range of orders, because the blueshift was not big enough to lift polaritons to the energy of cavity mode. $E_{CAV} - E_{LPB}$ is decreasing, because of the decreasing Rabi splitting. This means that the cavity mode is decreasing in energy, whereas the LPB mode stays at the same energy.

With increasing cavity order, the system becomes more photon-like, but blueshift is the same 1meV. This is because the threshold and the exciton densities are higher for a higher cavity order, which maintains the blueshift at the same value of 1meV.

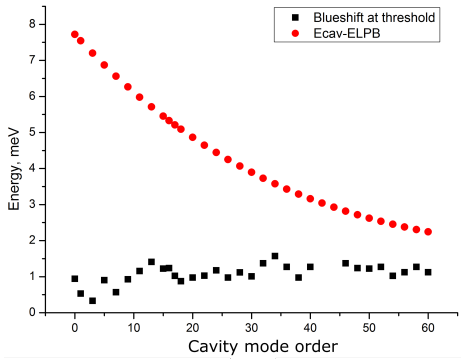

Figure 4.7: Polariton blueshift energy at the threshold and energy difference between cavity mode and LPB versus cavity mode order/relative cavity length. Graph shows the difference between the cavity mode and LPB as well as the mode blueshift at the threshold for multimode fibre excitation.

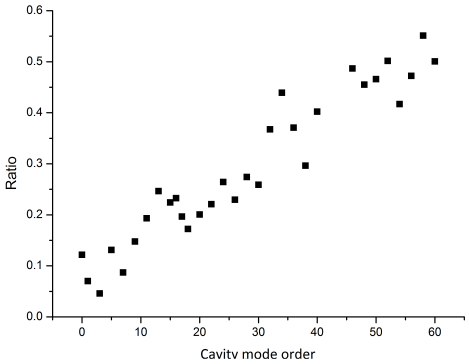

Figure 4.8: Ratio between the blueshift and the difference between the cavity mode and LPB for multimode fibre excitation versus cavity mode oerder/relative cavity length. This shows that blueshift becomes bigger in comparison to the difference between the cavity mode and LPB with increasing cavity length, which means that at some point polariton lasing will become photon lasing.

4.6 Optimum Threshold

The polariton condensation phase diagram is important, because it shows how the condensation threshold changes when various parameters are changed [49]. The condensation threshold is determined by the interplay between thermodynamics and relaxation kinetics. Here the detuning effect, which is described as a difference between the exciton and the bare cavity mode energies becomes very important. The bare cavity mode is described as the energy of the cavity mode without strong coupling with the exciton. $\delta = E_x - E_c$, where E_c is bare cavity energy and E_x is exciton energy.

Relaxation kinetics become more efficient with increasing positive detuning (polariton is becoming more excitonic), because of the greater exciton-exciton scattering rate. On the other hand, the polaritons can undergo BEC when the density is above the critical density if the temperature is low enough. This BEC transition temperature is inversely proportional to the mass of the polariton ([100]),

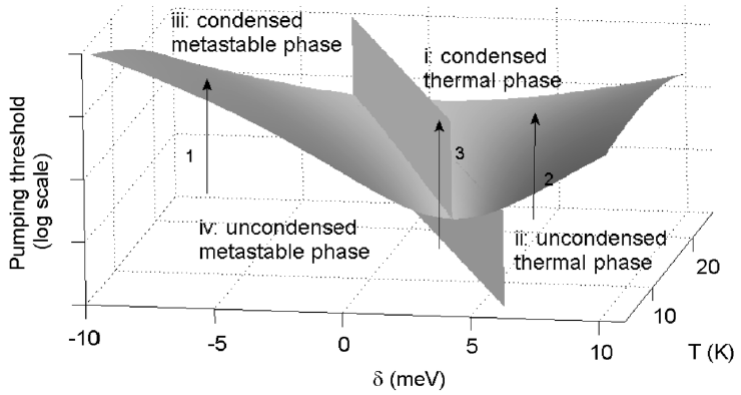

Figure 4.9: Illustration taken from [49]. Figure represents laser pumping/sample lasing threshold versus detuning (horizontal axis) and temperature (depth of the graph). It is a good example of the phase diagram, where the optimum detuning is found for a changing temperature.

so the polariton condensation becomes more thermodynamically difficult with increasing detuning as the polariton mass increases.

These two contradictory effects compete with each other and mean that the threshold value should decrease with decreasing detuning, because thermodynamics is the limiting factor in this range. Then the minima will be reached, where thermodynamics and the relaxation kinetics effects are equal. Further decreasing detuning will make relaxation kinetics the limiting factor, and so the threshold will start increasing again. Figure 4.9 shows such a phase diagram for different detunings and temperatures.

The novelty of this experiment is the study of various detunings with different values of Rabi splitting, hence different exciton fractions. The optimum threshold was found for different cavity length orders using multimode fibre excitation (Fig. 4.10). Since threshold oscillates vs. cavity order, the cavity lengths were chosen when the thresholds take local minimum values. This corresponded to 5th, 29th and 51st orders with Rabi splitting of 11.8meV, 8.56meV and 7.22meV respectively. The thresholds were carefully measured in the range of wavelengths. Then, knowing the Rabi splitting at this particular cavity order from the previous experiment, the cavity mode position was calculated. This allowed the detuning

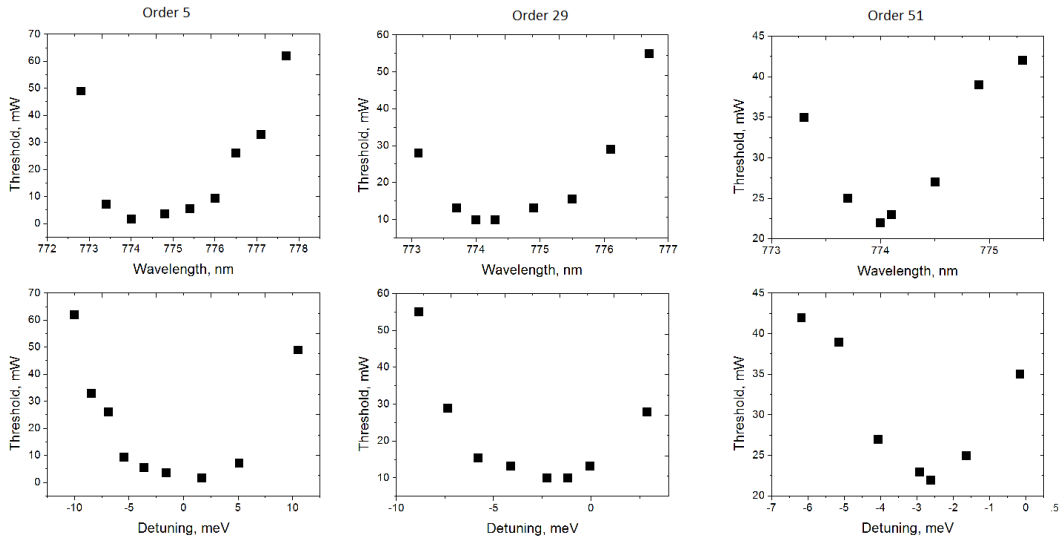

Figure 4.10: Figures show lasing threshold values at different wavelengths (top row) and different detunings (bottom row) for different cavity orders. Detunings were calculated using $\delta = E_{cav}(k = 0) - E_{exc}(k = 0)$. The top row indicates the optimum condensation threshold holding around a wavelength of 774nm with increasing cavity length from 5th order to 51th order for multimode fibre excitation, whereas the bottom row shows the optimum threshold dependence moving towards more negative detuning in the same conditions.

for every wavelength to be known.

The results showed that the lowest threshold moves from 1.8meV detuning at 5th order to -2.6meV at 51st order. This means that the optimum threshold favours decreasing detuning for increasing cavity order. Nevertheless, the optimum wavelength stays around the same - 774nm. It appears that the threshold depends only on the energy depth of LPB at k=0 with respect to the exciton level. At the more positive detuning, there is increased back scattering from LPB to the exciton reservoir, which leads to an increased threshold. At more negative detuning, the excitons need to lose more energy in order to scatter and condense to a k=0 state. Also, the threshold curve becomes steeper with increasing cavity length. This means that decreasing the Rabi makes thermodynamic and relaxation kinetics limiting factors vary more drastically.

4.7 Simulation

A simulation of the condensation phase diagram for this sample was carried out by Dmitry Solnyshkov. The calculations were based on semiclassical Boltzmann equations for microcavities. The method used is also described more in [101]. The parameters used for the simulation were as follows: Rabi splittings of 12meV, 8.5meV, 7meV; corresponding Q-factors for cavity lengths at measured Rabi splittings of 3500, 4000 and 5500, for 5th, 29th and 51st orders respectively; an exciton PL emission at around 770nm; an exciton linewidth of 3meV; 4K temperature; and an excitation wavelength of 739nm using a continuous-wave laser.

The simulation and measurements agree very well quantitatively and qualitatively (Fig. 4.11 and Fig. 4.12). The predicted lowest threshold and detuning values for the corresponding Rabi splitting are very close to the measured values. In both simulation and actual experiment, the optimum detuning values are around 2.5meV, 0meV and -2.5meV detunings for 5th, 29th and 51st cavity orders. The simulation also correctly predicts the narrowing of parabolas for decreasing Rabi splitting as well as its shift from negative to positive detuning and the increasing optimum threshold values. One more similarity between the simulation and the real results is the asymmetry of branches. The more negative branch tends to be steeper than the more positive detuning branch. The only difference is that the simulation predicts narrower polariton curves than were experimentally measured. The simulation supports the validity and correctness of the measurements.

4.8 Conclusion

These experiments give important knowledge about condensation threshold and excitation intensity dependence on cavity length and detuning. This process happens because small changes in the cavity cause large changes in the excitation power and the condensation threshold. It is very important to know the power oscillation over the cavity length effect when comparing properties of samples

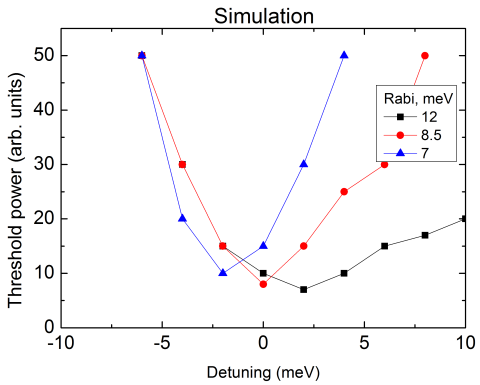

Figure 4.11: Sample lasing threshold versus cavity mode detuning. Graph represents D. Solnyshkov's simulation results. 12meV, 8.5meV and 7meV correspond to 5th, 29th and 51st cavity orders respectively.

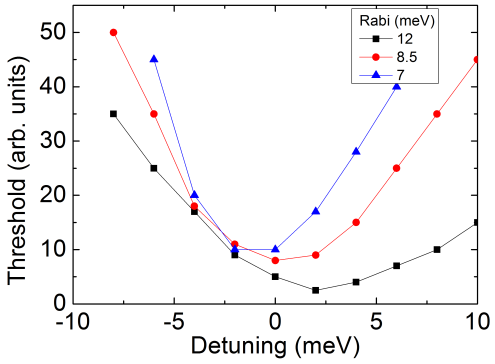

Figure 4.12: Sample lasing threshold versus cavity mode detuning. Graph represents the condensation phase measurements after intensity normalisation. 12meV, 8.5meV and 7meV correspond to 5th, 29th and 51st cavity orders respectively.

with different cavity lengths as a change of cavity length by one order gives a significantly different result. It also shows that a change in the cavity length can be substituted for an increase in the laser power to achieve the condensation threshold or a significant proportion of power over threshold. This study shows how Rabi splitting behaves with changing cavity length, while still having the same microcavity structure.

Chapter 5

Efficient Polariton Condensation Under Quasi-Resonant Pumping

5.1 Introduction

The easiest way to observe a polariton blockade or a strongly antibunched signal was identified as working in transmission mode. Thus, two different transmission setups were designed and assembled. This chapter will cover the measurements performed with this design. The designs of these devices were described in detail in Chapter 2. The first design is an upgrade to the previously used system, where the rearrangement of sample and piezo stacks allowed the collection of both reflected and transmitted light. The second design is the new transmission bath cryostat designed especially for this purpose.

5.2 Transmission Measurements Using the Transmission Upgrade of the Old System

5.2.1 LG_{00} Mode Blueshift

This experiment was performed to investigate LG_{00} mode blueshift dependence on the mode wavelength using resonant excitation. A polariton mode wavelength also depends on the exciting laser power. A higher power means a higher excita-

tion power density, and the polaritons are created with higher density. A higher polariton density increases repulsive interactions between the polaritons, which means that the next polariton added to the system will need to have higher energy. In other words, this will increase the required excitation laser energy (decrease laser wavelength). This effect is called blueshift, as the laser wavelength moves towards the blue colour. An open cavity allows measurement of how detuning (the exciton fraction changes in the polariton) influences this blueshift using a resonant laser. To measure this, the mode PL emission wavelength was measured at a low resonant excitation laser power ($\sim 70\mu W$). Then the power was increased to the maximum ($\sim 100mW$), the mode was located, the wavelength measured and the blueshift calculated. The graph of wavelength at low power vs. blueshift shows this dependence (Fig. 5.1). The blueshift increases exponentially with a decreasing wavelength towards the exciton wavelength. This increase is caused by two factors. First, at lower powers, the blueshift happens because of increasing polariton-polariton interaction. Then at 30mW power, the strong coupling regime is lost, and the blueshift increases much faster, because anti-crossing is no longer present and the mode at high power can cross the exciton wavelength. Also, the blueshift decreases with an increasing wavelength towards the exciton wavelength. Here, negative blueshift gives rise to the opposite effect, called redshift. Fig. 5.1 shows that the blueshift is increasing (decreasing) towards the exciton wavelength from higher (lower) wavelengths.

One explanation could be that this blueshift appears only from excitonic interactions. Another explanation is that at low power, the system is in strong coupling regime, which gives anti-crossing with the exciton wavelength, but at high power, the excitation system goes to the weak coupling regime, without anti-crossing, and so this gives bigger blueshift. Theory supports the first explanation, as resonant pumping does not create an exciton reservoir, which breaks the strong coupling in the case of non-resonant pumping; the polariton density at around k=0 is still way below the Mott density; and people have claimed to have strong coupling in a 3QW sample with much higher powers. To prove this, the blueshift was measured at every power by finding the mode using a resonant laser (Fig. 5.3). It can be seen that the blueshift changes linearly with changing

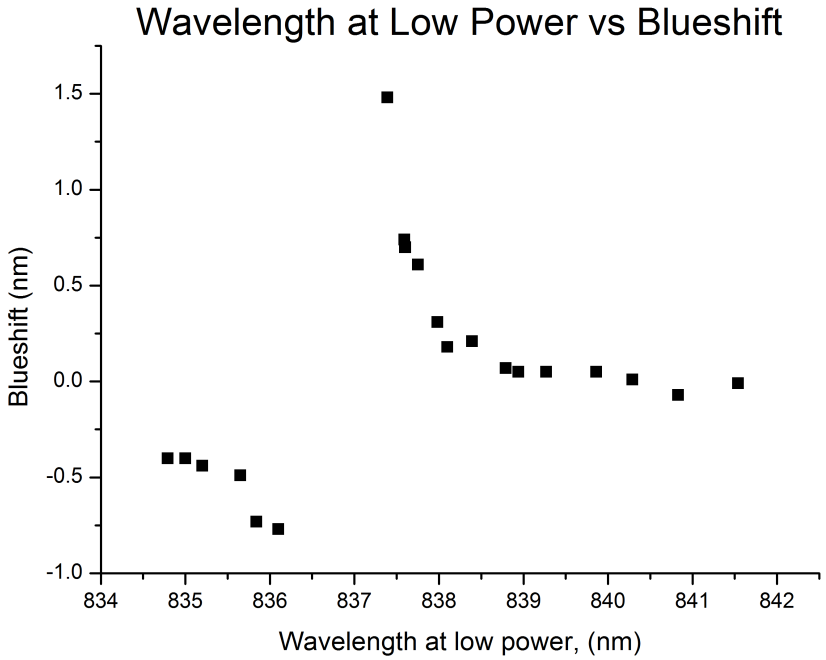

Figure 5.1: Blueshift measured for different low power excitation wavelengths. Negative blueshift is the same as redshift.

power, which suggests that the strong coupling regime has not been broken.

5.2.2 LG_{00} Mode Nonlinearity and Bistability

First, the blueshift at different wavelengths was measured using the previously mentioned method in order to know how the blueshift changes with changing wavelength and the best place to measure nonlinearity and bistability. A single QW sample was used for these measurements.

The nonlinearity measurement was performed according to the following steps: first, the mode wavelength was found at a very low power ($\sim 70\mu W$); second, the mode was located at a high power ($\sim 100mW$); then the laser excitation wavelength was moved between these two measured wavelengths and preceded by the power scan of the PL emission from $70\mu W$ to $100mW$. Fig. 5.2 shows a clear nonlinear increase in intensity, which starts at 40mW and stops at 60mW, because the mode blueshifted to the excitation laser wavelength and then it was

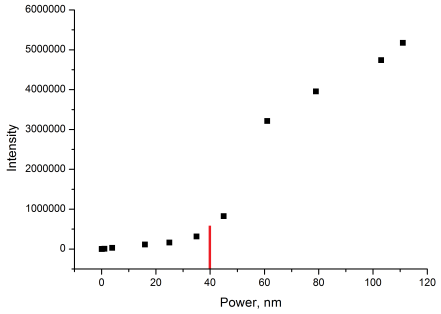

Figure 5.2: Sample emission intensity vs resonant excitation power. Red line marks a lasing threshold power.

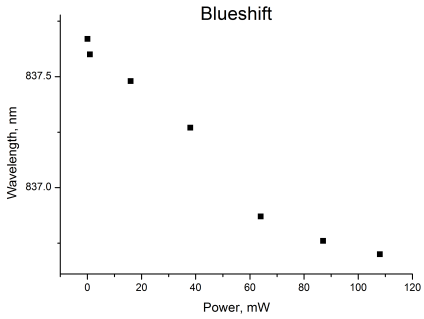

Figure 5.3: Sample emission blueshift vs resonant excitation power.

being pumped straight.

For this experiment, the excitation laser wavelength was set at a slightly lower wavelength, but within the range of the mode shift. In this case, the increasing laser power will create a greater density of polaritons, and the interaction between its exciton parts will increase the mode energy. This will move the mode into resonance with the excitation laser. This increases the power, which gets into the cavity even more. In the opposite situation, when the excitation laser power is reduced, the internal optical field is strong enough to keep the polariton mode closer to the excitation laser wavelength, when it would be expected in the case of increasing excitation laser power, until a threshold power, when this effect disappears. This effect is called bistability (Fig. 5.4), which requires the polariton linewidth to be smaller than the polariton mode shift. It was already observed not only in one-dimensional photonic crystals ([102]), microdisc resonators ([103]) and microring resonators ([104]), but also in microcavities in weak ([105]) and strong regimes ([106]). Optical bistability is the presence of two stable states of cavity transmission. These states are called "low" and "high". This effect was observed for the measured sample (Fig. 5.5), where bistability started at 3mW and ended at 40mW. The intensity increased more than 40 times in the bistability range.

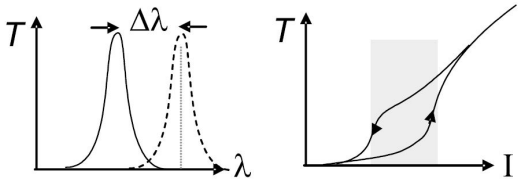

Figure 5.4: Theoretical measurement of bistability. A higher intensity is required when the intensity is increasing, compared to the threshold, when the intensity is decreasing.

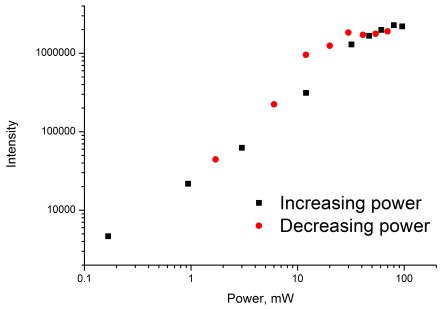

Figure 5.5: Sample emission intensity versus excitation power. Bistability observed from 3mW to 40mW of excitation power for a single QW sample.

5.2.3 LG_{01} Mode

Using resonant laser excitation and transmission mode, the spin-texture-like signal of zero-dimensional exciton-polaritons was observed. This was already observed using non-resonant laser excitation in reflectivity mode ([107]). An open-cavity structure enhances the transverse-electric-transverse-magnetic (TE-TM) splitting. In consequence, the quantized spin vortices are being carried by the polariton eigenstates. This TE-TM splitting can be tuned by changing the photonic-excitonic fractions of the exciton-polaritons.

The transmission experiment showed that depending on the resonant laser wavelength, it is possible to excite different profiles of the first transverse mode. This demonstrates a controllable way of a chosen splitted mode using a resonant laser. The observed real space PL intensities are very similar to the ones observed using the non-resonant laser ([107]). The lower energy mode has two lobes at $-45°$ angle, and the higher energy mode has two lobes at 0 degrees angle. These two modes overlap in between and have the shape of the circle (Fig. 5.6).

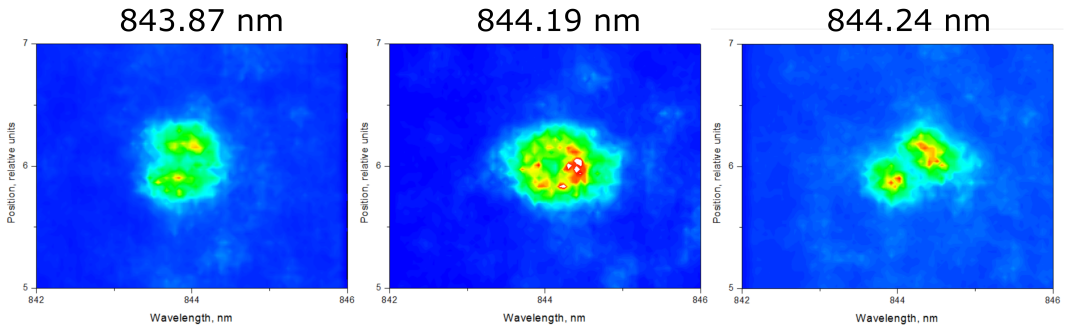

Figure 5.6: The images showing observed 1st transverse mode real space PL intensities. a) lower energy mode spectra, b) spectra between two split modes, c) higher energy mode spectra.

5.3 Measurements Made with New Transmission Cryostat

5.3.1 PL Emission Using Non-Resonant Laser

First, the system was tested using non-resonant laser excitation to make sure the transmission configuration gives the same results as using the reflectivity configuration (Fig. 5.7). No difference was noticed between the two transmission modes. This is a proof that the transmission setup is working correctly and can be used for other experiments.

5.3.2 Efficient Condensation

5.3.2.1 Experiment

The bottom sample used in the experiment is an $In_{0.04}GaAs$ single QW on a planar 28 pair AlAs/GaAs DBR grown using molecular beam epitaxy, and the top sample is concave DBR mirrors with 15 dielectric layers of SiO_2/Ta_2O_5 deposited on a concave surface. The 20μm RoC concave feature was used during the experiment. A GaAs active region has a size of $3\lambda/2$. A 10nm single $In_{0.4}Ga_{0.96}As$ QW is placed where simulations showed an expected electric field antinode. It gives a Rabi splitting of 3.4meV, an exciton emission at 837.3nm and a Q-factor of 20,000.

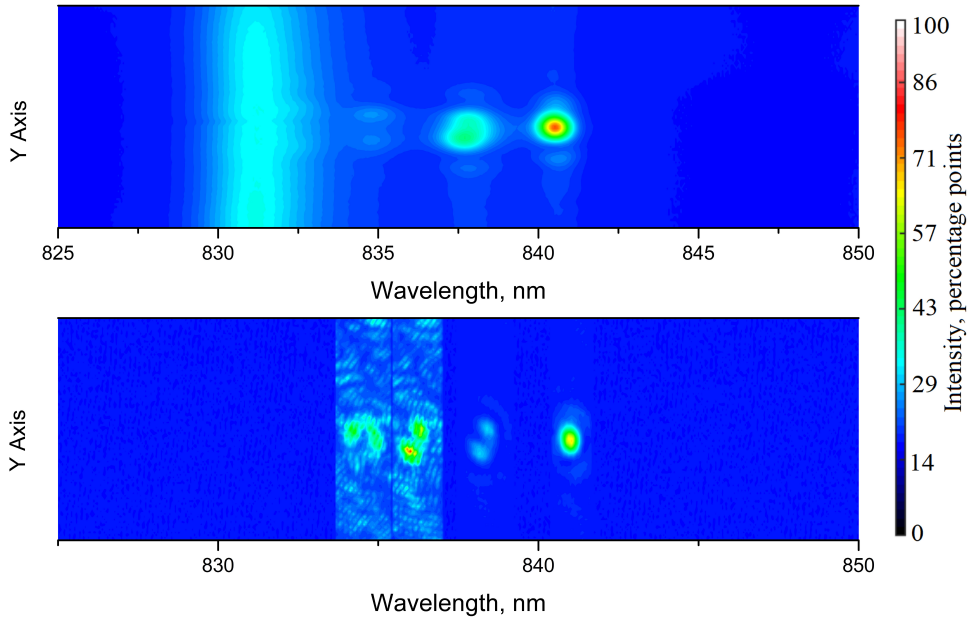

Figure 5.7: PL emission modes in transmission cryostat using non-resonant excitation laser (on the top) and the corresponding PL modes using resonant excitation laser (on the bottom). The transmission modes in the bottom image were taken from four separate measurements. The mode shift to a higher wavelength is visible for a resonant excitation.

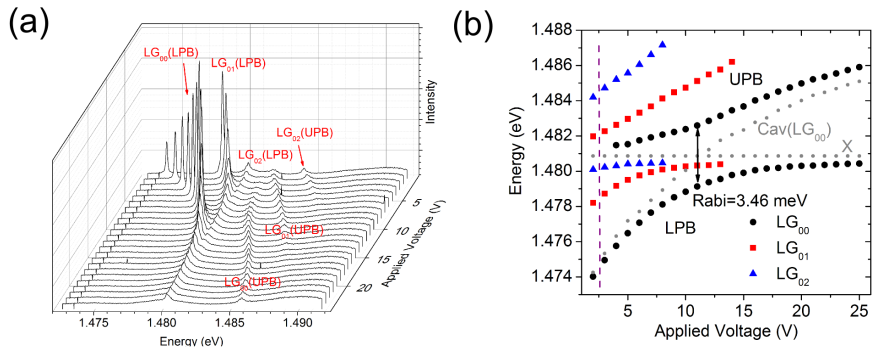

Figure 5.8: Anticrossing scans. a) Series of spectra taken at different cavity lengths by applying voltage on the piezo stage. b) Emission peaks extracted from (a) showing LG_{00}, LG_{01} and LG_{02} mode energies' dependence on voltage applied to the piezo stage. Anticrossing was observed for all the mentioned modes. The grey dotted line represents the LG_{00} bare exciton (X) and cavity (Cav) modes.

First, an anticrossing scan was performed to prove a strong coupling regime, which was observed for LG_{00}, LG_{01} and LG_{02} modes (Fig. 5.8). The measured Rabi splitting was found to be 3.46meV. This was done using continuous non-resonant red laser excitation (635nm) and by varying the cavity length through the application of piezo voltage.

To prepare for the experiment, the microcavity was tuned at a detuning of -0.23meV for LG_{01} mode and -5.52meV for LG_{00} mode. This configuration is marked in Fig. 5.8b by the purple dashed line. Then the energy of the continuous and vertically polarised Ti:Sapphire laser was set to be 0.54meV above the LG_{01} mode in all cases, which creates a quasi-resonant pumping.

Finally, two measurements were taken, collecting either vertical or horizontal polarisation emission. The signal was collected from the other side of the excitation. All the results of LG_{00}, LG_{01} modes (before and after the threshold) and the total intensity of both modes are visible in Fig. 5.9. The pumped mode (first transverse polariton mode excited resonantly by the laser) dominates the spectra below the threshold, and the LG_{00} mode cannot be distinguished from the noise. In the case of the horizontal polarisation, the collection (cross-polarised with the excitation laser) LG_{01} mode can be observed (Fig. 5.9d), which blueshifts to the

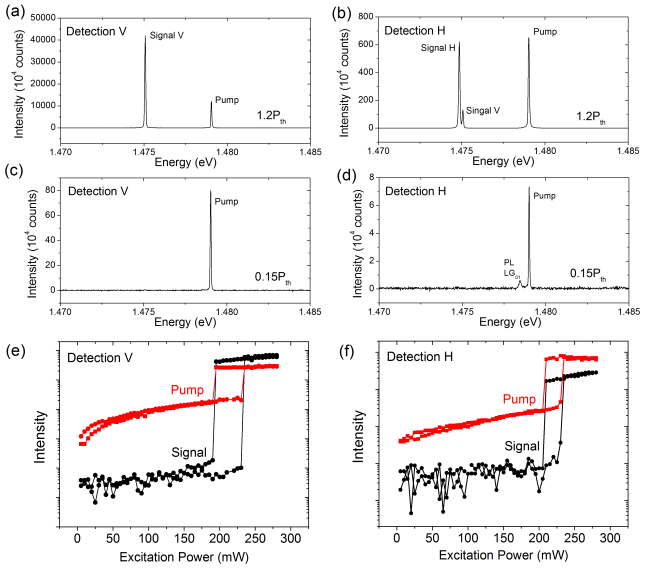

Figure 5.9: a-d) PL emission spectra of the pumped and the signal modes above (a and b) and below (c and d) the nonlinear threshold. The vertical linear polarisation pump laser was used in all the cases. The collection polarisation was different; vertical linear polarisation was detected in a) and c), whereas horizontal linear polarisation was detected in b) and d). e) and f) present power scans of the pump and the signal modes with an observed bistability effect. The e) signal was collected in vertical polarisation and f) was collected in horizontal polarisation.

wavelength of the laser (Fig. 5.9b).

Also above the threshold, both modes (LG_{00} and LG_{01}) become comparable in intensity, indicating the very efficient polariton transfer from the pump to the signal mode (longitudinal polariton mode). The signal mode is split into two cross-linearly polarised modes (separated by 0.2meV), because of the small ellipticity of the concave mirror and the birefringence of the materials. The nonlinearity of the vertically polarised LG_{00} mode is bigger, which makes it dominant (Fig. 5.9). Despite the same threshold between the LG_{00} and LG_{01} modes, the signal mode nonlinear increase is much stronger and reaches 4 orders of magnitude, highlighting the nonlinear enhancement of the polariton scattering rate at threshold. Finally, the optical bistability was observed for collection of both horizontal and vertical polarisations (Fig. 5.9e and f).

Both modes were investigated above the threshold using real-space imaging in both horizontal and vertical polarisations (Fig. 5.10). The LG_{00} mode shape represents a Gaussian profile, whereas the LG_{01} mode has a double-lobed profile due to the spectral splitting and is described by the Hermite-Gausssian (HG) mode profile.

The data from Fig. 5.10 shows a never-before-observed scattering efficiency of 0.59, which was calculated using Eq.5.1. The emission power above the threshold for vertical polarisation was measured to be 1.15μW. The polariton number was estimated by calculating the energy of polaritons using the polariton lifetime given by $\tau = \frac{Q\lambda}{c}$. It was calculated to give 146 polaritons in the system, 48 of them in LG_{00} and 98 in LG_{01} mode. The LG_{01} mode blueshifted by 200μeV, giving a polariton-polariton interaction energy of 4μeV, which is a good estimate, but it does not include the interaction with excitons. This shows a strong polariton interaction due to the tight confinement of the open-cavity system.

$$\eta = \frac{[I_{LG_{00}}(V) + I_{LG_{00}}(H)]/|C_{ph,s}|^2}{[I_{LG_{01}}(V) + I_{LG_{01}}(H)]/|C_{ph,p}|^2 + I_{LG_{00}}(V) + I_{LG_{00}}(H)]/|C_{ph,s}|^2} \tag{5.1}$$

Where $I_{s/p}(V/H)$ is the integrated intensity of the signal/pumped mode detected in Vertical/Horizontal linear polarizations and $C_{ph,s/p}$ is the photonic Hopfield coefficient of the signal/pumped modes.

5.3.2.2 Simulation

Simulation was performed by Emiliano Cancellieri to check if polariton scattering stimulated by the OPO process can account for achieved results. In this case the open cavity system was modelled with a generalized Gross-Pitaevskii equation (GP) ([108], [109]) for coupled cavity exciton fields (ψ_C and ψ_X) and include the effect of decay and resonant pumping ($\hbar = 1$):

$$\partial_t \begin{pmatrix} \psi_X \\ \psi_C \end{pmatrix} = \left[H_0 + \begin{pmatrix} g_X|\psi_X|^2 & 0 \\ 0 & V_C \end{pmatrix} \right] \begin{pmatrix} \psi_X \\ \psi_C \end{pmatrix} + \begin{pmatrix} 0 \\ F \end{pmatrix},$$

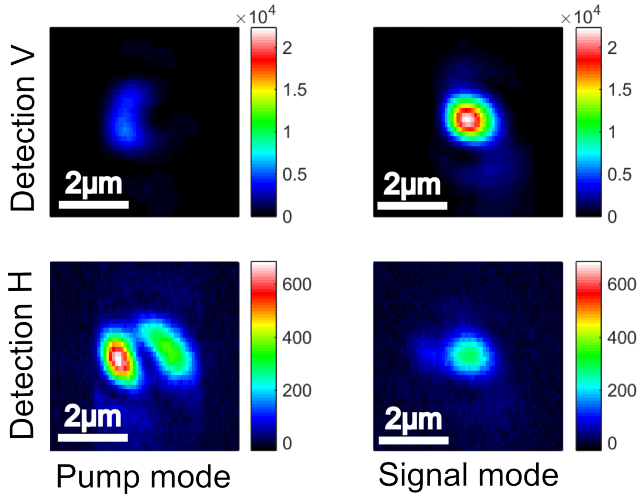

Figure 5.10: Here are presented real space images of the pumped and the signal modes above the nonlinear threshold. Both modes were detected in vertical and horizontal linear polarizations.

where the term H_0 is the single particle Hamiltonian:

$$\begin{pmatrix} \omega_X(-i\nabla) - i\kappa_X/2 & \Omega_R/2 \\ \Omega_R/2 & \omega_C(-i\nabla) - i\kappa_c/2 \end{pmatrix},$$

and $\omega_C(-i\nabla) = \omega_C^0 - \nabla^2/2m_c$ is the cavity dispersion with a photon mass $m_C = 2.3 \times 10^{-5} m_0$, where m_0 is the bare electron mass. For the simulations the flat exciton dispersion was set to zero $\omega_X(-i\nabla) = \omega_x^0 = 0$, and the exciton photon detuning was also fixed $\delta_{ex-ph} = \omega_X^0 - \omega_C^0 = -11\ meV$. The parameters of the Rabi frequency and the exciton and photon decay rates were used as following: $\Omega_R = 3.5\ meV$, $\kappa_X = 0.20\ meV$, and $\kappa_C = 0.05\ meV$. A continuous-wave quasi-resonant pump was used for the simulation of the polariton injection in to the sample. The laser shape was used to be a Gaussian shape: $F = f_p e^{-i\omega_p - (r-r_0)^2/2\sigma_p^2}$, where ω_p varies from -1.9 to $-1.8\ meV$. Here $r_0 = 0.5\ \mu m$ represents a slight mismatch between the pump and potential centres, and also $\sigma_p = 2.5\ \mu m$. Also a harmonic confinement of the photonic component was introduced to simulate the curvature of the top mirror: $V_C = \frac{1}{2} m_C \omega_{hp}^2 r^2$, where $\omega_{hp} = 5.0\ meV$ is the strength of the harmonic confinement. For the more precise results, all the parameters used in the simulation were chosen to be similar to the experimental values. Finally, a Runge-Kutta algorithm was used to simulate the dynamics of

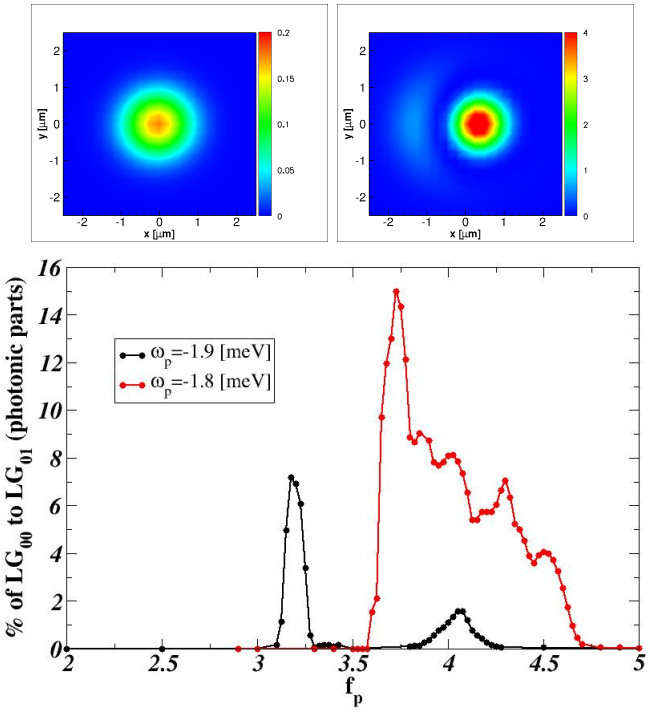

Figure 5.11: Top figures: emission intensity for the $LG00$ (left) and $LG01$ (right) modes at the steady state for $\omega_p = -1.8\ meV$ and $fp = 3.750$. Lower panel: percentage of photon emission at the LG_{00} energy with respect to the emission at the LG_{01} energy as a function of the pump intensity. The two curves correspond to two different frequencies for the quasi-resonant continuous-wave pump.

the GP equation. Simulation steps were as following: it was started from an empty system, then the pump was turned ON and a steady state situation was reached. At this point the spectra was evaluated of the emitted light and the ratio was derived between the population at the LG_{00} energy and the population at the LG_{01} energy (Fig. 5.11).

5.3.2.3 Conclusion

The simulated OPO efficiency is in the order of $10-15\%$ (Fig. 5.11 lower panel) for the photonic component (which correspond to an even smaller efficiency if we compare the polariton populations, since the LG_{00} mode is more photonic than the LG_{01} mode), which is much less than the overall conversion efficiency

observed experimentally. Nevertheless, the whole process can be explained by the combined effects of OPO and incoherent relaxation. Although the excited mode is only around 50% excitonic-like, it overlaps with localized exciton levels due to the small Rabi splitting associated with the single quantum well. During the OPO process, the pumping laser simultaneously excites the localized exciton states that afterwards populate a cold exciton reservoir. The exciton then experiences fast relaxation due to stimulated scattering by the polaritons that reach the LG_{00} via the OPO process ([110], [111]). It is important to note that the polariton blueshift is much lower than would be required to reach the bare cavity mode. This shows that efficient occupation of the ground state is in the strong coupling regime, which has been rarely realized under non-resonant excitation in microcavities with a single quantum well.

As the polariton transfer from LG_{01} to LG_{00} mode is very efficient, the coupling of the external pumping laser into the cavity is not that efficient. It could be improved if the laser profile matched the LG_{01} mode profile by using a spatial light modulator.

5.3.3 Bistability investigation

First, optical bistability is incredibly interesting, because it is a feature of non-linear optical effects. It provides another method of light by light manipulation, in which two stable excited states are observed for a single input intensity ([112]). This effect may allow the development of all-optical switching, optical transistors and optical memory ([113], [114]). Further investigation of the bistability at various detunings showed that the bistability threshold and size can be varied (Fig. 5.12). For example, the effect threshold power was observed in the range from 105mW to 263mW. The recorded bistability size also varied from 20mW to 71mW, which is a 3.5 times difference between the minimal and the maximal values. This so-called region of hysteresis is defined by the ratio between the pump detuning and the free space spontaneous emission rate. These measurements gave an impressive bistability percentage of 27%, which is determined by calculating the bistability size percentage compared with threshold value.

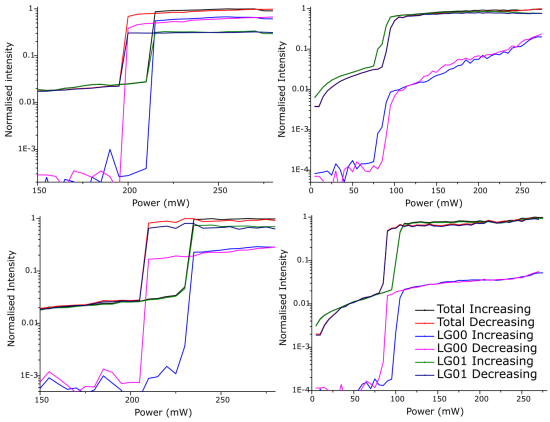

Figure 5.12: Normalised sample emission intensities versus excitation laser power. Bistability measurement graphs at various detunings. The vertical polarisation emission is shown in the top row, and the horizontal polarisation in the bottom row.

5.3.4 Conclusion

The results in this chapter show that the two transmission setups work very well, and different effects using resonant laser were observed: a nonlinear intensity increase and a bistability. It was shown that it is also possible to achieve a very efficient polariton scattering. It is expected that such an efficient polariton transfer appears because of a several mixed effects: the strong three-dimensional confinement, the stimulated parametric scattering and the condensation from a cold exciton reservoir. A compact system with a high scattering efficiency might be used for integrated optical circuit applications and the realization of quantum polaritonic systems.

Chapter 6

Open-Cavity Experiments

6.1 Organic Material

Interest is growing in the field of strongly coupled organic semiconductors as they have very high Rabi splitting (between 50meV and 1000meV), a large oscillator strength and large exciton binding energies. Such properties would allow the observation of polaritons even at room temperature as Rabi splitting exceeds thermal energy. Another advantage of organic materials is their easy fabrication. They are usually simply spin coated onto the required DBR mirror, which does not cause lattice mismatch. Polariton lasing and polariton condensation have already been observed. In these materials, excitons tend to be very small, mostly located on the same molecule, and so they are called Frenkel excitons.

There are two goals for trying organic materials in an open-cavity device. First, it is important to show that an organic material can work inside of the open-cavity device, which would mean that various experiments could be performed using it. Second, it is important to show Amplified Spontaneous Emission (ASE), which is a process when light is optically amplified by a stimulated emission in the gain medium. During this process, the amplification occurs close to the peak of the optical gain. A pulsed laser is required for this as there is a slow conversion of singlet states into long-lived triplet states that depletes the ground state and prevents it from reaching population inversion. Triplet population decay requires

the laser to work at a frequency of 1kHz.

J aggregate, the fluorescent molecular dye BODIPY-Br (bromine-substituted boron-dipyrromethene), was used to check if an open cavity is suitable for organic material investigation. This material has an emission at 550nm, an exciton at 530nm and a Rabi splitting of 50-100meV (it increases with an increasing dye concentration, but is definitely greater than kT).

In preparation for the experiment, BODIPY-Br was spin coated onto a $10mm \times 10mm$ dielectric DBR with a stopband at 550nm. The top mirror was the same plane dielectric DBR with a slightly smaller size of $5mm \times 5mm$. This introduced alignment difficulty as previously used top mirrors had a plinth of 500μm$\times 500\mu$m. Larger mirrors cause larger minimum cavity lengths as the edge touching at a small angle corresponds to long cavity lengths in the place where it is measured. Because of a very different working wavelength, the system itself was modified by changing all B-coated (allowing transmission of 650-1050nm waves) achromatic doublet lenses in the system into A-coated lenses (allowing transmission of 400-700nm waves). All the golden mirrors were also changed into silver mirrors because of a better reflectivity at the desired wavelength. The last step was to change the laser into a continuous-wave 520nm green laser.

The measurements proved that an open-cavity device can be used to study polymers. First, many k-space modes were observed at great cavity lengths (Fig. 6.1), and it was possible to reduce the number of modes to one, which means the cavity became very thin. These modes were also clearly observed in the reflectivity spectra. The Q-factor was measured as high as 900 at long and around 450 at small cavity lengths. A greater Q-factor at longer cavity lengths is consistent with the results from previous experiments. Organic materials tend to have a low quality factor in comparison to semiconductor QWs. In this case, no special vibration control measures were taken to reduce stability issues as the Q-factor is too low to be an important influence. Unfortunately, an anticrossing scan did not show polariton formation, and the modes bend only because the samples start touching (Fig. 6.2), which was done at room temperature. In addition, UPB was

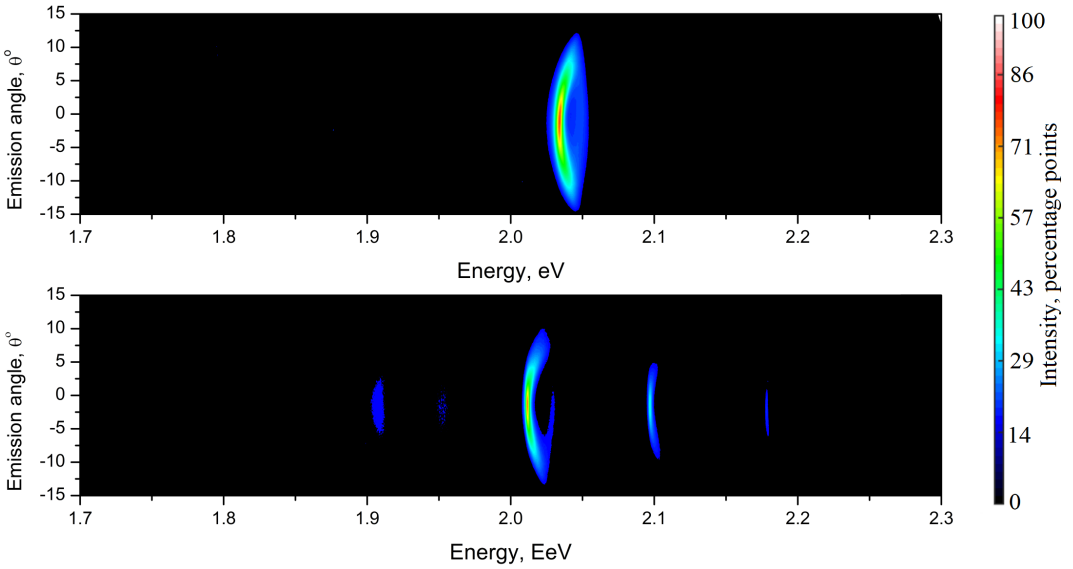

Figure 6.1: Sample emission intensity in emission angle-energy space. Top image shows only one mode in the observed spectra, which means that the cavity length is small. The spectra below show many modes and prove a large cavity length.

too weak for observation.

Unfortunately, the ASE effect was not observed during measurements. To get this effect and for better results during other experiments, the following steps should be taken. First, a top mirror with a 500μm$\times500\mu$m plinth and concave features should be fabricated with a stopband at 550nm wavelength. This would allow an easier alignment of the system, making experiments faster and easier, as well as mode confinement in two dimensions. The bottom mirror should also be redesigned to have a maximum electric field inside organic material and not at the interface between the material and the mirror. Second, a pulsed 1kHz laser should be used instead of the continuous-wave laser, which was not available during this experiment. It also appears that greater angle collection is required as it is currently -14 degree to 14 degree and does not make visible all dispersion features in k-space mode.

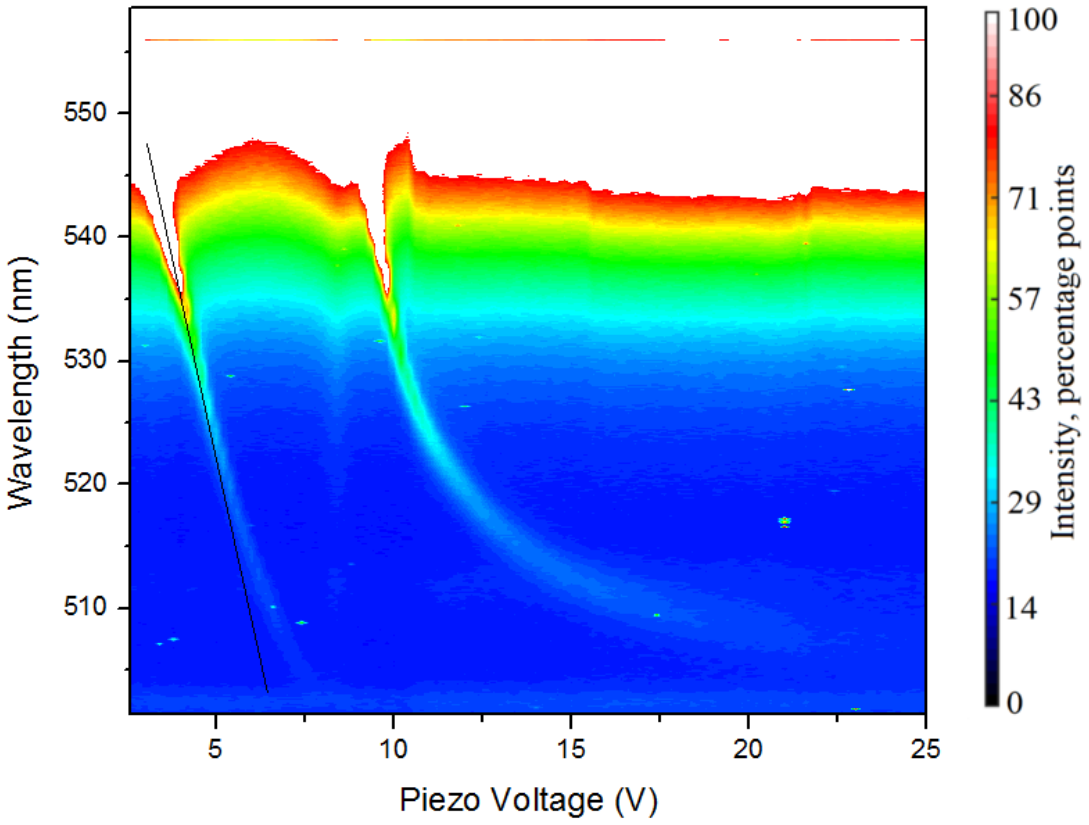

Figure 6.2: Sample emission into wavelength-piezo voltage/relative cavity mode space. Anticrossing scan did not show anticrossing for BODIPY-Br in an open-cavity device at 530nm. The modes bend because the samples start to touch. The measurement was performed at room temperature.

The experiment was discontinued, because of the very weak signal caused by the low light collection efficiency of CCD camera at a green wavelength, which increases the required integration time to an unacceptable level. This makes the alignment of the plane mirrors of the system to be very difficult and slow, almost to the point of impossibility. BODIPY-Br requires grating with a different blaze wavelength or a different grating that would be more efficient at the emitting wavelengths. The current 1μm blaze 600g/mm grating's efficiency rapidly drops from 50% at 700nm to 10% at 550nm. There is also a possibility that the sample degraded in the air or was burnt by a powerful laser.

6.2 Q-Factor Dependence on a Sample Structure

The cavity Q-factor depends on four main properties: exciton linewidth, cavity reflectivity, system stability and laser power. Exciton linewidth is an intrinsic property and cannot be improved after growth. Different samples have to be grown and tested in order to find ways to improve linewidth. The second property, cavity reflectivity, depends on DBR layers. The more layers, the better the reflectivity and thus the better Q-factor. System stability is unique to an open cavity as the two DBRs are not connected with each other by a semiconductor layer. This means that the two mirrors vibrate independently and so the cavity length changes. The polariton mode moves between different wavelengths, and with a slow acquisition time, these peaks combine into one broader peak. This arrangement makes system very vulnerable to outside noise. The last main property is laser power. Increasing laser power pumps more excitons into the system, which increases their polariton screening and widens the linewidth. The polariton linewidth increase with laser power should have little effect using the resonant laser, which is required for the polariton blockade experiment because it does not create an exciton reservoir.

At the moment, improvements to both polariton linewidth (depends on exciton linewidth and cavity reflectivity) and system stability are being investigated. It

is important to know the intrinsic polariton linewidth to determine how much the system is influenced by system vibrations and the laser power. This could help to determine what is the current biggest limiting factor of the system. It is also important to know how DBR and QW structural changes influence the intrinsic polariton linewidth.

As can be seen from Fig. 6.3, by changing both samples, a Q-factor increase of more than 4 times was achieved. The measurements were always performed in a very silent environment, using a low-power laser and a short acquisition time. The current improvement was achieved by increasing the number of DBR layers, which means an increase in the DBR reflectivity. One 15nm GaAs QW sample allowed the observation of a never-previously-measured exciton linewidth of $250\mu eV$, but when it was grown on the DBR, the trion emission became very strong. Other very promising half-cavity samples were tested, but they usually had a strong trion at lower energy. Unsuccessful methods were tried to grow an alloy barrier to stop these excitons. In the end, it was decided to keep the QW structure the same as in W0968, but increase the number of DBR layers in the W1222 sample. This increased the observable Q-factor from 8000 to 12000. Use of the new top dielectric DBR made by Layertec with more DBR layers increased the Q-factor further to 33000. Unfortunately, for reasons unknown, the Rabi splitting became 1.4meV instead of the previous 3.4meV. This makes the sample not very useful for polariton experiments. Efforts are being made to find the cause and resolve the issue.

The sample structures used are as follows. The W0968 sample is a single 4% InGaAs QW grown on 27 pairs of GaAs and AlAs layers with a layer pair thickness of 129nm. W1222 has the same cavity structure. It is a single 4% InGaAs QW grown on 32 pairs of $Al_{0.2}Ga_{0.8}As$ and AlAs layers with 132nm layer pair thickness. W0968, W1222 and other measured-but-not-mentioned bottom semiconductor samples were grown at the University of Cambridge. The LaserOptic top dielectric mirror has concave mirror features covered with 10 SiO_2/TiO_2 layers with a stopband at 825nm. The LayerTec sample is concave mirror features covered with 14 layers of SiO_2/Ta_2O_5 with a stopband at 840nm. Both top di-

	LaserOptik (old)	Layertec (New)
W0968 (old)	8,000	----
W1222 (New)	12,000	33,000

Figure 6.3: Table showing the Q-factor change with changing top and bottom DBRs measured in the same setup. Two different top mirrors (coated by Laser Optik and Lasertec) and two different single QW bottom DBRs (W0968 and W1222) were used.

electric mirrors were fabricated at the University of Oxford using the focused ion beam method and coated by an external company.

6.3 $MoSe_2$ Monolayer

The $MoSe_2$ monolayer was placed in the open cavity (Fig. 6.4). This is the only system in which monolayers could be investigated using a resonant laser in the open-cavity system. This system makes nonlinearity or OPO condensation observable. Important first steps were proven for the feasibility of these experiments, and it was a good test bed for future experiments. The flake was mechanically exfoliated on the substrate.

This sample was mounted using the same method as the other samples. The only difference is that it was mounted on the sample holder attached to a piezo stack, whereas the top mirror was attached to the stationary sample holder. It was possible to identify the monolayer and observe its emission signal, but attempts to put it into the cavity failed. At the moment, the flake was shattered by pressing two mirrors together, and the emission from the flake in the cavity was not observed.

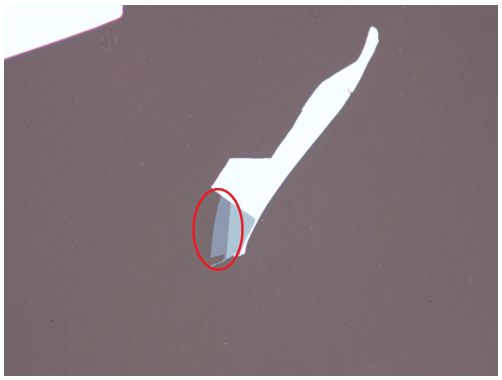

Figure 6.4: $MoSe_2$ monolayer flake circled in red.

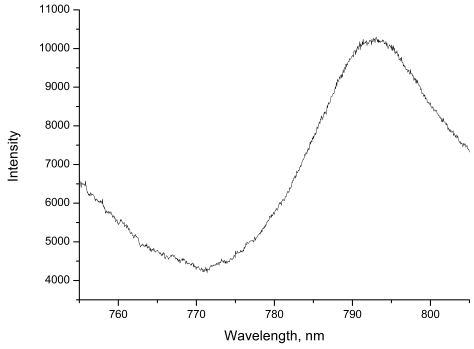

Figure 6.5: Sample emission intensity versus wavelength. Monolayer emission signal using non-resonant laser excitation. The spectral shoulder on the left comes from a non-resonant excitation laser.

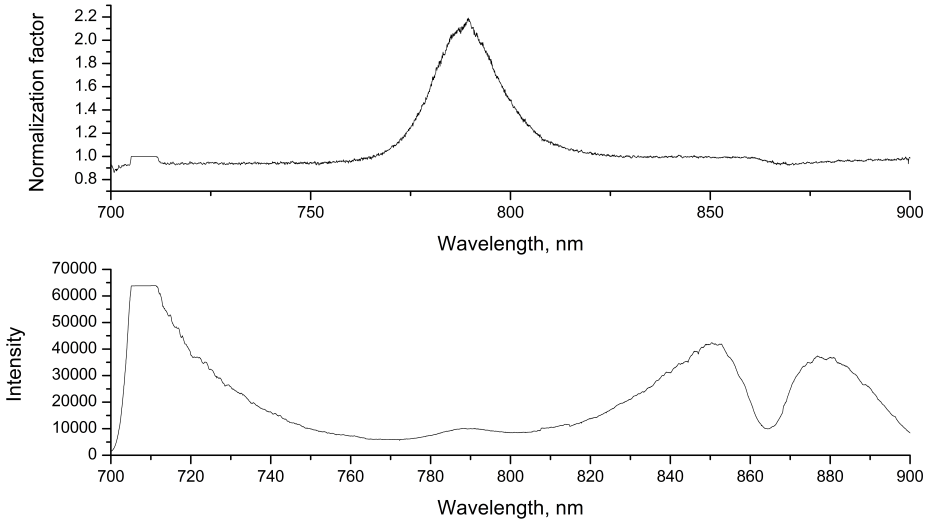

Figure 6.6: Top - flake emission after spectra normalisation using a white light source. Bottom - flake emission with a white light signal.

Chapter 7

Future Experiments

7.1 Introduction

This chapter will cover the background of experiments that will be attempted in the open-cavity system in the future. It includes surface acoustic waves on the bottom sample, a lift-off method to transfer quantum wells and the spin manipulation of polaritons to realise multiple bits in the single system.

7.2 SAW in an open cavity

In preparation for the SAW experiment, the parts required to upgrade the setup were already designed and made. Two extra wires must go through the vacuum tube to reach sample area in order to control the SAW device. A test setup was also created and LabVIEW code written to check the actual working frequency of the interdigital transducers (IDTs) on the sample, which would be used to create surface acoustic waves (SAWs) in an open-cavity system. These adjustments improved on the previous experiment, in which IDTs were deposited on top of the full cavity and the penetration into quantum wells was much worse. The test setup is also going to be useful to check if connections were properly made and the final system is ready for the SAW experiment.

The LabVIEW code was scanning through the range of generated frequencies, because a reduction of intensity at the working frequency should be observed if IDTs work properly; this creates a dip in the final frequency-scan spectra. During the measurements of the received sample, a dip was not observed. This absence led to an inspection of the sample, which was found to be damaged. A repaired sample should be received soon, and the experiment will continue to measure the dip in reflectivity. The setup used consists of a signal generator, an analyser and a signal splitter. The signal coming from the signal generator is directed to the sample by the splitter. Then the signal reflects back, and this time, instead of going back to the signal generator, it is directed to the analyser by the same splitter. At first, a test setup was used to investigate transmission and reflection from various ports to know the characteristics of the splitter that will be used in the main experiment.

7.3 Lift-Off Experiment

An epitaxial lift-off procedure was also tested and should be continued in the future. This method should allow the "peeling off" of a semiconductor layer, containing quantum wells, from a semiconductor mirror in order to deposit them on a dielectric mirror. It was already successfully achieved and published in the Journal of Applied Physics ([115]). Repeating the experiment would allow having good-quality quantum wells on a mirror with better reflectivity characteristics. At the moment, the strain mismatch causes poorer-quality quantum wells on better-reflectivity dielectric mirrors compared to semiconductor mirrors.

Here is a list of processes followed in the epitaxial lift-off procedure in order (Fig. 7.1). 1) Wax is heated and deposited on the sample to create a pillar after etching. 2) Piranha solution is used to etch the sample and uncover quantum well layers in order to expose GaAs layers, which will be etched to separate QWs. 3) Sample is attached to the Teflon rod through the deposited wax. 4) HF is used to etch through the GaAs layer and separate QWs. 5) Quantum wells are deposited by pressing them on the new dielectric sample.

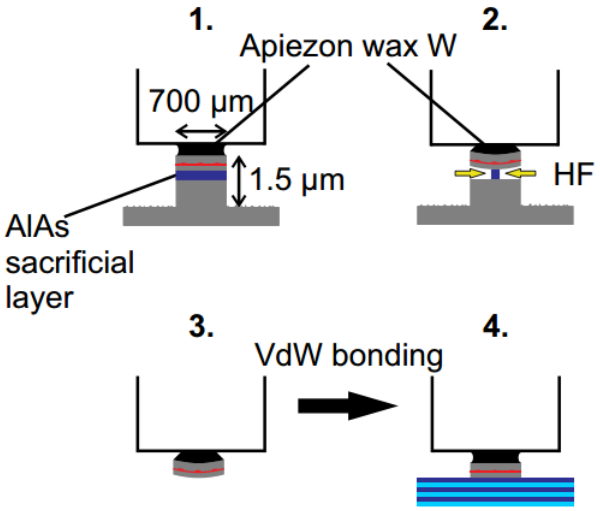

Figure 7.1: Figure taken from [115]. The lift-off procedure is shown step by step after a successful pillar etch. This method creates 700μm-diameter QW layer. 1) Result after Piranha solution etching. 2) HF acid etching. 3) QW transfer. 4) QW deposition on the new surface.

This experiment was already attempted multiple times, but because of a time shortage and the need for very strong HF acid, it was impossible to try to improve the unsuccessful experiment. The greatest problem arose during the QW transfer onto a dielectric mirror. The QW did not stick onto the dielectric mirror and was left on the Teflon tube. The current deposition technique should be mastered or another technique should be tried in future attempts.

7.4 Spin Manipulation

Currently, there are attempts to maximise classical and quantum information processing capabilities by using structured light beams with orbital angular momentum (OAM) and the polarisation of light. [116] suggests a way to use both of these degrees of freedom in combination by using strong light-matter coupling, TE-TM splitting and circular-symmetry confinement. The formation of polaritons has advantages, in that they can be manipulated on an ultrafast scale because of their light component and that they can be controlled because of their matter

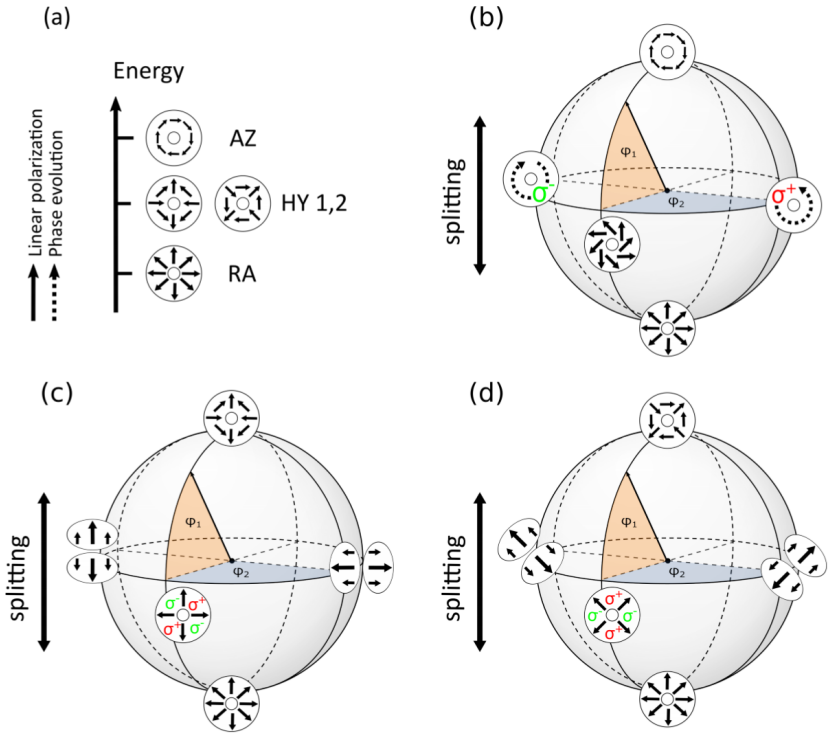

Figure 7.2: Figure taken from [116]. A diagram presenting polariton states. (a) eigenenergies and eigenmodes arising in the presence of 2D harmonic confinement and TE-TM splitting. (b-d): SO-Poincare spheres resulting from the states: ψ_{RA} and ψ_{AZ} (b), ψ_{RA} and ψ_{HY1} (c), and ψ_{RA} and ψ_{HY2} (d). The angular coordinates are ϕ_1 and ϕ_2.

component. The AC Stark effect allows this through control of the excitation energy of photon emitters without modifying the population.

In [116], it was theoretically shown that polariton spin vortices can be efficiently manipulated by using red-detuned Stark pulses of a different polarization. This manipulation is based on the evolution of the spin-orbit vector space. The mentioned model opens the door to manipulation of multiple logical bits inside of the single physical state. An open-cavity device is a perfect and only system, which allows observing the polariton states of the spin-orbit hypersphere as proclaimed, and these experiments should be carried out in the future.

7.5 Conclusion

Open-cavity systems developed throughout the work of this thesis are perfect test beds for many future theories and experiments. This approach has great potential in resonant excitation, monolayer, spin-orbit vector space measurements and offers the possibility of achieving a single photon source by using either coupled concave mirrors or surface acoustic waves.

References

[1] K. Vahala, "Optical microcavities," *Nature*, vol. 424, pp. 839–846, 2003. iv, 28

[2] F. Martini, G. Innocenti, R. Jacobovitz, and P. Mataloni, "Anomalous spontaneous emission time in a microscopic optical cavity," *Physical Review Letters*, vol. 59, pp. 2955–2958, 1987. iv

[3] M. Trupke, E. A. Hinds, S. Eriksson, *et al.*, "Microfabricated high-finesse optical cavity with open access and small volume," *Applied Physics Letters*, vol. 87, p. 211106, 2005. iv

[4] P. Walker, L. Tinkler, M. Durska, D. Whittaker, *et al.*, "Exciton polaritons in semiconductor waveguides," *Applied Physics Letters*, vol. 102, p. 012109, 2013. iv

[5] J. Singh, *Optical properties of condensed matter and applications*. Wiley, 2006. 2, 4

[6] C. Klingshirn, B. Meyer, A. Waag, A. Hoffmann, and J. Geurts, *Zinc oxide: from fundamental properites towards novel applications*. Springer, 2010. 2

[7] E. Purcell, "Resonance absorption by nuclear magnetic moments in a solid," *Physical Review*, vol. 69, p. 37, 1946. 3, 10

[8] P. Goy, J. Raimond, M. Gross, and S. Haroche, "Observation of cavity-enhanced single-atom spontaneous emission," *Physical Review Letters*, vol. 50, p. 1903, 1983. 3

[9] R. Hulet, E. Hilfer, and D. Kleppner, "Inhibited spontaneous emission by a Rydberg atom," *Physical Review Letters*, vol. 55, p. 2137, 1985. 3

[10] K. Guda, *The effect of interactions of intrinsic properties of polariton condensates in semiconductor microcavities*. PhD thesis, University of Sheffield, 2012. 4, 15, 20, 21, 24

[11] G. Panzarini, L. Andreani, A. Armitage, D. Baxter, *et al.*, "Exciton-light coupling in single and coupled semiconductor microcavities: Polariton dispersion and polarization splitting," *Physical Review B*, vol. 59, p. 5082, 1999. 5

[12] "Representation of TE and TM modes." https://www.testandmeasurementtips.com/basics-of-tem-te-and-tm-propagation/. Accessed: 2018-03-27. 6

[13] R. Barbour, *A tunable microcavity for semiconductor quantum dots*. PhD thesis, Heriot-Watt University, 2009. 7, 10, 12

[14] G. Khitrova, H. Gibbs, F. Jahnke, M. Kira, and S. Koch, "Nonlinear optics of normal-mode-coupling semiconductor microcavities," *Reviews of Modern Physics*, vol. 71, p. 1591, 1999. 7, 33

[15] T. Steinmetz, Y. Colombe, D. Hunger, T. Hansch, A. Balocchi, R. Warburton, and J. Reichel, "Stable fiber-based Fabry-Perot cavity," *Applied Physics Letters*, vol. 89, p. 111110, 2006. 8, 33

[16] A. Muller, E. Flagg, M. Metcalfe, J. Lawall, and G. Solomon, "Coupling an epitaxial quantum dot to a fiber-based external-mirror microcavity," *Applied Physics Letters*, vol. 95, pp. 329–339, 2009. 8, 27, 51

[17] A. Kavokin, J. Baumberg, G. Malpuech, and F. Laussy, *Microcavities*. Oxford: Oxford University Press, 2007. 9, 13, 15, 16, 20, 26, 49, 67, 72, 90, 103

[18] R. Barbour, P. Dalgarno, A. Curran, *et al.*, "A tunable microcavity," *Journal of Applied Physics*, vol. 110, p. 053107, 2011. 9, 14, 26, 33, 34

[19] P. Dolan, G. Hughes, F. Grazioso, B. Patton, and J. Smith, "Femtoliter tunable optical cavity arrays," *Optics Letters*, vol. 35, pp. 3556–3558, 2010. 9, 33

[20] Y. Yamamoto and R. Slusher, "Optical processes in microcavities," *Physics Today*, vol. 46, pp. 66–73, 2006. 10

[21] A. Muller, E. Flagg, J. Lawall, and G. Solomon, "Ultrahigh-finesse, low-mode-volume FabryPerot microcavity," *Optics Letters*, vol. 35, pp. 2293–2295, 2010. 10

[22] M. Fox, *Quantum optics: An introduction*. Oxford: Oxford University Press, 2006. 12

[23] M. Bayer, T. Reinecke, F. Weidner, A. Larionov, A. McDonald, and A. Forchel, "Inhibition and enhancement of the spontaneous emission of quantum dots in structured microresonators," *Physical Review Letters*, vol. 86, pp. 3168–3171, 2001. 12

[24] D. Bajoni, P. Senellart, E. Wertz, *et al.*, "Polariton laser using single micropillar GaAs-GaAlAs semiconductor cavities," *Physical Review B*, vol. 100, p. 047401, 2008. 12, 68

[25] T. Happ, I. Tartakovskii, V. Kulakovskii, J. Reithmaier, M. Kamp, and A. Forchel, "Enhanced light emission of $In_xGa_{1-x}As$ quantum dots in a two-dimensional photonic-crystal defect microcavity," *Physical Review B*, vol. 66, p. 041303, 2002. 12

[26] Y. Kaluzny, P. Goy, M. Gross, J. Raimond, and S. Haroche, "Observation of self-induced Rabi oscillations in two-level atoms eexcited inside a resonant cavity: The ringing regime of superradiance," *Physical Review Letters*, vol. 51, p. 1175, 1983. 12

[27] M. Skolnick, T. Fisher, and D. Whittaker, "Strong coupling phenomena in quantum microcavity structures," *Semiconductor Science and Technology*, vol. 13, pp. 645–669, 1998. 12

[28] V. Savona, L. Andreani, P. Schwendimann, and A. Quattropani, "Quantum well excitons in semiconductor microcavities: Unified treatment of weak and strong coupling regimes," *Solid State Communications*, vol. 93, pp. 733–739, 1995. 12

[29] L. Novotny, "Strong coupling, energy splitting, and level crossings: A classical perspective," *American Journal of Physics*, vol. 78, pp. 1199–1202, 2010. 13, 15

[30] M. Sich, *Effects of spin-dependent polariton-polariton interactions in semiconductor microcavities: Spin rings, bright spatial solitons and soliton patterns*. PhD thesis, University of Sheffield, 2013. 15, 17, 18, 22

[31] A. Reinhard, *Strong photon-photon interactions in solid state cavity QED*. PhD thesis, ETH Zurich, 2013. 16, 39

[32] H. Deng, H. Haug, and Y. Yamamoto, "Exciton-polariton Bose-Einstein condensation," *Reviews of Modern Physics*, vol. 82, p. 1489, 2010. 17, 79

[33] D. Whittaker, P. Kinsler, T. Fisher, *et al.*, "Motional narrowing in semiconductor microcavities," *Physical Review Letters*, vol. 77, p. 4792, 1996. 17, 39

[34] C. Weisbuch, M. Nishioka, A. Ishikawa, and Y. Arakawa, "Observation of the coupled exciton-photon mode splitting in a semiconductor quantum microcavity," *Physical Review Letters*, vol. 69, pp. 1062–1065, 1992. 17

[35] B. Dayan, A. Parkins, T. Aoki, E. Ostby, K. Vahala, and H. Kimble, "A photon turnstile dynamically regulated by one atom," *Science*, vol. 22, p. 5866, 2008. 17

[36] T. Liew and V. Savona, "Single photons from coupled quantum modes," *Physical Review Letters*, vol. 104, p. 183601, 2010. 17, 31

[37] S. Empedocles, D. Norris, and M. Bawendi, "Photoluminescence spectroscopy of single CdSe nanocrystallite quantum dots," *Physical Review Letters*, vol. 77, pp. 3873–3876, 1996. 18

[38] I. Favero, A. Berthelot, G. Cassabois, *et al.*, "Temperature dependence of the zero-phonon linewidth in quantum dots: An effect of the fluctuating environment," *Physical Review B*, vol. 75, p. 073308, 2007. 18

[39] S. Munch, S. Reitzenstein, P. Franeck, *et al.*, "The role of optical excitation power on the emission spectra of a strongly coupled quantum dot micropillar system," *Optics Express*, vol. 17, pp. 12821–12828, 2009. 18

[40] G. Rossbach, J. Levrat, A. Dussaigne, *et al.*, "Tailoring the light-matter coupling in anisotropic microcavities: Redistribution of oscillator strength in strained m-plane GaN/AlGaN quantum wells," *Physical Review B*, vol. 84, p. 115315, 2011. 18, 24

[41] K. Lagoudakis, *Physics of exciton-polariton condensates*. EFPL Press, 2013. 19

[42] E. Cerda-Mendez, D. Krizhanovskii, M. Wouters, R. Bradley, K. Biermann, *et al.*, "Polariton condensation in dynamic acoustic lattices," *Physical Review Letters*, vol. 105, p. 116402, 2010. 19, 28, 29, 39

[43] D. Fried, T. Killian, L. Willmann, *et al.*, "Bose-Einstein condensation of atomic hydrogen," *Physics Review Letters*, vol. 81, p. 3811, 1998. 20

[44] S. Christopoulos, G. Hogersthal, A. Grundy, *et al.*, "Room temperature polariton lasing in semiconductor microcavities," *Physical Review Letters*, vol. 98, p. 126405, 2007. 20

[45] A. Das, J. Heo, M. Jankowski, *et al.*, "Room temperature ultralow threshold GaN nanowire polariton laser," *Physical Review Letters*, vol. 107, p. 066405, 2011. 20

[46] L. Landau and E. Lifshitz, *Statistical physics vol. 5: Course of theoretical physics*. Butterworth-Heinemann, 1980. 20

[47] J. Kasprzak, M. Richard, S. Kundermann, *et al.*, "Bose-Einstein condensation of exciton polaritons," *Nature*, vol. 443, p. 409, 2006. 20, 24, 67, 103

[48] R. Balili, V. Hartwell, D. Snoke, L. Pfeiffer, and K. West, "Bose-Einstein condensation of microcavity polaritons in a trap," *Science*, vol. 316, pp. 1007–1010, 2007. 20

[49] J. Kasprzak, D. Solnyshkov, R. Andre, L. Dang, and G. Malpuech, "Formation of an exciton polariton condensate: Thermodynamic versus kinetic regimes," *Physical Review Letters*, vol. 101, p. 146404, 2008. 20, 104, 105

[50] W. Lai, N. Kim, S. Utsunomiya, *et al.*, "Coherent zero-state and π-state in an excitonpolariton condensate array," *Nature*, vol. 450, pp. 529–532, 2007. 20

[51] A. Love, D. Krizhanovskii, D. Whittaker, *et al.*, "Intrinsic decoherence mechanisms in the microcavity polariton condensate," *Physical Review Letters*, vol. 101, p. 067404, 2008. 21

[52] M. Abmann, F. Veit, M. Bayer, M. Poel, and J. Hvam, "Higher-order photon bunching in a semiconductor microcavity," *Science*, vol. 325, p. 5938, 2009. 21, 31

[53] A. Kavokin and G. Malpuech, *Cavity polaritons*. Academic Press, 2003. 21, 22

[54] F. Tassone, C. Piermarocchi, V. Savona, A. Quattropani, and P. Schwendimann, "Bottleneck effects in the relaxation and photoluminescence of microcavity polaritons," *Physical Review B*, vol. 56, pp. 7554–7563, 1997. 22, 24

[55] L. Ferrier and E. Wertz, "Interactions in confined polariton condensates," *Physical Review Letters*, vol. 106, p. 126401, 2011. 22, 26

[56] A. Tartakovskii, M. Emam-Ismail, R. Stevenson, *et al.*, "Relaxation bottleneck and its suppression in semiconductor microcavities," *Rapid Communications*, vol. 62, p. 2283, 2000. 24

[57] H. Miesner, D. Stamper-Kurn, M. Andrews, D. Durfee, S. Inouye, and W. Ketterle, "Bosonic stimulation in the formation of a Bose-Einstein condensate.," *Science*, vol. 279, pp. 1005–1007, 1998. 24

[58] S. Utsunomiya, L. Tian, G. Roumpos, *et al.*, "Observation of Bogoliubov excitations in exciton-polariton condensates," *Nature Pysics*, vol. 4, pp. 700–705, 2008. 24

[59] A. Amo, D. Sanvitto, F. Laussy, *et al.*, "Collective fluid dynamics of a polariton condensate in a semiconductor microcavity," *Nature*, vol. 457, pp. 291–295, 2009. 24

[60] L. Pitaevskii and S. Stringari, *Bose-Einstein condensation*. Oxford Science Publications, 2003. 25, 29

[61] B. Nelsen, G. Liu, M. Steger, D. Snoke, R. Balili, K. West, and L. Pfeiffer, "Coherent flow and trapping of polariton condensates with long lifetime," *arXiv*, pp. 1–18, 2012. 25

[62] V. Stevenson, R. aand Astratov, M. Skolnick, *et al.*, "Continuous wave observation of massive polariton sedistribution by stimulated scattering in semiconductor microcavities," *Physical Review Letters*, vol. 85, p. 3680, 2000. 25

[63] A. Brichkin, S. Novikov, A. Larionov, *et al.*, "Effect of Coulomb interaction on exciton-polariton condensates in GaAs pillar microcavities," *Physical Review B*, vol. 84, p. 195301, 2011. 25

[64] H. Deng, G. Weihs, D. Snoke, J. Bloch, and Y. Yamamoto, "Polariton lasing vs. photon lasing in a semiconductor microcavity," *PNAS*, vol. 100, pp. 15318–15323, 2003. 25

[65] D. Bajoni, P. Senellart, E. Wertz, I. Sagnes, A. Miard, A. Lematre, and J. Bloch, "Polariton laser using single micropillar GaAsGaAlAs semiconductor cavities," *Physical Review Letters*, vol. 100, p. 047401, 2008. 26, 27

[66] K. Hennessy, A. Badolato, M. Winger, *et al.*, "Quantum nature of a strongly coupled single quantum dot cavity system," *Nature*, vol. 445, pp. 896–899, 2007. 27

[67] G. Dasbach, M. Schwab, M. Bayer, D. Krizhanovskii, and A. Forchel, "Tailoring the polariton dispersion by optical confinement:access to a manifold of elastic polariton pair scattering channels," *Physical Review B*, vol. 66, p. 201201, 2002. 27

[68] M. de Lima Jr and P. Santos, "Modulation of photonic structures by surface acoustic waves," *Reports on Progress in Physics*, vol. 68, p. 1639, 2005. 27, 28

[69] J. Rudolph, R. Hey, and P. Santos, "Long-range exciton transport by dynamic strain fields in a GaAs quantum well," *Physical Review Letters*, vol. 99, p. 047602, 2007. 28, 32

[70] E. Cerda-Mndez, D. Sarkar, D. Krizhanovskii, S. Gavrilov, K. Biermann, M. Skolnick, and P. Santos, "Exciton-polariton gap solitons in two-dimensional lattices," *Physical Review Letters*, vol. 111, p. 146401, 2013. 28

[71] D. Krizhanovskii, D. Sanvitto, A. Love, M. Skolnick, D. Whittaker, and J. Roberts, "Dominant effect of polariton-polariton interactions on the coherence of the microcavity optical parametric oscillator," *Physical Review Letters*, vol. 97, p. 097402, 2006. 29

[72] M. Wouters and I. Carusotto, "Goldstone mode of optical parametric oscillators in planar semiconductor microcavities in the strong-coupling regime," *Physical Review A*, vol. 76, p. 043807, 2007. 29

[73] S. Dettmer, D. Hellweg, P. Ryytty, *et al.*, "Observation of phase fluctuations in elongated Bose-Einstein condensates," *Physical Review Letters*, vol. 87, p. 160406, 2001. 29

[74] C. Kurtsiefer, S. Mayer, P. Zarda, and H. Weinfurter, "Stable solid-state source of single photons," *Physical Review Letters*, vol. 85, pp. 290–293, 2000. 30

[75] M. Steiner, A. Hartschuh, R. Korlacki, and A. Meixner, "Highly efficient, tunable single photon source based on single molecules," *Applied Physics Letters*, vol. 90, p. 183122, 2007. 30

[76] M. Bamba, A. Imamoglu, I. Carusotto, and C. Ciuti, "Origin of strong photon antibunching in weakly nonlinear photonic molecules," *Physical Review A*, vol. 83, p. 021802, 2011. 31, 39, 58

[77] S. Ferretti, L. Andreani, H. Tureci, and D. Gerace, "Photon correlations in a two-site nonlinear cavity system under coherent drive and dissipation," *Physical Review A*, vol. 82, p. 013841, 2010. 31

[78] M. Greiner, O. Mandel, T. Esslinger, T. Hansch, and I. Bloch, "Quantum phase transition from a superfluid to a Mott iinsulator in a gas of ultracold atoms," *Nature*, vol. 415, pp. 39–44, 2002. 32

[79] I. Bloch, "Exploring quantum matter with ultracold atoms in optical lattices," *Journal of Physics B: Atomic, Molecular, and Optical Physics*, vol. 38, pp. S629–S643, 2005. 32

[80] C. Toninelli, Y. Delley, T. Stoferle, A. Renn, S. Gotzinger, and V. Sandoghdar, "A scanning microcavity for in situ control of single-molecule emission," *Applied Physics Letters*, vol. 97, p. 021107, 2010. 32

[81] M. de Lima, M. van der Poel, P. Santos, and J. Hvam, "Phonon-induced polariton superlattices," *Physical Review Letters*, vol. 97, p. 045501, 2006. 32

[82] G. Rempe, R. Thompson, H. Kimble, and R. Lalezari, "Measurement of ultralow losses in an optical interferometer," *Optics Letters*, vol. 17, pp. 363–365, 1992. 33

[83] S. Dufferwiel, F. Fras, A. Trichet, P. Walker, F. Li, L. Giriunas, *et al.*, "Strong exciton-photon coupling in open semiconductor microcavities," *Applied Physics Letters*, vol. 104, p. 192107, 2014. 34, 35

[84] C. Rushworth, J. Davies, J. Cabral, P. Dolan, J. Smith, and C. Vallance, "Cavity-enhanced optical methods for online microfluidic analysis," *Chemical Physics Letters*, vol. 554, pp. 1–14, 2012. 35

[85] A. Verger, C. Ciuti, and I. Carusotto, "Polariton quantum blockade in a photonic dot," *Physical Review B*, vol. 73, p. 193306, 2006. 36

[86] A. Siegman, *Lasers*. University Science Books, 1986. 36

[87] S. Dufferwiel, *Strongly confined exciton-polaritons in a tunable semiconductor microcavity*. PhD thesis, University of Sheffield, Department of Physics and Astronomy, 2014. 37, 49, 69, 95, 97

[88] S. Michaelis de Vasconcellos, A. Calvar, A. Dousse, *et al.*, "Spatial, spectral, and polarization properties of coupled micropillar cavities," *Applied Physical Letters*, vol. 99, p. 101103, 2011. 38

[89] V. Savona, C. Piermarocchi, A. Quattropani, F. Tassone, and P. Schwendimann, "Microscopic theory of motional narrowing of microcavity polaritons in a disordered potential," *Physical Review Letters*, vol. 78, p. 4470, 1997. 39

[90] B. Besga, C. Vaneph, J. Reichel, J. Esteve, A. Reinhard, J. Miguel-Sanchez, A. Imamoglu, and T. Volz, "Polariton boxes in a tunable fiber cavity," *Physical Review Apllied*, vol. 3, p. 014008, 2015. 40

[91] P. Trichet, R. Dolan, R. Coles, M. Hughes, and M. Smith, "Topographic control of open-access microcavities at the nanometer scale," *Optics Express*, vol. 23, pp. 17205–17216, 2015. 42

[92] A. Yariv, *Quantum Electronics*. John Wiley and Sons, 1975. 51

[93] M. Sich, D. Krizhanovskii, M. Skolnick, and otthers, "Observation of bright polariton solitons in a semiconductor microcavity," *Nature Photonics*, vol. 6, p. 5055, 2011. 67

[94] J. Chen, T. Lu, Y. Wu, S. Lin, and W. Liu, "Large vacuum Rabi splitting in ZnO-based hybrid microcavities observed at room temperaturee," *Applied Physics Letters*, vol. 94, p. 061103, 2009. 68

[95] N. Antoine, F. Natali, and D. Byrne, "Observation of Rabi splitting in a bulk GaN microcavity grown on silicon," *Physical Review B*, vol. 68, p. 153313, 2003. 68

[96] E. Cotta and P. Roma, "Determination of oscillator strength of confined excitons in a semiconductor microcavity," *Condensed Matter Physics*, vol. 17, p. 23702, 2014. 68

[97] S. Dufferwiel, F. Li, A. Trichet, L. Giriunas, *et al.*, "Tunable polaritonic molecules in an open microcavity system," *Applied Physics Letters*, vol. 107, p. 1, 2015. 81

[98] L. Flatten, A. Trichet, and J. Smith, "Spectral engineering of coupled open-access microcavities," *Laser & Photonics Reviews*, vol. 10, p. 195, 2016. 81

[99] M. Wouters, I. Carusotto, and C. Ciuti, "Spatial and spectral shape of inhomogeneous nonequilibrium exciton-polariton condensates," *Physical Review B*, vol. 77, p. 115340, 2008. 95

[100] D. Buan and V. Phan, "Phase diagram of microcavity exciton-polariton condensates," *Europhysics Letters*, vol. 116, p. 57004, 2017. 104

[101] O. Jamadi, F. Reveret, E. Mallet, *et al.*, "Polariton condensation phase diagram in wide-band-gap planar microcavities: GaN versus ZnO," *Physical Review B*, vol. 93, p. 115205, 2016. 107

[102] M. Sodagar, M. Miri, A. Eftekhar, and A. Adibi, "Optical bistability in a one-dimensional photonic crystal resonator using a reverse-biased pn-junction," *Optics Express*, vol. 23, pp. 2676–2685, 2015. 112

[103] M. Soltani, S. Yegnanarayanan, Q. Li, A. Eftekhar, and A. Adibi, "Self-sustained gigahertz electronic oscillations in ultrahigh-Q photonic microresonators," *Physical Review A*, vol. 85, p. 053819, 2012. 112

[104] A. Arbabi, P. Lu, B. Griffin, and L. Goddard, "Thermally-induced nonlinearity and optical bistability in Si_3N_4 microring resonators," *Optical Society of America*, p. 90, 2012. 112

[105] B. Sfez, J. Oudar, J. Michel, R. Kuszelewicz, and R. Azoulay, "High contrast multiple quantum well optical bistable device with integrated Bragg reflectors," *Applied Physics Letters*, vol. 57, p. 324, 1990. 112

[106] A. Baas, J. Karr, H. Eleuch, and E. Giacobino, "Optical bistability in semiconductor microcavities," *Physical Review A*, vol. 69, p. 023809, 2004. 112

[107] S. Dufferwiel, F. Li, E. Cancellieri, L. Giriunas, *et al.*, "Spin textures of exciton-polaritons in a tunable microcavity with large TE-TM splitting," *Physical Review Letters*, vol. 115, p. 246401, 2015. 113

[108] E. Cancellieri, F. Marchetti, M. Szymanska, and C. Tejedor, "Multistability of a two-component exciton-polariton fluid," *Physical Review B*, vol. 83, p. 214507, 2011. 118

[109] E. Cancellieri, J. Chana, M. Sich, *et al.*, "Logic gates with bright dissipative polariton solitons in Bragg cavity systems," *Physical Review B*, vol. 92, p. 174528, 2015. 118

[110] D. Krizhanovskii, A. Tartakovskii, A. Chernenko, V. Kulakovskii, M. Emam-Ismail, M. Skolnick, and J. Roberts, "Energy relaxation of resonantly excited polaritons in semiconductor microcavities," *Solid State Communications*, vol. 118, pp. 583–587, 2001. 121

[111] D. Krizhanovskii, A. Tartakovskii, M. Makhonin, A. Dremin, and V. Kulakovskii, "Influence of nonstimulated polariton relaxation on parametric scattering of microcavity polaritons," *Physical Review B*, vol. 70, p. 195303, 2004. 121

[112] K. Zhang, Y. Huang, A. Miroshnichenko, and L. Gao, "Tunable optical bistability and tristability of nonlinear graphene-wrapped dielec-

tric nanoparticles," *The Journal of Physical Chemistry C*, vol. 121, p. 1180411810, 2017. 121

[113] D. Mazurenko, "Ultrafast optical switching in three-dimensional photonic crystals," *Physical Review Letters*, vol. 91, p. 213903, 2003. 121

[114] G. Assanto, Z. Wang, D. Hagan, and E. Van Stryland, "All-optical modulation via nonlinear cascading in type II second-harmonic generation," *Applied Physics Letters*, vol. 67, p. 2120, 1995. 121

[115] L. Greuter, D. Najer, A. Kuhlmann, S. Valentin, *et al.*, "Epitaxial lift-off for solid-state cavity quantum electrodynamics," *Journal of Applied Physics*, vol. 118, p. 075705, 2015. 132, 133

[116] F. Li, E. Cancellieri, G. Buonaiuto, M. Skolnick, D. Krizhanovskii, and D. Whittaker, "Full Stark control of polariton states on a spin-orbit hypersphere," *Physical Review B*, vol. 94, p. 201301, 2015. 133, 134